UNIVERSITY OF OKLAHOMA

GRADUATE COLLEGE

MODELLING AND VERIFICATION OF THERMOACOUSTIC MEDICAL IMAGING FROM NANOSCOPIC TO MACROSCOPIC RESOLUTIONS

A DISSERTATION

SUBMITTED TO THE GRADUATE FACULTY

in partial fulfillment of the requirements for the

Degree of

DOCTOR OF PHILOSOPHY

By

PRATIK SAMANT

Norman, Oklahoma

2019

MODELLING AND VERIFICATION OF THERMOACOUSTIC MEDICAL IMAGING FROM NANOSCOPIC TO MACROSCOPIC RESOLUTIONS

A DISSERTATION APPROVED FOR THE
STEPHENSON SCHOOL OF BIOMEDICAL ENGINEERING

BY THE COMMITTEE CONSISTING OF

Dr. Liangzhong Xiang, Chair

Dr. Hong Liu

Dr. Bin Zheng

Dr. Yuzhen Qiu

Dr. John Kimble Frazer

Acknowledgement

None of the work presented here would have been possible without the active support and guidance of Dr. Liangzhong Xiang. Throughout all the hardships of research in the past four years, Dr. Xiang has been a steady source of encouragement that helped me get through it. He believed in me from the start when I sometimes struggled to believe in myself, and he has been a critical part of helping me realize and maximize my potential as a student, a scientist, and a member of the academic community. He has always actively been cognizant of my professional goals and has gone above and beyond to help me achieve them, I could not have dreamt of a more supportive doctoral advisor.

I'd also like to thank my lab mates and all those who helped me with this research, especially Siqi Wang, Jack Merrill, Tiffany Tran, Dr. Yue Zhou, Dr. Shanshan Tang, Dr. Yong Chen, and Dr. Jian Chen, for their good company and support throughout my daily research. Ultimately all our research has been teamwork, and this strong team kept me motivated through it all to keep going in the face of hardship.

A big thank you to all my committee members who took the time to mentor me throughout graduate school. For the past five years they have all been highly accessible and ready to provide support whenever it was asked of them.

Thank you to Dr. Michael Detamore, Dr. Lei Ding, and Shayla Glover for their institutional support through the Stephenson School of Biomedical Engineering. They made sure that I was supported by me department every step of the way and made sure that I got the most out of the opportunities I had these four years.

To the friends I've made in Norman, Dan Markman, Conner Flansburg, Haden Hime, Bill Dower, Patrick Hart, I could not have made it here without being able to unwind with all of you at the end of the week. Thank you for helping make my years in Norman the best of my life so far.

I'd like to express enormous thanks to my friends back home in Toronto, Tiffany Chan, Kristina Morgan, Caterina Sauro and Eric Turner. who were always around to lend an ear or share a laugh despite being a continent apart, and for their friendships stretching back to the majority (if not the entirety) of my adult life.

Thank you to my parents for raising me to value education and be curious, and for helping me every step of the way to graduate school, including financial, emotional, and logistical support throughout my entire academic life. Thank you to my little brother Parth, who continues to make me proud with his insight, hard work, and empathy despite his young age. I'll always be there when you need me.

Thank you to George Murzaku, who first got me interested in physics and mathematics in high school. He will forever set the standard of teaching to which I aspire to live up to. With an uncanny ability to inspire, challenge, communicate, and accommodate, Mr. Murzaku has made a lasting impact on my life, and the lives of many other students. As I have grown as a physicist, engineer, and researcher, I still feel like I have never left his classroom. I hope I've made him proud.

To Patrick Antila, my oldest friend. Thank you for your friendship, thank you for being there at times when it felt like nobody else was, thank you for fighting so hard for me when it would have been easy to give up. Lastly, thank you for making sure I stuck around long enough to write this.

Finally, thank you to Anisha Nijhawan, who has become as much a part of me as my hands and feet. Her empathy, intelligence, perseverance, and courage have consistently left me in awe. Coming home to her has been the highlight of my life, and there's nobody I'd rather cross an ocean with.

Table of Contents

List of Figures

Abstract

In this thesis, three main questions regarding the potential of thermoacoustic imaging are answered: 1) what are the conventional resolution limitations of photoacoustic imaging and how can they be extended to enable high-resolution imaging, 2) Can photoacoustic imaging resolution be brought down to nanoscopic levels, and 3) As laser based photoacoustic imaging has been deployed with great success, is it also possible for proton beams to generate useful ultrasound signals for imaging?

Whereas laser-induced photoacoustic tomography has been widely explored for a diverse range of biomedical contexts, there remain some fundamental limits to the resolution levels in which it can operate. Namely, the axial resolution of photoacoustic imaging remains restricted by the fact that ultrasonic transducers are not able to detect high-frequency signals that encode nanoscale resolution information. Therefore, there is a lingering question about how photoacoustic imaging can truly enter the realm of nanoscale imaging, as has been done by other modalities such as STED microscopy, structured illumination microscopy, and STORM microscopy.

It is believed that laser-based detection in lieu of a transducer may enable a super-resolution photoacoustic imaging modality. However, there remain important questions about the reach and feasibility of nanoscale photoacoustic imaging. Specifically: will highly focused lasers directed at single cells result in thermal damage of biological samples? Will the axial imaging resolution of laser based detection truly be able to overcome the conventional optical diffraction limit of ~200nm? Will optical detection be sensitive enough to detect photoacoustic signals?

Consequently, models are developed for thermoacoustic imaging for nanoscale imaging at super-resolutions exceeding that of the optical diffraction limit (~200nm), that show the potential for thermoacoustic imaging to enable super-resolution imaging of single cells. The models confirm that such imaging is possible while simultaneously ensuring the thermal safety of cells as the laser-induced temperature rise of such imaging is only within mK, potentially allowing for high-resolution imaging in vivo. It is also confirmed that a laser of 7ps duration should generate frequencies high enough to enable super-resolutions.

Models are also developed for the estimation of the sensitivity and resolution of these high-resolution imaging, and it is predicted that super-resolution photoacoustic imaging may be able to image at axial resolutions of 10nm at noise equivalent number of molecules of 292 in the case of imaging hemoglobin in red blood cells. A length-scale and time-scale generalizable simulation workflow is developed and deployed to generate simulated images of super-resolution photoacoustic imaging, showing the potential of 3D super-resolution achievable via thermoacoustic imaging.

The model predictions regarding detectable high frequency photoacoustic signal generation is experimentally confirmed via the creation and testing of a pump-probe based preliminary photoacoustic imaging system. The system is shown to be capable of detecting a clear and repeatable signal. Acquired A-lines from this system confirm that GHz frequencies can be detected using pump-probe detection in photoacoustics, thereby opening the door for nanoscale photoacoustic imaging However, the experimental results also demonstrate that feasible and convenient nanoscale imaging will require a more stable laser than is available, as pulse to pulse

intensity fluctuations in the laser greatly limit the imaging speed and necessary number of averages for a single A-line scan.

With the potential of laser-based nanoscale imaging established. It is interesting to consider whether proton beams can be used for thermoacoustic imaging as well. This is especially important as the problem of Bragg peak localization is a prominent issue in modern day proton therapy, and protoacoustic emissions could well have the potential to enable a real-time therapy monitoring procedure in proton therapies.

Models previously deployed in nanoscale imaging contexts are therefore extended to the millimeter range, thereby demonstrating a versatile workflow that is deployable for feasibility studies for nanoscopic to macroscopic imaging and robust to different types of incident radiation. The models show that thermoacoustic imaging can enable 3D visualization of protoacoustic Bragg peaks at millimeter resolutions, thereby potentially enabling real-time Bragg peak localization during proton therapy of patients.

The developed models show promise and use towards the development of novel thermoacoustic imaging modalities and can be deployed to assess feasibility of different configurations of thermoacoustic imaging prior to the expenditure of resources on experimental realization. In this way, the developed models have the potential to enable the development of various thermoacoustic imaging modalities via a single generalizable framework through which imaging characteristics can be predicted at multiple length and time scales.

Chapter 1: Introduction

Thermoacoustic imaging (TAI) is a promising series of imaging modalities introduced in the past two decades. These novel imaging modalities have taken great advantage of radiation induced ultrasound for the purpose of imaging energy absorption maps. The realization of successful TAI has the potential to solve a wide variety of clinical and biomedical problems, including the enabling of neurological imaging[1–4], vascular imaging[5–8], super-resolution imaging[9–15], DNA imaging [16,17], high-resolution mammography[18–27], radiation therapy monitoring[28–30], proton therapy monitoring[31,32], and many more. While in effect the myriad TAI modalities are themselves a series of independent imaging modalities with their own advantages and potentials for clinical implementation, all TAI modalities share the same basic physics of signal generation and detection. This chapter will review the physics of TAI, introduce the key thermoacoustic imaging modalities to be explored and discussed in this thesis. This chapter will also highlight the important of modelling in the context of extending TAI to novel clinical problems at nanoscale imaging and microscale imaging and present an overview of the thesis' chapters.

The Thermoacoustic Effect

All TAI modalities ultimately rely on the thermoacoustic (TA) effect[33,34], which is discussed in this sub-section. In a typical deployment of TAI, some radiation is incident on the sample of interest. This radiation is pulsed in nature and so deposits its energy very rapidly into the sample. The sample then absorbs this incident energy, resulting in localized heating of the sample. The heating of the sample is typically negligible in the context of affecting biological samples (typical heating can be in the range of mK^9). This rapid sample heating leads to thermoelastic expansion

of the sample, which in turn produces a propagating pressure wave with the site of excitation acting as an acoustic source. This pressure wave manifests itself in the form of radiation induced ultrasound (RU), which can yield insights about radiation energy deposition. RU signals are typically broadband, with center frequency and spectrum characteristics influenced by the excitation pulse duration, and spatial energy distribution. The governing equation of thermoacoustic signal propagation in matter is as follows[33]:

$$\left(\nabla^2 - \frac{1}{v_s^2}\frac{\partial^2}{\partial t^2}\right)p(\mathbf{r},t) = -\frac{\beta_V}{\kappa v_s^2}\frac{\partial^2 T(\mathbf{r},t)}{\partial t^2} \quad (1)$$

Where v_s is the speed of sound in the medium, t is time, $\mathbf{r}$ is the position, β_v is the coefficient of volume expansion, κ is the isothermal compressibility, p is the induced TA pressure, and T is the temperature rise induced in the sample. In the case of a delta function excitation, equation 1 can be further simplified to

$$\left(\nabla^2 - \frac{1}{v_s^2}\frac{\partial^2}{\partial t^2}\right)p(\mathbf{r},t) = -\frac{\beta}{C_p}\frac{\partial H(\mathbf{r},t)}{\partial t} \quad (2)$$

where C_p is the heat capacity at constant pressure, and H is the heating function of the sample, defined as the thermal energy converted into a pressure wave per unit volume and per unit time. In the case of excitation via an optical source (including x-ray excitation), the heating function is given by $H = \mu_a \Phi$, where μ_a is the energy absorption coefficient and Φ is the optical fluence rate, defined as radiant energy received per unit area per unit time.[33] Upon analysis of equation 1, the right side of the equation corresponds to an excitation-dependent source term that ultimately

determines the generation efficiency of the signal, p. The left side of the equation models the propagation of the signal itself.

Typical TA signals, when detectable, are much weaker than conventional ultrasound signals generated by transducers, therefore it is important for any TAI set-up, that operators carefully optimize signal generation efficiency and detection. In this context, there are two key factors to consider. The first is the excitation pulse, and the second is the detection apparatus, ultimately all TAI setups must carefully incorporate both factors to best optimize the achieved imaging signal-to-noise ratio (SNR).

As the heating function in equation 2 is linearly proportional to the fluence rate, it is important in TAI experiments to ensure that the excitation pulse varies quickly (i.e. the pulse must be sufficiently short in duration to efficiently generate a TA signal). The exact requirements of the pulse width are dependent on the sample itself. In a sample being heated by an excitation pulse, there are two key processing at work simultaneously and in conflict with one another. Firstly, the pulse is depositing energy into a fixed spatial region, which is causing the localized build-up of heat in the area. At the same time, this heat is dissipating outwards from the region in response to the induced temperature gradient. If the pulse deposits energy so quickly, such that the generated heat does not have time to dissipate outward, the resulting heat build-up will instead induce rapid thermoelastic expansion in the sample, and subsequently generate a TA signal. This is the main driving mechanism behind the generation of TA waves.[35] There are two fundamental dependencies of the final signal on the excitation pulse width, the first relation occurs when the pulse duration

is, to a good approximation, a delta function. The second relation occurs for longer lasting pulses in which the delta function approximation is not value.

Delta Function Approximation

In the case of delta function excitation, equation 2 is the governing equation of TA signal generation and propagation. The main condition under which equation 2 can be used is known as stress confinement. Stress confinement occurs when the pulse energy is deposited faster than any fractional volume expansion can occur in the sample. This time is given by the time needed for sound in the sample to travel the characteristic length of heat heterogeneity (determined by either the dimensions of the absorbing target as well as the decay constant of the optical energy deposition, whichever is smaller).[33]Thermal confinement occurs when the entirely of the pulse interaction with the sample occurs at a shorter duration than the characteristic time of thermal heterogeneity, of the sample, meaning that thermal diffusion can be neglected. In order to achieve both stress and thermal confinement, a Gaussian excitation pulse duration must be fixed such that the pulse duration, θ ideally meets the condition

$$\theta \ll \frac{d_c}{v_s} \ll \frac{d_c}{4\alpha_{th}} \tag{3}$$

Where d_c is the characteristic length of heat heterogeneity (typically d_c is taken to be the desired resolution of imaging) and α_{th} is the thermal diffusivity. The $\frac{d_c}{4\alpha_{th}}$ inequality enforces the condition of thermal confinement, and $\frac{d_c}{v_s}$ inequality enforces the condition of stress confinement. Stress confinement typically requires shorter pulse than thermal confinement, but both conditions are

important in applying the delta excitation assumption. If stress confinement is met, then equation 2 can be applied and the resulting pressure wave can be obtained by analytically solving it. The regime of pulse widths in which stress confinement is satisfied is especially important because the pulse width (in and of itself) of the excitation becomes largely irrelevant to the final generated acoustic signal. Now, as the pulse width is often related to the total energy deposited in the sample, in practice it tends to be the case that lowering the pulse width even in the stress confinement regime can indeed affect signal strength. Nevertheless, this difference in signal intensity for different pulse widths is entirely related to the total energy deposited per pulse, and all other factors being equal reduction in the pulse duration does not continuously improve signal generation efficiency past this limit.[36]

In the case of acoustic detection via the use of ultrasonic transducers, it is typical that the transducer itself is far away (on the order of millimeters) from the excitation source. In this case, the detected signal strength is typically not improved drastically by meeting stress confinement narrowly (i.e. $\theta < \frac{d_c}{v_s}$ is good enough, and θ does not have to be drastically smaller than $\frac{d_c}{v_c}$ for the delta function approximation to apply. However, in the case of optical detection, the detector photoacoustic amplitude can be very similar to the target acoustic amplitude as probe lasers can be close to confocal with pump lasers, in the case where the detection and excitation laser are close to confocal (detector distance from the source is on the order of nanometers), the condition $\theta \gg \frac{d_c}{v_s}$ must be enforced if the delta function approximation is to be applied.

Before considering the case of finite pulse excitation, it is useful to work through the solution of the TA wave equation, as ultimately, a practical solution to the general case from equation 1 can be derived from the delta function case from equation 2.

Solution to the TA Wave Equation

In the case of delta function heating (equation 2), the TA wave equation is most commonly solved using a Green's function approach, which yields a full analytic solution, p_δ in the form of the integral function[33]

$$p_\delta(\mathbf{r}, t) = \frac{\beta_V}{4\pi C_p}\frac{\partial}{\partial t}\int \mathrm{d}\mathbf{r}'\,\frac{1}{|\mathbf{r}-\mathbf{r}'|}H\left(\mathbf{r}', t - \frac{|\mathbf{r}-\mathbf{r}'|}{v_s}\right) \tag{4}$$

While equation 2 can be universally solved via the use of equation 4, the vast majority of TAI set-ups do not allow for an solution to equation 2 as the integral in equation 4 rarely has an exact analytic expression , or alternately the solution is extremely complicated to derive. Additionally, even small changes in the sample's acoustic or radiation absorption characteristics can render exact solutions to the integral invalid. Therefore, exact solutions to the photoacoustic wave equation are typically not robust to all changes in sample and pulse characteristics, and usually must be derived under strict assumptions. Therefore, equation 2 is more commonly solved numerically, as this allows for the freedom of all manner of complicated forms of all its terms, including support for complex initial pressures matching real biological samples, as well as support to incorporate tissue heterogeneities, acoustic attenuation, transducer frequency response, and the loss of information that occurs in the case of limited view of the sample.[37]

The initial pressure rise induced in a sample in the case of delta function heating, heretofore referred to as $p_{0\delta}$, can be expressed in terms of several parameters[33] and take several forms, as shown below

$$p_{0\delta}(\mathbf{r}) = \Gamma A_c = \frac{\beta_V}{\kappa \rho C_V} = \frac{\beta T(\mathbf{r})}{\kappa} \tag{5}$$

Where Γ is the unitless Grüneisen parameter, defined as $\frac{\beta_V}{\kappa \rho C_V}$, ρ is the mass density, C_V is the heat capacity at constant volume, and A_c is the specific volumetric energy absorption, defined as the energy absorbed per unit volume. In all cases, $p_{0\delta}$ is spatially dependent, and indeed this is a crucial feature of TAI. Ultimately, a TA image is an acceptably accurate reconstruction of the initial condition of equation 2. In the case of delta function heating, the goal of TA reconstruction is to retrieve the spatial distribution of $p_{0\delta}$. If the exact form of p_δ is known at some time after the initial excitation, then the exact form of the initial pressure, $p_{0\delta}$ is theoretically possible. The inverse problem of all thermoacoustics is the retrieval of p_0 given recorded pressures from sensors that sample $p(\mathbf{r}, t)$. However, in this section only delta function excitations have been considered. The next section will outline the solution in the case of finite pulse durations.

Finite Pulse Durations

Whereas the solution of the TA wave equation is easily retrievable in the case of delta function excitation, the solution in the finite pulse case is more complicated. When stress confinement is not met, the TA pulse width is a major factor in the optimization of the signal amplitude.[36] The resultant TA pressure at the target in the case of a non-stress confined pulse duration is roughly

proportional to the inverse of the pulse duration squared, namely, the condition $p \propto \frac{1}{\theta^2}$ is applied. In this regime, a shorter pulse is substantially more effective at generation TA signals as opposed to a longer pulse in terms of raw amplitude. However, it is important to keep in mind that shorter pulses in this regime will affect the frequency spectrum of the signal being generated. Shorter pulses produce high frequency TA signals, and so while the absolute signal strength is increases as θ decreases, it is possible in practice to decrease SNR in these cases if the detection apparatus is not of equivalent sensitivity at higher frequencies. The pressure generated in the case of finite pulse duration is obtained by solving equation 1 indirectly using a delta function solution to equation 2.

$$p(\mathbf{r}, t) = \int_{-\infty}^{\infty} \mathrm{d}t' p_{\delta}(\mathbf{r}, t - t') S(t') \tag{6}$$

Where $S(t')$ is the temporal profile of the excitation pulse (typically a Gaussian with the full width at half maximum (FWHM) equal to θ). Through the use of equation 6, a universal solution is available to equation 1, this solution is generalizable to all pulse widths as the limit of equation 6 as the temporal profile approaches a delta function is p_{δ} itself.

Having solved the TA wave equation for both delta excitations and finite pulse excitations, it is prudent to address some common ideas and techniques through which imaging parameters such as resolution and sensitivity can be optimized. The next section of the introduction discusses the key parameters that are typically optimized in TAI and the most common techniques used to optimize them.

Imaging Characteristics

Imaging Resolution

As most versions of TAI are capable of 3D imaging, the factors governing resolution depend on the specific set-up. Nevertheless, there are some trends common to all TAI that are important to discuss. The first of these is the ability of ultrasonic detection to resolve details in the sample. In general, the ability of an ultrasound signal to resolve an object depends entirely on its frequency. Higher frequency signals have narrower envelopes, and therefore can resolve finer details. To this end, it is always important in TAI to maximize the generated and detected acoustic frequencies during imaging. Additionally, it is important to ensure that generated frequencies are within the detection bandwidth, otherwise signal sensitivity will become a significant issue. The matching of the detection bandwidth and pulse generation is one of the most important considerations towards whether TAI set-up experiments will be successful.

Generally, it is a rough approximation that the maximum frequency generated in a TA experiment is inversely proportional to θ. This means that in the case that $\frac{1}{\theta}$ is much larger than the detector bandwidth limitation, there is no additional benefit gained by lowering the pulse width, and indeed the generated TA signal may well not be detectable

TAI fundamentally involves the detection of ultrasound for the purposes of imaging. To this end, the fundamental resolution limits that the ultrasound can probe are dependent on the maximum frequency of the ultrasound signal. The ability of a standard TA signal to resolve detail is equal to the distance travelled by sound in the time duration equal to the full-width at half maximum of the

signal.[36,38,39] This is better illustrated below in Figure 1, which shows an example TA signal from a point source. The implication of Figure 1 is that the resolving power in a TA signal is directly related to the frequency of the signal, as higher frequencies will have narrower envelopes and therefore smaller FWHM values.

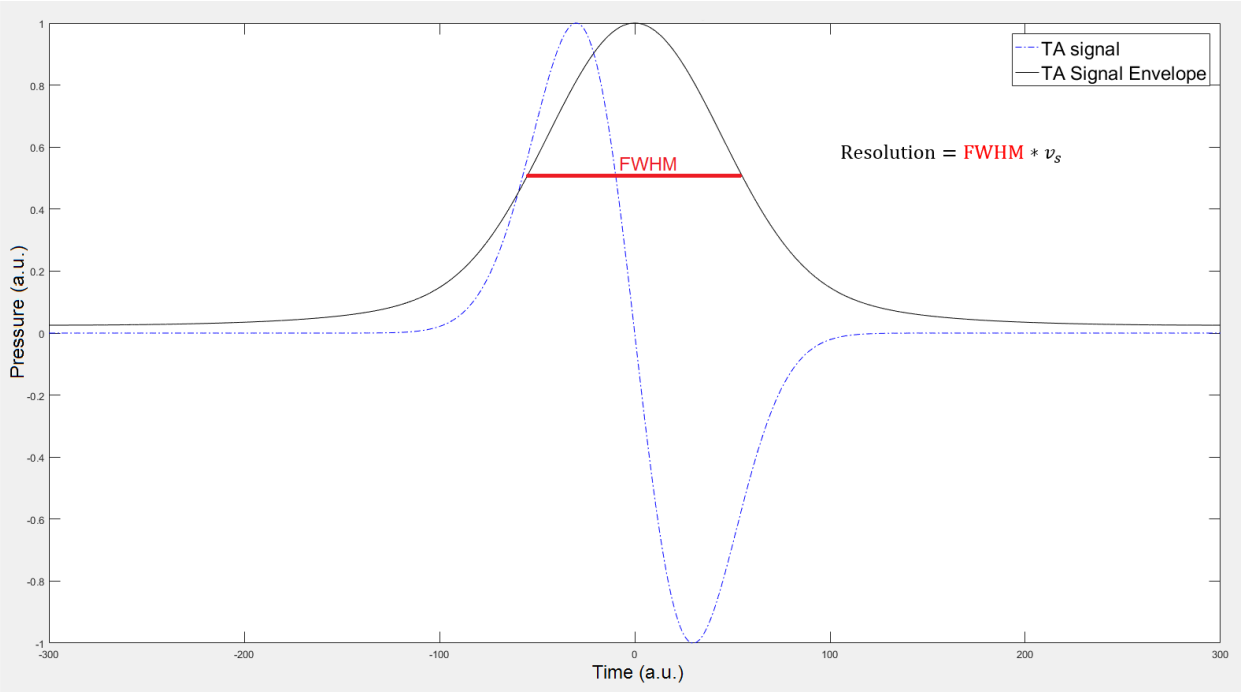

Figure 1: TA signal and its Gaussian envelope as they relate to resolution. The maximum resolving distance of the TA signal is equal to product of FWHM and v_s

While this serves as an effective resolution limit on the acoustic signal's spatial resolving power, this does not necessarily mean that all TAI modalities are limited to resolutions defined by TA signal spectrum alone. Indeed, there exist implementation of TAI in which the resolution limits of ultrasound can be overcome by the thermoacoustic nature of the signal itself. i.e. because the TA signal is ultimately generated by some incident radiation, if the incident radiation itself is focused

to a spot smaller than the acoustic resolution limit outlined in Figure 1, then it is possible to achieve resolutions higher than what the acoustic signal can carry, as the entirety of the signal originates from a smaller spot size than the acoustic resolution limit.

Sensitivity

TA signal generation depends on a range of factors, depending on whether the different confinement conditions have been met[36,40], however there exist some general rules for optimizing signal generation efficiency. The equation for the amplitude of a thermoacoustic point source from a long pulse response has been derived by Calasso et al[40], and yields the following information when fully expanded

$$p(t) = \frac{\sigma\beta}{4\pi C_p r}\frac{\mathrm{d}}{\mathrm{d}t}I(t) \tag{7}$$

where σ is the absorption cross section of the absorber (which is also the source), β is the coefficient of thermal expansion, r is the distance from the source, and the time dependent function I is the time dependent intensity of the incident radiation. In the case of a Gaussian radiation pulse the intensity function takes the form

$$I(t) = \frac{E_0}{\theta}\exp\left[-k\frac{(t-\varphi)^2}{\theta^2}\right] \tag{8}$$

Where E_0 is the fluence of the incident radiation, φ is some adjustable temporal phase shift parameter, and $k = 4\ln 2$. In this case, the temporal derivative of the intensity function is

dependent on the pulse width, θ, and therefore so to is the time dependent signal, p. Then, equations 7 and 8 can be combined to yield the pulse width dependency of the pressure signal.

$$p(t) = \frac{E_0 \sigma \beta k (t-\varphi)}{2\pi C_p r \theta^3} \exp\left[-k\frac{(t-\varphi)^2}{\theta^2}\right] \quad (9)$$

As the pulse width is Gaussian in the case of most laser excitations, and indeed across many forms of pulsed radiation sources, the amplitude of the TA signal is typically dependent on the pulse width. While equation 9 is only perfectly accurate for a point source excitation, it nevertheless reveals important properties of all TA signals, namely the specific parameters than can be manipulated in order to maximize the signal generation efficiency. As β, C_p, and σ are typically sample dependent quantities, a TA signal in a given sample can typically be optimizing by insuring that the incident fluence, E_0, is as high as possible, and, in the case of Gaussian excitation, the pulse width, θ, is as low as possible. However it is to be noted that as once stress confinement has been well met (i.e. $\theta \gg \frac{d_c}{v_s}$), additional lowering of the pulse width will not improve signal strength, and indeed may reduce the SNR by pushing the generated signal to frequencies outside of detector bandwidth range.

Photoacoustic imaging

The most common and mature family of TAI modalities is photoacoustic imaging (PAI). PAI is characterized using a laser as the TA excitation source. As a requirement of all TAI is a pulsed excitation source, it is important in PAI at the excitation laser itself be pulsed and not continuous. While PAI modalities have laser-based excitation in common, they have been deployed in a wide variety of biomedical contexts at resolutions ranging from the range of organelles to organs.[35]

Photoacoustic tomography (PAT) is the main class of PAI imaging modalities used in biomedicine and has several implementations depending on the specific clinical problems being addressed. The main common theme for PAT and PAI is the use of a conventional ultrasonic transducer for detection of a laser-induced signal from the sample. As the photoacoustic (PA) signal is directly proportional in strength to the absorbed optical energy, PAI yields imaging contrast based on the absorption contrast of the sample to the excitation light. In this way, 3D optical absorption contrast images can be created via the detection of PA ultrasound signals.

The main implementation of PAI of interest in this thesis is photoacoustic microscopy (PAM). PAM is one of the first functional modes of PAI demonstrated in the literature, and remains the most mature TAI modality developed to date.[8,41] The basic principle in PAM is the use of a focused and pulsed laser that is scanned in 3D (laterally and axially) in the sample of interest, in order to provide 3D absorption contrast imaging.[5,6,35,38,42,43] PAM implementations typically feature a focused laser beam for signal generation with a confocal transducer for signal detection.

One critical constraint on conventional PAM is the limitation of the axial resolution. The axial resolution, R_a is ultimately governed by the spectrum of the generated signal and the bandwidth, B of the ultrasound detector. Assuming that sensitivity is not a problem (i.e. the broadband PA signal is detected with high SNR by the transducer), the axial resolution is given by[39]

$$R_a = \frac{4 \ln 2}{\pi} \frac{v_s}{B} \tag{10}$$

As the speed of sound in most biological tissues is approximately that of water, and typical transducers have bandwidths in the range of hundreds of MHz, the axial resolution of PAM is

typically limited to several microns, not high enough for nanoscale imaging. This contrasts with the lateral resolution of PAM, which can be as high as 200nm for a perfectly focused laser beam at 532nm wavelength.

Bringing the Axial Resolution into the nanoscale

One promising TA imaging modality proposes to bring the axial resolution of PAM down to the nanoscale, thereby enabling 3D imaging of single cells through high-resolution imaging. This modality, known as nanoscale photoacoustic tomography (nPAT), is capable of drastically improving the axial resolution over conventional PAM via the use of an optical set-up for the detection of high-frequency photoacoustic signals, rather than the use of an ultrasound transducer.

nPAT seeks to accomplish high resolution imaging via the use of an ultra-short laser pulse (picoseconds in duration) to induce an extremely high frequency (in the range of GHz) photoacoustic signal in a cell. As the signal is in the GHz range, it is not detectable via conventional ultrasonic transducers due to bandwidth limitations. Therefore, nPAT uses a second laser beam that probe the generated acoustic wave.

The mechanism through which a second laser can detect an ultrasonic wave is through the pressure dependence of an object's refractive index, the details of which are outlined later in this thesis. This optical detection is favored because of its extremely high bandwidth of detection, optical detection of ultrasonic signals is easily capable of detecting ultrasonic signals in the GHz range and therefore can enable nanoscale photoacoustic imaging.

Chapter Overview

There remain some concerns that must first be addressed prior to the deployment of nPAT. Firstly, the thermal safety of nPAT must first be guaranteed. nPAT uses a high peak power laser illumination incident onto a single cell. Additionally, the laser is focused into a tiny spot (200nm lateral resolution spot size by the optical diffraction limit), further increasing the likelihood of damaging the sample as the intensity of the laser is extremely high at this spot. Additionally, the exact expected resolution and sensitivity, especially as it related to conventional PAM, is not yet known and requires the development of a detailed model for assessment.

The main topic of this thesis is the development of a details physical model that can assess these concerns, and the extension of this model to contexts in macroscopic TAI imaging feasibility. Firstly, a model for the temperature rise during nPAT imaging of a red blood cell is created to address thermal damage issues. Secondly, a theoretical model is developed to predict the resolution and sensitivity of nPAT and tested using numerical simulations. Thirdly, the predictions of these models are tested and validated in an experimental study. Fourthly, the model is extended to macroscopic imaging in protoacoustics, thereby demonstrating its effectiveness for assessing the feasibility of novel TAI modalities at multiple length and time scales.

Chapter 2 addresses the concern of thermal damage during nPAT. A physical model is developed of the excitation beam and the red blood cell sample. Numerical finite element methods are applied to these two models in order to assess the thermal interaction between the beam and the red blood cell (RBC). It is shown that the temperature rise induced in the RBC during nPAT imaging is no more than a few mK in magnitude, and the thermal safety of nPAT is established for the purpose

of high resolution RBC imaging. Additionally, it is shown that the same incident laser pulse should still generate a strongly detectable PA signal in the sample.

In Chapter 3, a model is developed that assesses the true high-resolution imaging potential of nPAT. The theoretical maximum resolution of nPAT is derived using acousto-optical equations, and it is shown that nPAT can enable high-axial resolutions of up to 9.2nm, far surpassing that of conventional PAM. Additionally, it is shown that nPAT's sensitivity is comparable to that of PAM. Chapter 3 also developed and deploys a generalizable numerical model through which 3D imaging via nPAT can be simulated for RBC imaging.

In Chapter 4, experimental confirmation of previous theoretical predictions is established. A laser-set-up is constructed on an optical table for the purposes of demonstrating the concept of high-frequency (GHz) acoustic signal detection via the use of an optical probe. It is shown that through the use of pump-probe imaging techniques[44–48], high-frequency signals can be detected that enable nanometer level axial resolutions in PAM.

Finally in Chapter 5, the numerical models are extended to macroscopic length scales and microsecond time scales, and deployed in the context of proton therapy Bragg peak localization via the protoacoustic effect. It is shown that the model performs well at the length scales and returns stable and sensible predictions. The generalizability of the model is established, and the 3D imaging of a prostate radiation therapy dose deposition is established via simulations.

Chapter 2: Characterization of the temperature rise in a single cell during photoacoustic tomography at the nanoscale

Overview

In this chapter, a model is developed to estimate the temperature rise induced during nanoscale photoacoustic tomography (nPAT). This model is deployed in order to assess the thermal feasibility of nPAT imaging of a red blood cell. nPAT uses a laser-induced acoustic pulse to generate a nanometer-scale image. The primary motivation behind this imaging technique is the imaging of biological cells in the context of diagnosis without fluorescent tagging. During this procedure, thermal damage due to the laser pulse is a potential risk that may damage cells. A physical model is built to estimate the temperature rise and thermal relaxation during the imaging procedure. Through simulations using finite element methods, two lasers (532 nm at 5ps pulse duration and 830 nm at 0.2ps pulse duration) were simulated for imaging red blood cells (RBCs). It is demonstrated that a single 5-ps pulse laser with a 400-Hz repetition rate will generate a steady state temperature rise of less than a Kelvin on the surface of the RBCs. All the simulation results show that there is no significant temperature rise in an RBC in either single pulse or multiple pulse illumination with a 532-nm laser with 219 W fluence. Therefore, the simulation results demonstrate the thermal safety of an nPAT system. The photoacoustic signal generated by this laser is on the order of 2.5 kPa, which should still be large enough to generate high-resolution images with nPAT. Frequency analysis of this signal shows a peak at 1.47 GHz, with frequencies

as high as 3.5 GHz still being present in the spectrum. It is believed that nPAT will open an avenue for disease diagnosis and cell biology studies at the nanometer-level.

Introduction

Since the breaking of the diffraction limit through the introduction of super-resolved fluorescence microscopy, optical microscopy has been brought into the nanoscale. It has become possible then to image structures and phenomena at the nanoscale using optical microscopy. The relevance of this achievement is difficult to overstate as it allows for the analysis of an entirely different scale of objects in unprecedented detail, for which these efforts were awarded a Nobel prize. However, super-resolution techniques often rely on fluorescent tagging or the use of external contrast agents for imaging, which results in many disadvantages including, but not limited to, photobleaching, phototoxicity[49], and small in vivo lifetimes.[50] As a result, there is a very real interest in label-free nanoscale imaging modalities in biomedical settings.[51–54]

Photoacoustic tomography (PAT) is a label-free imaging technique that has already seen applications in microscopic imaging. This method circumvents the optical diffraction limit by instead relying on a laser-generated acoustic signal for imaging. PAT has seen applications in vascular biology[55–57], neurobiology[41,58,59], dermatology[60,61], opthamology[62,63] and other biological fields since its conception.[35] However, a three-dimensional (3D) PAT mechanism at the nanoscale has yet to see completion; single- cell PAT has not yet been achieved.

In nanoscale photoacoustic tomography (nPAT), laser-induced thermal excitation generates an ultrasound signal due to thermoelastic expansion. The pulse deposits energy into the specimen, which is partially converted into a detectable acoustic signal that can be used to reconstruct images.

The excitation laser pulse is focused through a lens and achieves its lateral resolution through raster-scanning, like that used in photoacoustic microscopy (PAM). However, nPAT does not rely on the use of a transducer for signal detection or axial resolution. Instead, axial scanning is done using an optical delay line in a pump-probe setup. A laser beam, dubbed the pump beam, is used to generate the photoacoustic (PA) signal, which then travels to the surface of the sample to induce a reflectivity change. At this point in time, another beam, dubbed the probe beam, is reflected off the sample. The change in surface reflectivity can then be used to measure the PA signal instead of relying on an ultrasound transducer. This detection method allows for theoretically infinite band- width via the probe beam reflectivity. As a result, nPAT can achieve even better resolution than PAM in the axial direction, while matching the resolution of PAM in the lateral directions.

Thermoelastic expansion comes with an associated temperature rise, which must be carefully controlled and accounted for during the imaging procedure.[46] Photothermal cellular damage is a common occurrence following laser irradiation[64,65] and high temperature rises have been a concern in similar experiments.[46] It is therefore crucial to demonstrate the thermal safety of nPAT before its implementation in experiment.[66,67]

Red blood cells (RBCs) are particularly good candidates for imaging via PAT. This is due to the high absorption of hemoglobin at particular excitation wavelengths. The RBC's structure can then be imaged using nPAT, providing high optical contrast with ultrahigh resolution to image the mechanics of the RBC in addition to its hemoglobin concentration distribution. This is especially fortunate because RBC structural characteristics are crucial to their function, and abnormalities are hallmarks of a multitude of diseases, including protist infection, leukemia, and anemia. In addition,

the hemoglobin concentration distribution can be analyzed to come to conclusions about the internal operations of the cell in different contexts.[68] In this chapter, finite element methods (FEM) are used to simulate the temperature rise and signal generation during nPAT of an RBC. FEM has been useful in previous models of photoacoustic absorption and signal generation,[69] so it is believed that FEM can assist to evaluate the thermal safety of nPAT, thereby providing insight on its feasibility. nPAT is a label-free method of obtaining nanoscale images by taking advantage of optical contrast and ultrasonic resolution. This process is simulated using a 532-nm laser at a frequency of 400 Hz with 219 W peak power and 5-ps pulse duration, matching a laser present at the University of Oklahoma's TRUE lab in the Stephenson Research and Technology Center (Norman, OK, USA). For the sake of comparison, an 830-nm laser at a frequency of 75 MHz is also simulated, with a peak power of 1 kW, and pulse duration of 0.2 ps. These simulations are performed in the interest of demonstrating the feasibility of using this system to image RBCs without thermal damage being a concern, while simultaneously generating a large enough signal to provide high image resolution.

Methods

Red Blood Cell Geometry

Prior to simulation, a mathematical description is needed to visualize and model the RBC shape. To this end, the work of Evans and Fung[70] provides an appropriate model. This model features a biconcave shape with adjustments, and has been regularly deployed in simulation studies involving RBCs[71–73]. The general equation of the given biconcave shape, expressed in cartesian coordinates parameterized by $\omega \in [0, \pi]$, is as follows

$$x = 0.5D \sin \omega$$

$$z = 0.25D(c_0 + c_1 \sin^2 \omega + c_2 \sin^4 \omega)$$

Where $c_0 = 0.207, c_1 = 2.003, c_2 = -1.123$ and D is the diameter of the cell. In this simulation, the diameter is set to 8μm to match a healthy RBC. This biconcave shape is shown below in Figure 2.

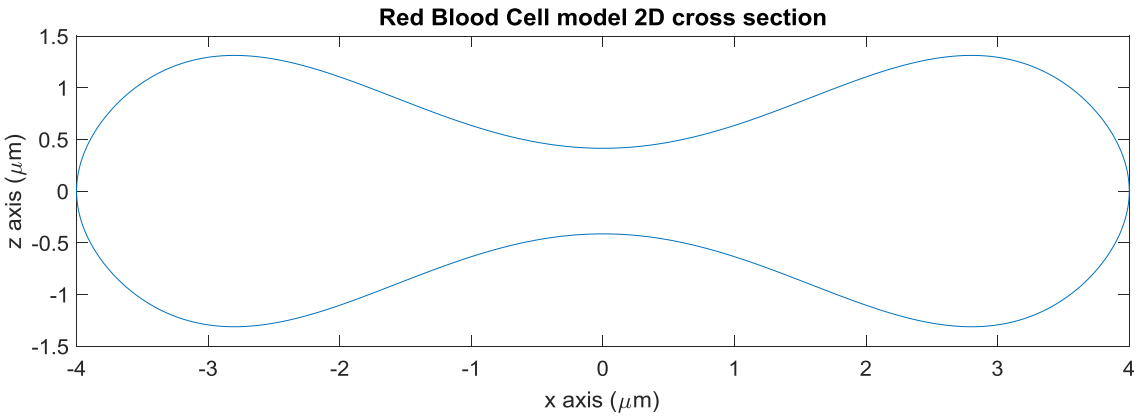

Figure 2: RBC model in two dimensions

The above equations yield the half biconcave shape in two dimensions. The 3D version of the RBC model can then be constructed through a 3D solid of revolution around the $x = 0$ axis in Figure 2. A mesh for FEM simulation can then be constructed within this shape to allow for 3-D FEM simulations with adjustable spacing. A heat source can be added into this sample to model a focused laser heating the RBC. The resulting shape is shown below in Figure 3

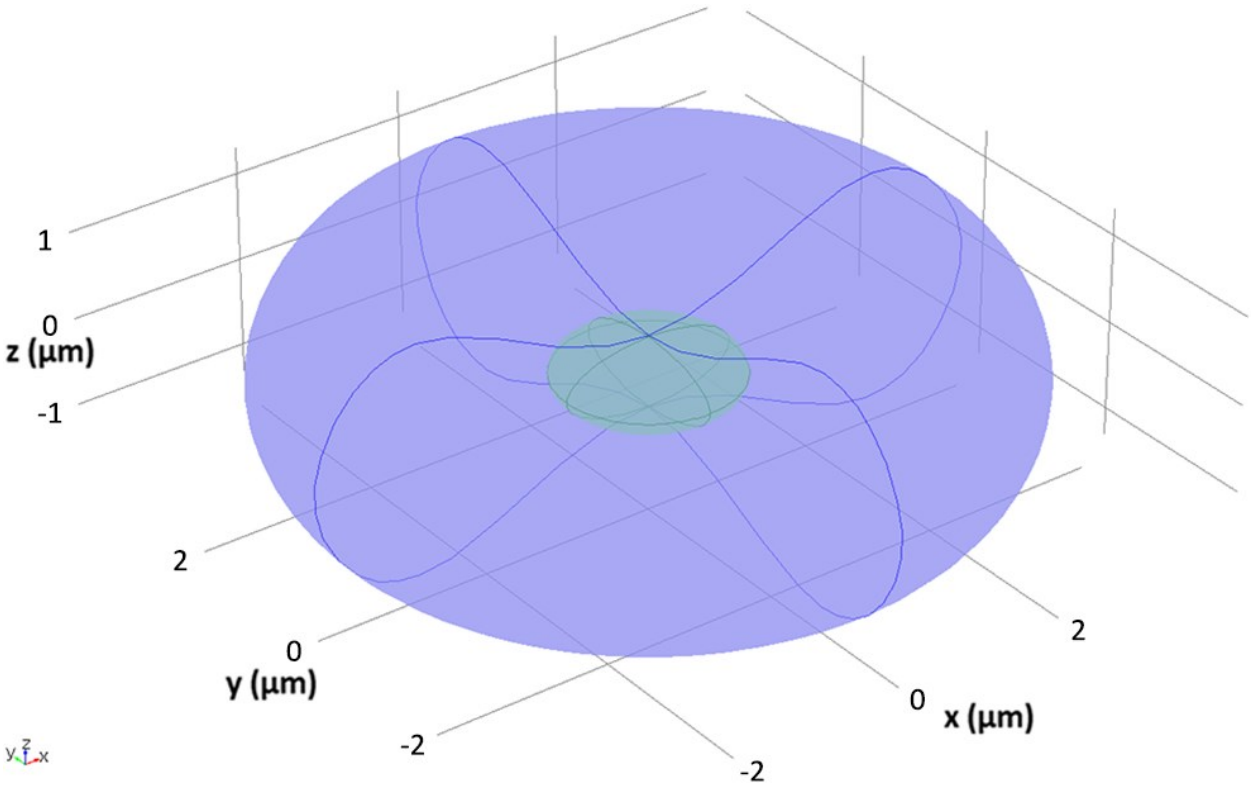

Figure 3: The 3-D shape of the simulation geometry, laser is incident from the positive z direction. The ellipsoid in the center is the simulated heat source.

Physical Model of Temperature

Ultimately, the time evolution of the temperature, $T(x, y, z, t)$, will be described by the 3-D heat equation, which can be solved via finite difference methods. The equation to be solved is as follows:

$$\rho C_p \frac{\partial T}{\partial t} - \nabla \cdot [k \nabla T] = Q_{in} \tag{11}$$

where k is the thermal conductivity of the material, and Q_{in} is the incoming heat from the laser. The heat equation is numerically solved using the initial condition that the temperature at all points is equivalent to the average human body temperature (310.15 K). In addition, the RBC exterior was maintained at a constant temperature, so the heat flux at the surface could be calculated by applying the standard heat flux equation $q_0 = h(T_{ext} - T)$ where T is the temperature inside the cell, h is the heat transfer coefficient (taken to be $250\,\frac{\mathrm{W}}{\mathrm{m}^2 K}$ to match that of a water-water interface), and T_{ext} is the external temperature held constant at $310.15\mathrm{K}$

The laser is introduced to the system in the form of a heat source, depositing heat spatially according to its fluence. A focused laser was modelled to reflect the heat distribution with maximal accuracy. The laser can be incorporated into the system by constructing the source term using the geometrical equations of that of a focused Gaussian beam.

For a Gaussian beam focused at the origin and incoming from the positive z direction, the heat deposited by the laser manifests itself as a source term of the following form:

$$Q_{in} = \frac{E_0(1 - R_c)\mu_a}{\pi w^2}\left(\frac{w_0}{w}\right)^2 \exp\left[-2\left(\frac{r_{ax}}{w}\right)^2\right] \exp[-\mu_a(z - z_s)] \qquad (12)$$

Where w is the beam's spot size parameter and is dependent on z, w_0 is the minimum beam waist size, r_{ax} is the distance from the beam axis, R_c is the reflection coefficient, z_s is the z position of the cell membrane that the laser first contacts (this is to ensure that the laser begins to attenuate at the correct location), and E_0 is the incident beam fluence. Equation 12 comes from the intensity profile in 3D of a Gaussian beam, which can be multiplied by the absorption coefficient and the

absorbance to yield the energy deposited per unit volume by the laser as a function of space. Equation 12 can also be multiplied by a time-dependent triangle function, thereby simulating a pulsed laser.

The heat source was spatially represented by an ellipsoid in the center of the RBC, as shown in Figure 3. The a and b semiaxes of this ellipsoid were $0.1\mu m$ and the c semiaxis was $0.4\mu m$. This ellipsoid was the only source of heat in this system, and Q_{in} was used to calculate the heat deposited at each point in the mesh. Mesh sizing was set to a maximum element size of $0.05\mu m$ and a minimum of $0.01\mu m$. The mesh was manually made to be much denser in the center region where the heat source ellipsoid was located.

Acoustic Pressure Model

The PA signal was calculated using FEM coupling several differential equations. This can be calculated by solving three equations simultaneously: the heat equation, the strain equation of motion, and the scalar wave equation in pressure acoustics. These can be coupled by computing the thermal expansion and then computing the resulting pressure wave generated by the RBC membrane. The temperature output of the heat equation is used to compute thermal expansion assuming the RBC interior is a linear elastic material. The thermal expansion is then used with the strain equation to compute the stresses and strains across the RBC. Lastly, the resultant thermal stresses and strains at the surface are fed into the acoustic wave equation, which finally outputs the resultant 2-D pressure distribution.

Initial values for temperature were set to 293.15K, and the heat source was defined according to the 2-D version of equation 12. The simulation was done in 2-D as opposed to 3-D in the interest of computation time, taking advantage of the axial symmetry of the system. In this simulation, the laser pulse was given a Gaussian profile as opposed to the triangle function temporal distribution from the temperature simulations. A full list of parameters can be found in Table 1 and Table 2.

Parameter	**Value**
u_a	391.65cm^{-1}
R_c	0.005
Numerical Aperture	0.7
h	$250\text{W} \cdot \text{m}^{-2} \cdot \text{K}^{-1}$
k	$456\text{W} \cdot \text{m}^{-2} \cdot \text{K}^{-1}$
ρ (RBC interior)	$1125\text{kg} \cdot \text{m}^{-3}$
C_p (RBC interior)	$3223.84\ \text{J} \cdot \text{kg}^{-1} \cdot \text{K}^{-1}$

Table 1: Simulation parameters of temperature calculation[9]

Parameter	**Value**
u_a	391.65cm^{-1}
R_c	0.005
Numerical Aperture	0.7
h	$250\text{W} \cdot \text{m}^{-2} \cdot \text{K}^{-1}$
k	$456\text{W} \cdot \text{m}^{-2} \cdot \text{K}^{-1}$

ρ (RBC interior)	$100\text{kg} \cdot \text{m}^{-3}$
C_p (RBC interior)	$3223.84\ \text{J} \cdot \text{kg}^{-1} \cdot \text{K}^{-1}$
Speed of sound (RBC interior)	$1650\text{m} \cdot \text{s}^{-1}$
Poisson's Ratio (RBC)	0.49
Coefficient of thermal expansion (RBC interior)	$1.2 \times 10^{-4}\text{K}^{-1}$
Young's Modulus	200MPa
ρ (Water)	$1000\text{kg} \cdot \text{m}^{-3}$
C_p (Water)	$4182\ \text{J} \cdot \text{kg}^{-1} \cdot \text{K}^{-1}$
Speed of sound (Water)	$1520\text{m} \cdot \text{s}^{-1}$
Ratio of specific heats	1

Table 2: Simulations parameters of pressure calculation[9]

Results

Temperature Rise with Single Pulse

The temperature at three probe points (Figure 4a) was observed during the laser illumination. The simulation was run twice with a laser focus at point α (Figure 4b) and at point β (Figure 4c). In either case, the temperature change in the case of a single pulse was not significant enough to cause thermal damage,[74] reaching a maximum value of about 317 K in the single pulse case, which would decay back to very close to the original temperature of 310.15 within a nanosecond. This decay was present when focusing the laser in both the center of the RBC (β) as well as in the case of a focus located at α. The maximal temperature at the focus was slightly higher in the case of laser

focusing at α as opposed to β. This is to be expected since laser attenuation in Eq. (2) was accounted for with the exponential z-dependent decay, so the laser heat deposition was slightly attenuated upon contacting the RBC.

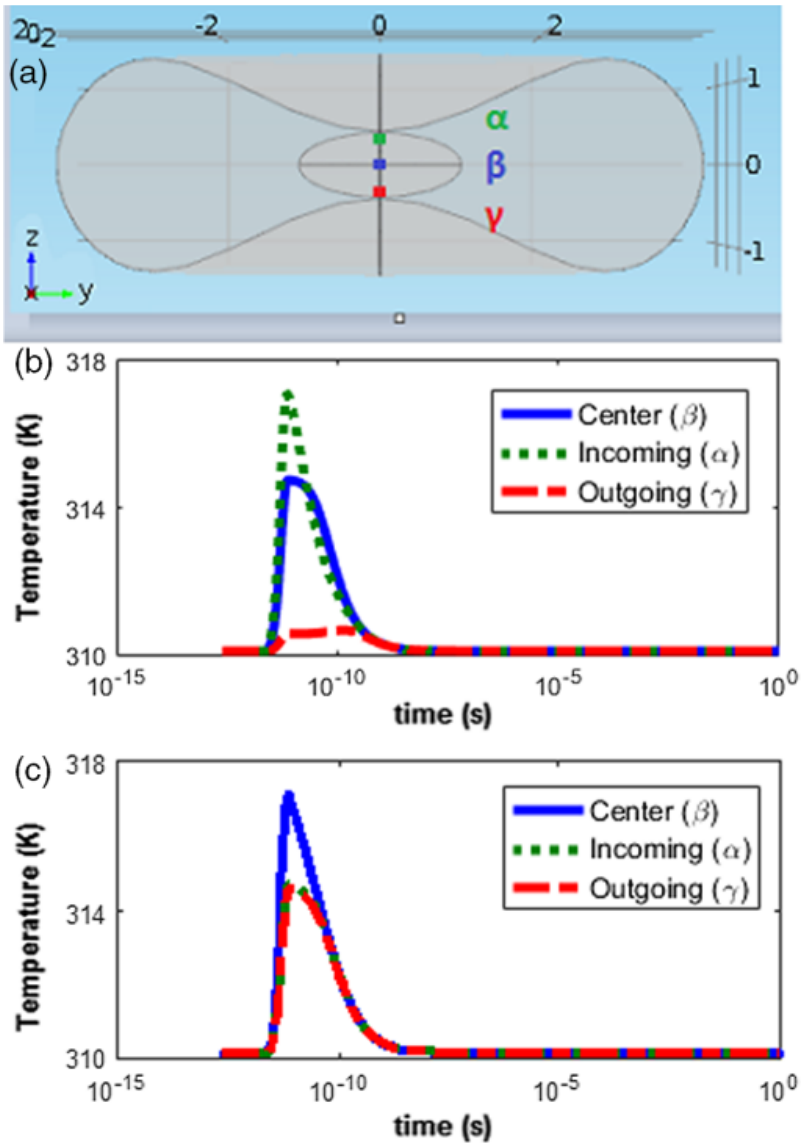

Figure 4: (a) Probe locations α, β, γ at the origin and at points $(0,0,\pm 0.032)$ within the RBC. Axis scale in μm. Laser is incident from positive z direction. (b) Temperature versus time of

probe points for a single pulse hitting the RBC focused at α. (c) Temperature versus time for a single pulse hitting the RBC focused at β[9]

Temperature Rise with High Repetition Rate

The temperature change of repeated pulses is shown in the form of the steady state temperature in Figure 5. Here the word steady state refers to the final (after a nanosecond has passed) temperature rise observed in the single pulse temperature versus time curves. That is to say, Figure 5 is the temperature versus time with the ephemeral temperature peaks from laser excitation being omitted. It can be seen that the total increase in steady state temperature is on the order of 0.01 K, which is a guarantee of thermal safety over numerous pulses.[74] It can also be seen that the temperature peaks after a certain time has reached; this is due to the heat contribution from earlier pulses diminishing at the same rate that additional pulses heat the system, leading to a steady state equilibrium temperature of < 310.165 at the laser focus.

It becomes computationally inefficient to repeat this simulation for extremely high repetition rates on the order of $\geq$ 1kHz. Therefore, for systems with higher pulse repetition rates, the steady state temperature will need to be calculated theoretically. Due to the linearity of solutions of the heat equation, the temperature distribution of multiple pulses will simply be the sum of single pulse temperature functions, $T_s(t)$, i.e. the multiple pulse temperature T can be modeled as

$$T = \sum_{i=t}^{N} T_s(t - it_d)$$

Where t_d is the time between pulses, N is the total number of pulses being simulated, and T_s is the single pulse temperature as a function of time.

Then, it is mathematically simple to obtain the multiple pulse temperature evolution given the single pulse temperature evolution by overlapping the output with translated versions of itself. The steady state equilibrium temperature for the laser should be proportional to the pulse repetition rate. This allows us to simulate a single pulse temperature profile that can be overlaped to generate a multiple pulse temperature rise.

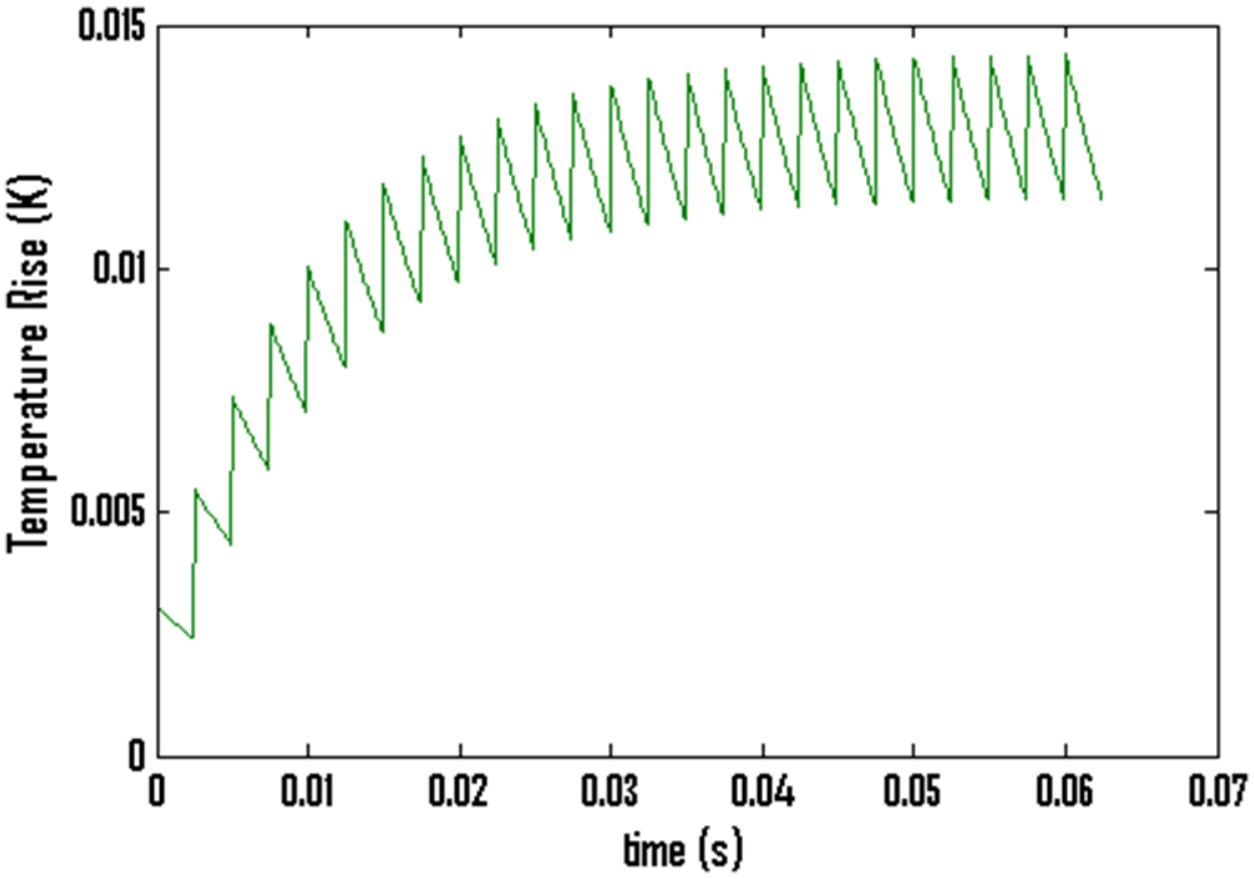

Figure 5: Steady state temperature at the focus of the laser as a function of time.[9]

Using this method, the steady state equilibrium temperature was found of the 219W picosecond laser with varying repetition rates. It was found that the picosecond laser could reach a repetition rate on the order of 100 kHz without the steady state equilibrium temperature rising significantly (3.5 K for 100 kHz). Thermal damage can be characterized by equivalent minutes at 43°C, which is dependent on exposure time.[75] The 219W picosecond laser does not reach 43°C in steady state; it can be concluded that to have temperature rises high enough to cause heat damage (assuming exposure times of a few seconds) to the RBCs, the pulse repetition rate will need to be increased to the order of several hundreds of kHz.

The steady state temperature rise for a femtosecond (830 nm, pulse duration of 0.2 ps, 1 kW fluence, and 75MHz repetition rate) laser was also examined. The steady state equilibrium temperature was calculated to be 6.3K. This is much larger than the temperature rise of the 219W picosecond laser at 400Hz and even exceeds the theoretical steady state equilibrium temperature of the laser with a 100kHz repetition rate. As a result, the thermal safety of a 100kHz laser with a fluence can be more confidently guaranteed as compared with the femtosecond laser at 75MHz; the exposure time under which thermal safety with this laser can be guaranteed will be lower than that of the picosecond laser. In addition to this, the absorption of hemoglobin at the femtosecond laser wavelength (830 nm) is lower than at the femtosecond laser wavelength (532 nm), so the signal strength per watt of fluence will be weaker with this laser.

Spatial Distributions of Temperature Rise in a Single Cell

The spatial distribution of the temperature is also relevant and can be analyzed via the generation of volume temperature plots. In the single pulse scenario, it is easiest to analyze the spatial

temperature distribution at the peak of the temperature rise. Figure 6 shows the spatial temperature distribution with time with a single pulse illumination. The temperature rise is very localized in a small part around the center of the RBC.

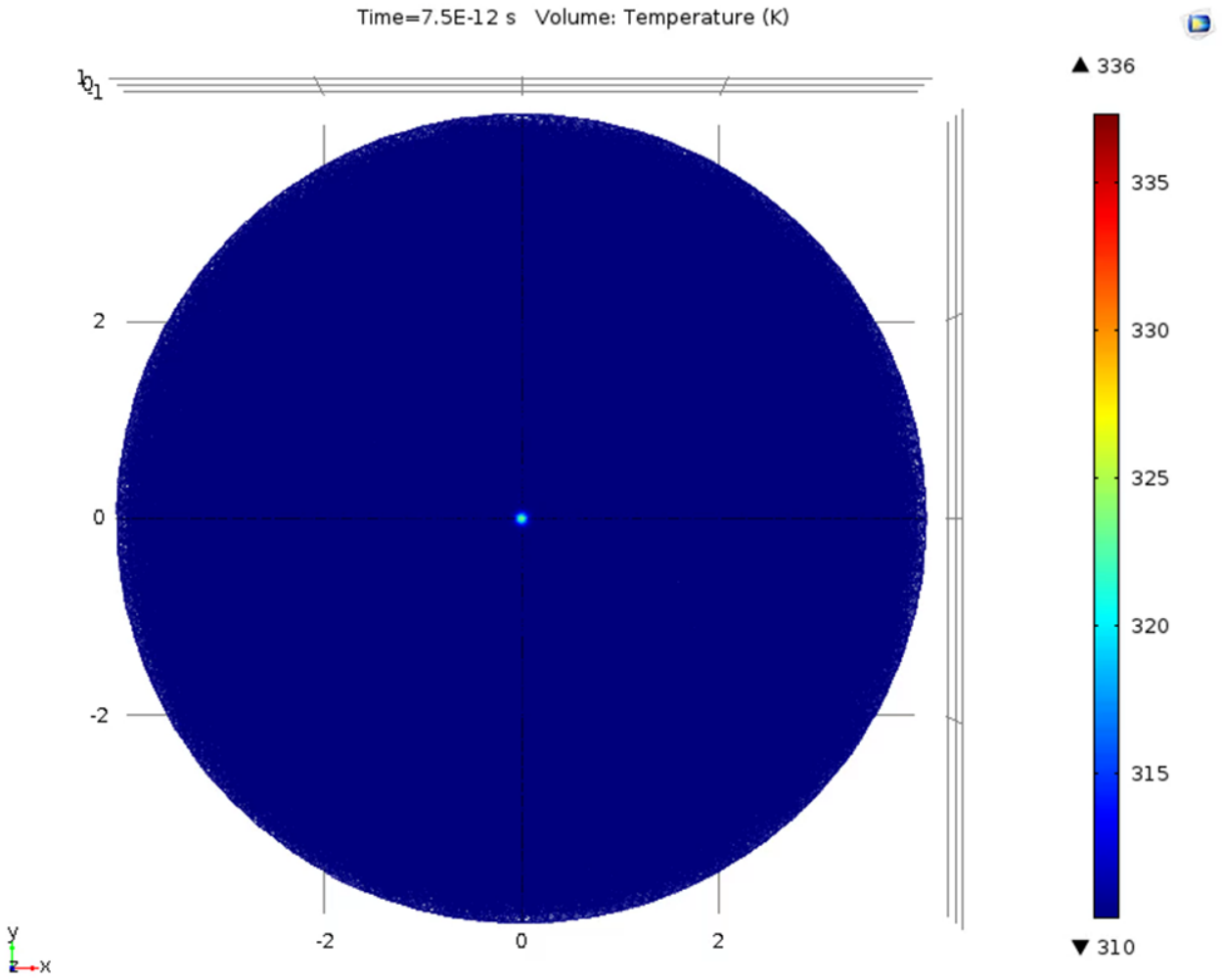

Figure 6: The spatial distribution of the temperature at the time of peak temperature rise through single pulse illumination.[9]

This is shown in more detail in Figure 7 where the location of the highest temperature is displayed (the rest of the cell did not see a significant difference from the initial temperature rise at the time

of peak temperature at the focus). In this case, it is clear to see that some areas actually exceed the temperature at the focal point, as illustrated by the red coloring. This can be attributed to the fact that the focus lies toward the top of the figure and is not directly in the center; as a result, there is a larger heat sink in the negative z direction than there is in the positive z direction. The positive z portion of Figure 7 then does not have as large a capability of dissipating incident heat away from peaks. Nevertheless, this peak is still ephemeral and only on the order of a 10K rise from equilibrium, still not enough to cause thermal damage to the RBC when the duration is considered. The change in temperature is localized to the area around the focus, which would explain its fast dissipation and decrease. However, the temperature did not see any significant rise from the equilibrium.

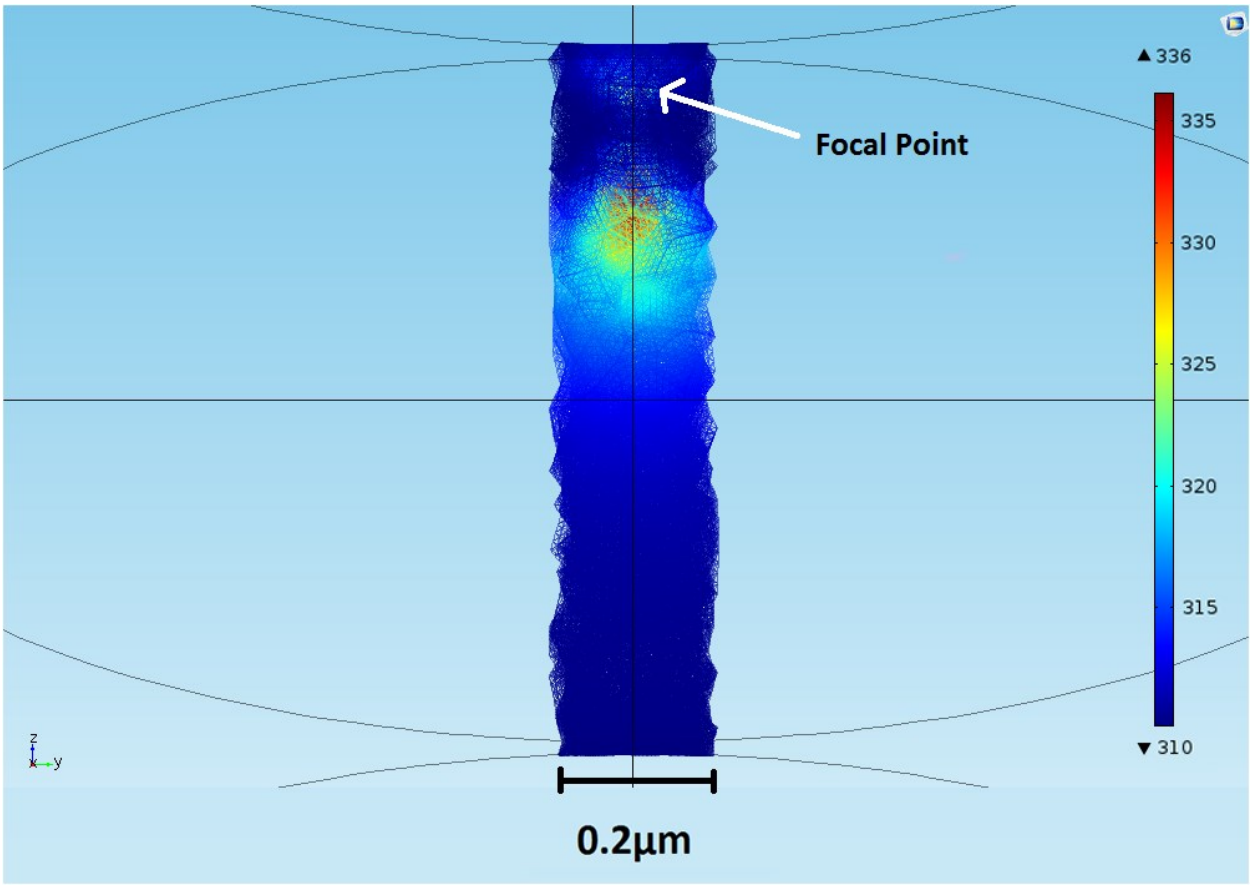

Figure 7: Peak temperature rise in center region of the RBC after repeated pulsed illumination by laser. Laser is incident from positive *z* direction. Colorbar legend is in Kelvin.[9]

In the case of multiple pulses, it makes the most sense to analyze the maximal equilibrium temperature as opposed to the ephemeral peaks (which were ill-behaved due to the larger time-step size in computing this many pulses). While there is not a drastic change (~0.1µK) in the temperature in this context, it is still useful to illustrate this spatial distribution to analyze the pattern of heat flow in the cell. This is shown in Figure 8 where it can be seen that the heat dissipates outward from the center and that the ends of the cell remain at the environmental temperature even in the face of a 400-Hz laser. he simulation shows that under repeated irradiation

by a laser, the temperature rise in an RBC is ~0.1μK, not large enough to cause thermal damage in nPAT.

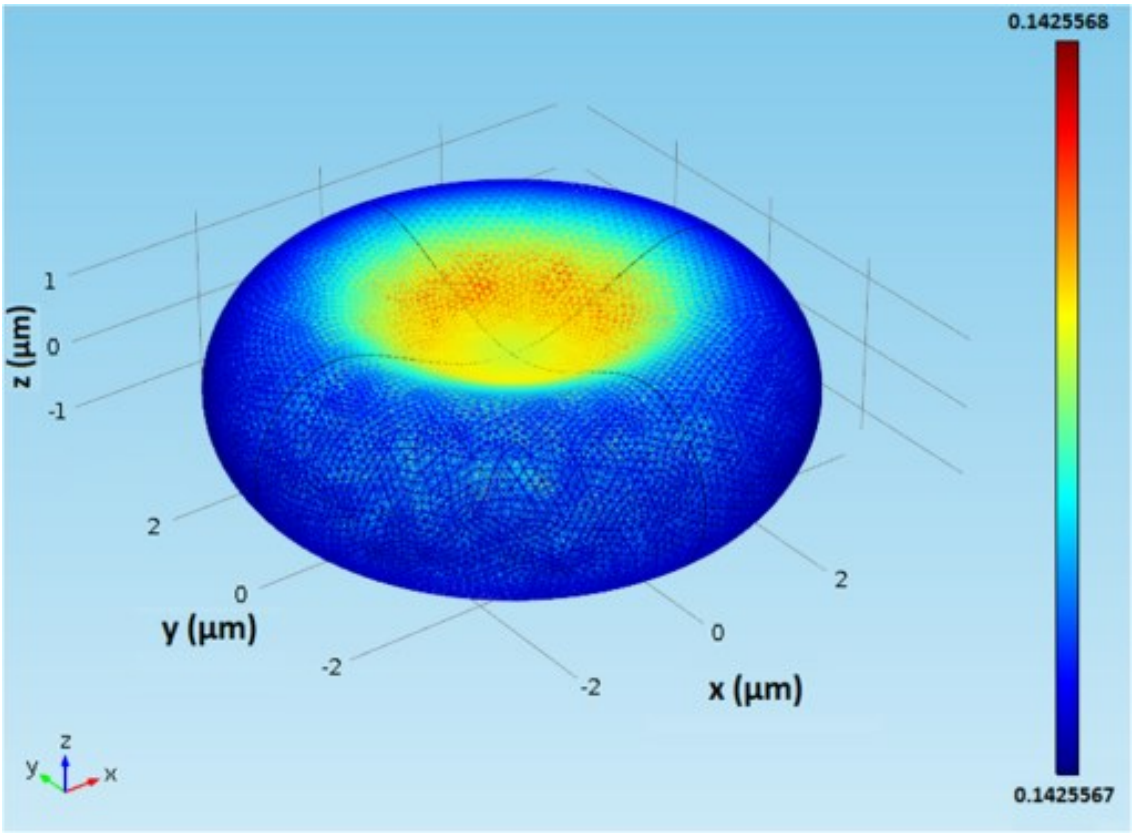

Figure 8: Spatial distribution of temperature deviation (from initial temperature) immediately following (0.001 s) after the final pulse in the multiple pulse temperature simulation. Colorbar legend is in Kelvin. It is to be noted that the temperature scale here is much finer than that from previous figures, not even covering an entire μK in difference.[9]

This simulation was also repeated for multiple pulses striking the RBC, such that the temperature evolution could be studied over time. As shown already in Figure 5 the temperature following repeated pulsed illumination did not result in more than a 10 mK change in temperature rise. The peaks did not last longer than single nanoseconds, so they were omitted in the context of data

presentation. This data set shows that the temperature at the focus does not show a significant rise during PA imaging and should be indicative of the safety of the nPAT system at the specified fluence levels.

Signal Generation and Detection

In the 2-D case, the RBC was encased in a coupling medium (which was taken to be water). PA wave amplitude was monitored at a probe point located at (8,0) using the center of the RBC as the origin, as shown in Figure 9a. It can be seen in Figure 9b that the generated PA pressure at this probe point from the laser pulse of the same fluence as in the temperature simulations reaches more than 2.5 kPa in magnitude. To properly measure this signal, the noise of the system must be known, but these simulation results show that at this probe point a signal of appreciable magnitude will be generated by the laser pulse.

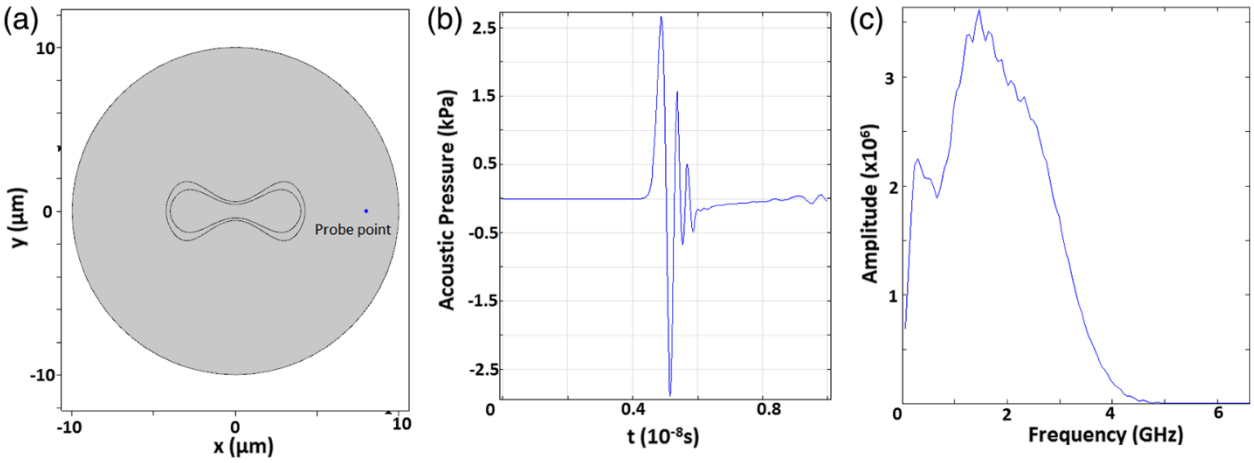

Figure 9: (a) Location of probe point relative to RBC, (b) PA pressure at probe point versus time, and (c) FFT of the signal showing frequency spectrum of the signal.[9]

The composition of the signal can be analyzed via spectral analysis. This is done in Fig. 7(c), which shows the frequency spectrum of the signal. The peak of this frequency spectrum occurs at a frequency of 1.47 GHz, with signals of considerable amplitude at frequencies as high as 3.5 GHz. The axial resolution, R_a is given as

$$R_a = \frac{0.88 v_s}{f}$$

where f is the frequency.[39] Using the speed of sound in water and a frequency as high as 3.5 GHz, yields $R_a = 373\text{nm}$ which is suitable for nanoscale imaging. The spatial propagation of the PA waves is also important to analyze, and the pressure waves can be represented in a surface plot for particular times. In the context of ensuring that the PA signal from the laser is large enough to measure, the time of highest PA signal amplitude at the probe point is a sensible time at which to examine propagation. A plot of the pressure distribution is given in Figure 10. The wave front can be seen after it has propagated outward from the center of the RBC (at which the laser is focused), and the pressure wave is seen to be originating from the center of the cell symmetrically outward.

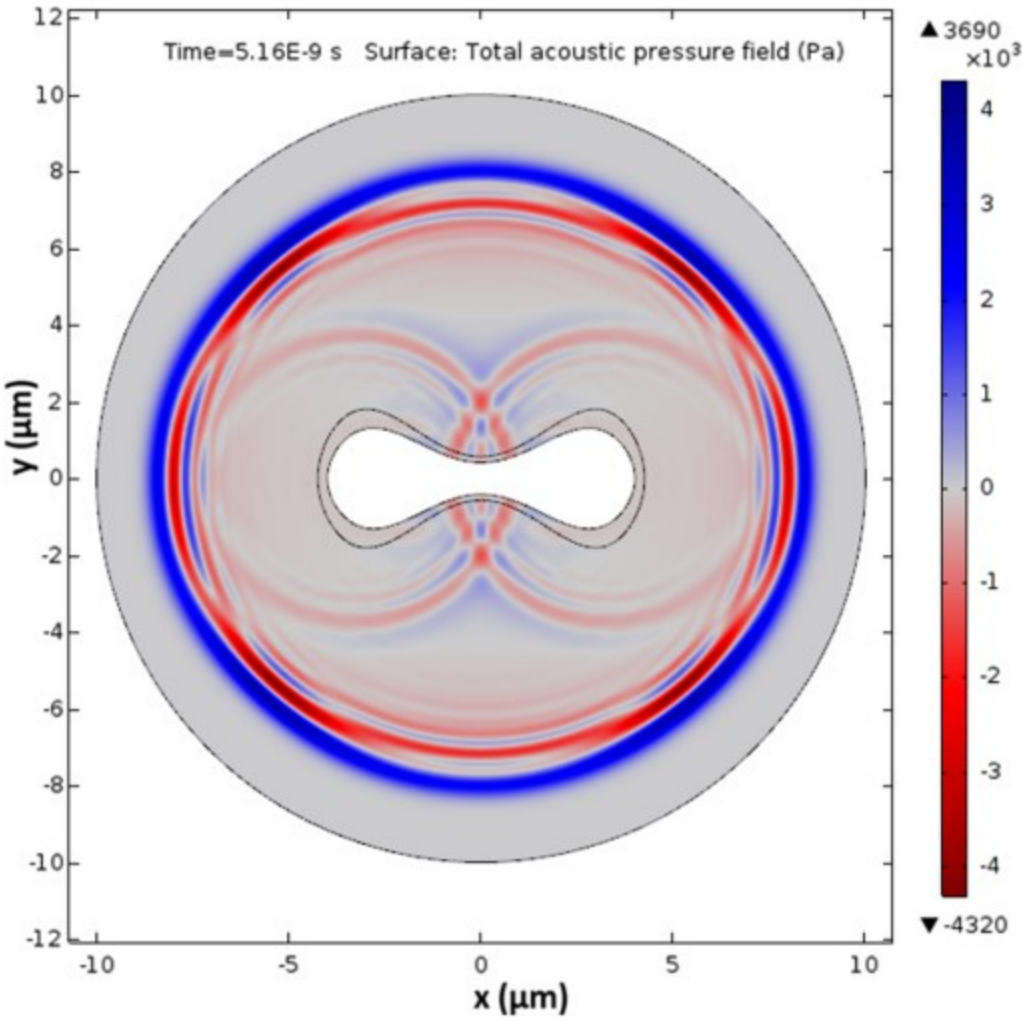

Figure 10: PA pressure spatial distribution at time of peak amplitude at probe point, RBC shown in white; the remaining area is all modeled as a uniform continuity of water. Units of x and y are in µm.[9]

Discussion

To cause thermal damage to biological tissue, the temperature must have an instantaneous rise of $\geq$ 150K or a cumulative temperature rise of 43 K for a sustained period of time.[13,75,76] Simulations of the temperature change induced by a laser with 219-W peak power show that the temperature

rise is not high enough to induce thermal damage in an RBC. This is demonstrated by the fact that a laser focused directly onto the RBC does not display a large temperature change once the heat equation has been solved with FEM. The PA signal generated by such a pulse was shown to be on the order of kPa, so these simulation results show that the laser should be capable of generating a measurable PA signal while at the same time ensuring that the RBC does not become damaged due to high temperature rises.

These simulations demonstrate the feasibility of an nPAT system to generate PA images of an RBC. Such a system could be used to look into RBCs with high resolution without the need for contrast agents (due to the high absorption coefficient of hemoglobin). It is believed that nPAT will be a modality for disease diagnosis and understanding of cell biology at the nanometer-level.

The single-pulse case maximum fluence can be taken to be as high as on the other of 1 kW. In this situation, the ephemeral temperature rise immediately following excitation can be up to 5 K, but the steady state temperature rise is still quite low. As RBC thermal damage depends greatly on exposure time[74], it is predicted that this should not result in thermal damage to the RBC. However, the instantaneous temperature rise with a MW fluence laser was several hundreds of degrees. Therefore, the maximum fluence for a single pulse should be on the order of 1 kW for the RBC to avoid thermal damage.

The single pulse maximum allowed repetition rate was found to be 100 kHz for a 219-W laser (532 nm and 5-ps pulse duration), with a steady state temperature rise of 3.5 K. In contrast, a femtosecond laser at 830 nm with a repetition rate of 75 MHz was found to induce a temperature rise on the order of 6 K. The absorption of the 532-nm laser is also much larger in hemoglobin, so

it could be suggested that the signal generated by each pulse would be of stronger amplitude than in the 830 nm case.

Now that thermal safety of nPAT has been established, the next chapter examines what nPAT imaging may look like as well as derives theoretically many of the key imaging parameters associated with nPAT imaging. This builds upon the work of Chapter 1 by extending modelling beyond temperature and 2D signal generation, introducing work on resolution and sensitivity estimates as well as creating a simulation workflow to model nPAT imaging itself.

Chapter 3: Nanoscale photoacoustic tomography for label-free super-resolution imaging: simulation study

Overview

In this chapter, modelling is extended to assess the imaging parameters of nPAT. Expanding on Chapter 2, this chapter develops modelling of the sensitivity and resolution of nPAT, and presents a simulation workflow through which thermoacoustic imaging at nanoscale lengths is possible. Resolutions higher than the optical diffraction limit are often desired in the context of cellular imaging and the study of disease progression at the cellular level. However, three-dimensional super-resolution imaging without reliance on exogenous contrast agents has so far not been achieved. This chapter presents nanoscale photoacoustic tomography (nPAT), an imaging modality based on the photoacoustic effect. nPAT can achieve a dramatic improvement in the axial resolution of the photoacoustic imaging. The theoretical resolution and sensitivity of nPAT are derived and it is demonstrated that nPAT can achieve a maximum axial resolution of 9.2 nm. It is also demonstrated that nPAT can theoretically detect smaller numbers of molecules (~273) than conventional photoacoustic microscopy due to its ability to detect acoustic signals very close to the photoacoustic source. nPAT imaging of malaria-infected red blood cells (RBCs) is simulated using digital phantoms generated from real biological samples, showing nPAT imaging of the RBC at different stages of infection. These simulations show the potential of nPAT to nondestructively image RBCs at the nanometer resolutions for in vivo samples without the use of exogenous contrast agents through modelling. Simulations of nPAT-enabled functional imaging show that nPAT can yield insight into malarial metabolism and biocrystallization processes. The experimental realization of nPAT has important applications in biomedicine.

Introduction

Super-resolution imaging has pushed past the optical diffraction limit and revolutionized optical imaging at the cellular and molecular levels.[77] Many imaging modalities have been successful in achieving high-resolution imaging of biological samples, meeting or exceeding resolutions required for single-cell imaging.[13,78,79] Conventional super-resolution imaging techniques work by first labeling the region of interest with fluorophores, and then precisely determining the distribution of these fluorophores to form an image.[80–82] The high resolution provided by fluorescence imaging techniques has been a crucial feature leading to multiple biomedical discoveries[83–86] by probing at length scales previously inaccessible to optical imaging. However, fluorescence-based super-resolution techniques rely on exogenous fluorophores to image at high resolutions. Therefore, these techniques often suffer from limited imaging times due to photobleaching and can result in sample damage through phototoxicity effects. Lastly, optical scattering in tissue remains a large problem, which limits imaging depth.[35]

One important context in which high-resolution imaging can yield important biomedical insight is that of malarial development in red blood cells (RBCs). Malaria remains a worldwide problem causing >400; 000 deaths each year. Therefore, the understanding of malarial metabolism and development has global impetus.[87] Entering the blood stream from the bite of an infected *Anopheles* mosquito, the malaria parasite (*Plasmodium falciparum*) infects human RBCs, where it metabolizes hemoglobin (Hb) and grows, before eventually causing cell membrane rupture and enters the blood stream. Invasion by *P. falciparum* can be characterized in infected RBCs via the presence of hemozoin (Hz). The malaria parasite, while inside the RBC, consumes up to 80% of

the host cell's Hb.[88] This Hb is digested by the parasite, releasing toxic hematin byproducts. To prevent cell lysis, the parasite processes these toxic heme groups via biocrystallization into Hz crystals, which are inert.[89–91] It is well known that the mechanism of the action of frontline anti-malarial drug Chloroquinone is the inhibition of the Hz formation in the digestive vacuole of malaria.[92] Important information regarding malarial metabolic activity and drug efficacy can be gained by quantifying Hz and Hb concentrations throughout the cell. However, the erythrocytic development of malaria happens on length scales much smaller than the 8-μm diameter of erythrocytes. *P. falciparum* merozoites are typically 1.5 microns in diameter,[93] and metabolized molecules such as Hb have an average diameter of 5.5nm.[94]

Therefore, to image malarial metabolism and Hb digestion progress, resolutions well below

1.5μm are desired, as resolutions approaching the size of single Hb molecules can provide important insight into macromolecular processes such as Hz biocrystallization and effectiveness of antimalarial agents. The most common form of malarial micros- copy remains blood films, as major parasite species are distinguishable in these tests. However, blood films require the removal of blood from the host, and additional staining followed by imaging via conventional light microscopy. Blood film microscopy cannot perform dynamic imaging and has only diffraction limited resolutions. Therefore, it is not enough for the visualization of molecular processes. Super-resolution, label-free imaging as required for research purposes is not achievable with blood film microscopy.

PAM is a promising biomedical imaging modality, which can overcome the traditional limits of optical diffusion by taking advantage of the photoacoustic effect and, instead, by detecting an

optically induced acoustic signal.[35] However, PAM's axial resolution is limited because conventional piezoelectric transducers have difficulty in detecting GHz frequency acoustic signals, which encode higher resolution information. Whereas progress has been made in the development of high-frequency transducers[95,96], transducers that can sensitively detect signals in the range of several GHzs are not commonly available commercially. Among high bandwidth transducers that are available, high acoustic frequency attenuation due to the large distance between the source and the detector remains a problem.[97]

Consequently, there does not yet exist an imaging modality that can achieve super-resolution imaging without reliance on fluorescent labeling and overcome high optical scattering effects in tissue. Label-free super-resolution imaging remains a technological challenge. Here the capabilities of nPAT are presented, as a biomedical imaging modality that can achieve nanometer-level resolutions and optical contrast without reliance on fluorescent labeling. nPAT takes advantage of the photoacoustic effect to generate ultrasound signals generated via optical absorption. In this way, nPAT encodes optical contrast information in an ultrasonic signal. This high-frequency ultrasound can yield super-resolution (better than 200 nm) imaging in the axial direction of laser excitation. This is accomplished by detecting acoustic signals in the GHz range by taking advantage of pump–probe techniques commonly used in picosecond ultrasonics.

According to developed models, nPAT is capable of high- resolution in vivo imaging of malarial development at different stages. nPAT can yield anatomical and functional information as the distribution of Hb throughout the cell can reveal both the outline of malarial parasites as well as their metabolic activity. In this chapter, theoretical resolution and sensitivity of the nPAT imaging

technique is calculated. nPAT imaging of malaria-infected RBCs in both early and late stages of the blood-stage life cycle is then simulated. The imaging features of nPAT are then compared with those of x-ray microscopy and the simultaneous anatomic and functional imaging capabilities of nPAT are demonstrated.

Theory of Nanoscale Photoacoustic Tomography

Principle of Nanoscale Photoacoustic Tomography

nPAT uses two laser beams for signal generation and detection. The excitation beam is tuned to an absorbance peak of the primary molecule being used as a contrast agent (532 suffices in the case of Hb). The excitation and detection wavelengths are kept below the ANSI safety limit if dynamic imaging of biological samples is desired. The detection beam is ideally tuned to a wavelength of maximum reflectance but can also be of the same wavelength as the excitation wavelength. Pump–probe detection of the excitation beam-induced acoustic signal is then performed in the axial direction.[47,98] Optical detection as opposed to detection by an ultrasound transducer enables nPAT to detect extremely high-frequency signals.[47,99–102] This allows for nPATs axial resolution to surpass that of conventional PAM as the axial resolution is dependent on the bandwidth of ultrasound detection.[39] This extends the theoretical resolution of nPAT into the nanometer range. The high resolution achieved by nPAT is not a result of optical focusing, but instead the extremely high bandwidths that are achievable in laser-based pump–probe systems. As a result, the resolution of nPAT should ultimately only depend on the excitation pulse duration and sound velocity.

The experimental setup of nPAT requires the use of a pulsed laser, several beam splitters, two focusing lenses of sufficiently high numerical aperture, an optical delay line, mirrors, and detection

electronics (e.g., photodiodes). The laser beams are close to confocal on the sample, with the pump being less finely focused than the probe to enable a large axial field of view.

Typical transducers can detect photoacoustic signals on the order of tens of MHz. However, the physical photoacoustic signal is theoretically broadband, with relevant contributions in the GHz range for excitation pulses on the order of picoseconds, as demonstrated in Chapter 2. These GHz signals contain information about higher resolution imaging, and the ability to detect them is directly tied to the resolution of the final image. Therefore, to detect such high-frequency pulses and obtain nanometer resolution in the axial direction, a piezoelectric transducer is insufficient. For this reason, nPAT uses a pump–probe signal detection method, allowing for the detection of high bandwidths.

Resolution of Nanoscale Photoacoustic Tomography

To calculate the maximum achievable resolution of nPAT, the excitation pulse of the laser is first considered. For a Gaussian laser pulse, the intensity as a function of time can be written as

$$I(t') = \frac{E_0}{\theta} \exp\left[-k\frac{t'^2}{\theta^2}\right] \tag{13}$$

where $t' = 0$ at the instant of maximum intensity, E_0 is the fluence as in Chapter 2, and $k = 4\ln 2$. It is assumed that this laser pulse is incident on a point absorber. At some distance r from the point absorber, the center of the resultant acoustic pulse will arrive at a time $t = t' + r/v_s$.

Let $\tau = \frac{t-\frac{r}{v_s}}{\theta}$. Then, substituting this into equation 13:

$$I(\tau) = \frac{E_0}{\theta}\exp\left[\frac{k\left(-t-\frac{r}{v_s}\right)^2}{\theta^2}\right] = \frac{E_0}{\theta}\exp[-k\tau^2] \quad (14)$$

The photoacoustic pressure produced by a point source as a function of r and τ has been derived by Calasso et al.[40] In the case of delta function heating and linear thermal expansion, it is given as

$$P(\tau, r) = \frac{\sigma\beta}{4\pi\theta C_p r}\left[\frac{\mathrm{d}}{\mathrm{d}\tau}I(\tau)\right] \quad (15)$$

Combining equations 14 and 15 yields

$$P(\tau, r) = \frac{E_0\sigma\beta}{4\pi\theta^2 C_p r}\left[\frac{\mathrm{d}}{\mathrm{d}\tau}\exp(-k\tau^2)\right] = -\frac{E_0\sigma\beta k\tau}{2\pi\theta^2 C_p r}\exp(-k\tau^2) \quad (16)$$

Where all variables are as in equation 7. Equation 16's maxima and minima can be found by taking its derivative

$$\frac{\mathrm{d}}{\mathrm{d}\tau}P(\tau, r) = [1-2k\tau^2]\frac{E_0\sigma\beta}{2\pi\theta^2 C_p r}\exp(-k\tau^2)$$

Which has maxima and minima at $\tau = \pm\frac{1}{\sqrt{2k}}$. With respect to t, this corresponds to maxima/minima of $t = \pm\frac{\theta}{\sqrt{2k}} + \frac{r}{v_s}$. The Raleigh criterion can be applied to these values to determine the maximum theoretical resolution. the temporal diffraction limit of two such point sources will occur when the minimum pressure of one point signal coincides with the maximum pressure of another. This is equivalent to the distance between the maximum and minimum of the photoacoustic point source. Time between the maxima and minima is then $\frac{2\theta}{\sqrt{2k}}$. The Rayleigh

spatial resolution is given by converting this time into a distance by multiplying by the sound speed. Then, the maximum theoretical resolution achievable by a point source is given as

$$R = \frac{2\theta v_s}{\sqrt{2k}}$$

For a pulse duration of 7ps and $v_s = 1593.3\ \mathrm{m/s}$, which corresponds to a maximum achievable axial resolution of 9.2nm.

Sensitivity of Nanoscale Photoacoustic Tomography

The sensitivity of nPAT is an important parameter in the assessment of its potential. Whereas an ultrasonic transducer benefits from higher sensitivities at the cost of lower bandwidth, acoustic detection via a laser pulse is the opposite scenario. The sensitivity of probe laser detection will be less than that of an ultrasound transducer at comparable distances from the source. The probe beam acts similar to a high-bandwidth transducer, and detects acoustic waves at the point at which it is focused. In this way, the focused probe beam can detect acoustic waves traveling through the focal point, and the pump beam can generate these acoustic waves. The two beams, pump and probe, can be focused very close to each other, making it easier to detect an nPAT signal very close to the source as compared with PAM. The sensitivity of nPAT can be estimated based on the theoretical change in refractive index caused by the acoustic pressure.

It was assumed that the sound wave (for simplicity's sake) is a box function in one-dimension and propagates outward in three-dimensions. Then, the resultant change in refractive index induced related to the wave intensity is given as[103]

$$\Delta n_0 = \frac{1}{2}\hat{p}n^3\sqrt{\frac{2I_a}{\rho v_s^3}} \tag{17}$$

Where $\hat{p}$ is the photoelastic tensor, n is the refractive index, and I_a is the acoustic intensity. The acoustic intensity is equal to the acoustic power divided by the distributed area. For a spherical wave, this corresponds to

$$I = \frac{\text{Power}}{\text{Area}} = \frac{\frac{Ap^2}{\rho v_s}}{A} = \frac{p^2}{\rho v_s} \tag{18}$$

where A is the surface area of the sphere, and p is the pressure. Then combining equations 17 and 18,

$$\Delta n_0 = \frac{1}{2}\hat{p}n^3\sqrt{\frac{2p^2}{\rho^2 v_s^4}} = \frac{\frac{\sqrt{2}}{2}\hat{p}n^3 p}{\rho v_s^2} \tag{19}$$

where $\hat{p}$ is related to the material parameter M as follows[103]

$$M = \frac{\hat{p}^2 n^6}{\rho v_s^3} \tag{20}$$

It is assumed that M for water and blood plasma remains the same. It is also known that, for blood plasma, $\rho = 1025\text{kg/m}^3$, $v_s = 1549.3\text{ms}^{-1}$, $n = 1.333$ for light of 532nm wavelength. This corresponds to $\hat{p} = 10.5$.

The simulations from Chapter 2 suggest that acoustic waves produced by RBCs can reach amplitudes as high as 2500Pa, for such a pressure, the resulting change in the refractive index is $\Delta n_0 = 1.775 \times 10^{-5}$. n pump–probe imaging, the corresponding reflectance change, δR, induced by Δn_0 is the probed quantity and can be given by evaluating the usual Fresnel equation

$$\delta R = R_2 - R_1 = \left|\frac{n_a - (n_b - \Delta n_0)}{n_a + n_b}\right|^2 - \left|\frac{n_a - n_b}{n_a + n_b}\right|^2 \tag{21}$$

Where n_a is the refractive index in the air (~ 1) and n_b is the refractive index in the medium.

Combining equations 19 and 20 with equation 21 yields $\delta R \approx -2.17 \times 10^{-6}$. If instead it is needed to go in the opposite direction and calculate the minimum detectable pressure (i.e., the sensitivity of nPAT), then isolating for pressure is necessary. Rearranging equation 21,

$$\sqrt{\delta R + \left|\frac{n_a - n_b}{n_a + n_b}\right|^2} = \left|\frac{n_a - (n_b - \Delta n_0)}{n_a + n_b}\right| \tag{22}$$

As $n_a - n_b = 0.333$ for a medium of blood plasma, and the magnitude of Δn_0 will not exceed 0.333 (this would correspond to a pressure of 46 MPa, which is unreasonably high), the right side

will be negative prior to taking the absolute value. Then by combining equations 19 and 20 with equation 22 and re-arranging yields an expression for pressure as follows

$$\sqrt{\delta R + \left|\frac{n_a - n_b}{n_a + n_b}\right|^2} = \left|\frac{n_a - (n_b - \Delta n_0)}{n_a + n_b}\right|$$

$$-(n_b + n_b)\sqrt{\delta R + \left|\frac{n_a - n_b}{n_a + n_b}\right|^2} - n_a + n_b = \Delta n_0 = \frac{\frac{\sqrt{2}}{2}\hat{p}n^3 p}{v_s^2}$$

$$p = \frac{\sqrt{2}\left(-(n_b + n_b)\sqrt{\delta R + \left|\frac{n_a - n_b}{n_a + n_b}\right|^2} - n_a + n_b\right)\rho v_s^2}{\hat{p}n_b^3} \quad (23)$$

The pump–probe method's sensitivity to reflectivity is theoretically limited to a reflectivity ratio change on the order of -10^{-6}, which corresponds to a reflectance change of $\delta R = 2.04 \times 10^{-8}$.[104] Substituting this into equation 23 yields a noise equivalent pressure (NEP) of 21Pa, whereas ultrasound transducers can detect pressures as small as < 1Pa.[105]

The number of molecules (NEN) required to generate this pressure, known as the noise equivalent NEN, is given by dividing this pressure by the pressure generated by a single molecule, p_s.[36] For Hb, this pressure is given by the equation

$$p_s(r) = \frac{E_0 \sigma_{Hb} \beta}{4\pi\theta^2 C_p r} \quad (24)$$

Assuming perfect energy conversion from laser light to pressure. However, equation 24 does not hold for indefinitely small pulse widths, and at pulse widths extending to shorter than stress confinement, the dependence on pulse-width vanishes, with shorter pulse widths no longer increasing signal amplitude.[36] As compared with PAM, which uses an ultrasonic transducer, nPAT will benefit from typically higher NEN due to the fact that nPAT's pump–probe detection method allows for r to be very close to the source itself. However, laser-based detection is less sensitive than an ultrasound transducer at comparable distances from the source. For pulse widths comparable with PAM (30 ns) and fluence operating at the ANSI safety limit, the NEN for $r =$ 1μm is 292, which is a lower NEN than typically reported in PAM. This number can be further decreased by increasing the fluence or shortening the pulse.

Methods

Sample Selection

To demonstrate the imaging capabilities of nPAT, simulation geometries based on x-ray microscopy image data obtained and generously provided by Dr. Saibil of Hale et al.[106] These samples were chosen because they were obtained with x-ray microscopy and can serve as extremely high-resolution digital phantoms for physical simulations. Also, these samples show the malaria parasites clearly, in addition to the parasitophorous vacuole, digestive vacuole, and RBC membrane. The samples also show the RBC at different life cycle stages. The simulation geometries are outlined below.

Simulation Geometry

Simulations were performed on experimental data obtained by Hale et al.[106] via soft x-ray microscopy. These images depict a malaria-infected RBC treated with the broad-spectrum cysteine protease inhibitor E64. This treatment allows for the rupture of the parasitophorous vacuole membrane (PVM) but prevents RBC membrane rupture. The result is merozoites that would otherwise egress, being trapped in the RBC.[107,108]

These tomograms could then be used to construct a simulation geometry that was suitable for the photoacoustic imaging of the specimen. A sample slice from the segmented tomogram is shown in Figure 11a. This slice was transformed into a simulation geometry by filling in the segmented regions and assigning to each color a different absorption coefficient. A sample slice of the resultant geometry is shown in Figure 11b, along with the axially focused laser beam and the direction in which it scans. Scanning along the slice yields a series of 1-D images that can be combined and segmented to form a 2-D image. This can be repeated over the entire 3-D x-ray tomogram to yield a series of 2-D images, which can be combined into a 3-D image. Hale et al.[106] also used x-ray microscopy to image earlier stage malaria within RBCs by fixing with selective PKG inhibitor compound 2 (C2) to reversibly inhibit egress prior to the rounding up stage. These 3-D tomograms could also be similarly utilized and segmented to simulate nPAT imaging of malaria at this earlier stage. Simulations were performed on this geometry in the same way as outlined above for the E64 fixed schizonts. The C2 tomograms consisted of 43 slices, and the E64 tomograms consisted of 27 slices. For both geometries, the distance between each slice was 80 nm and the pixel size in each slice was $16 \times 16\mu m$.

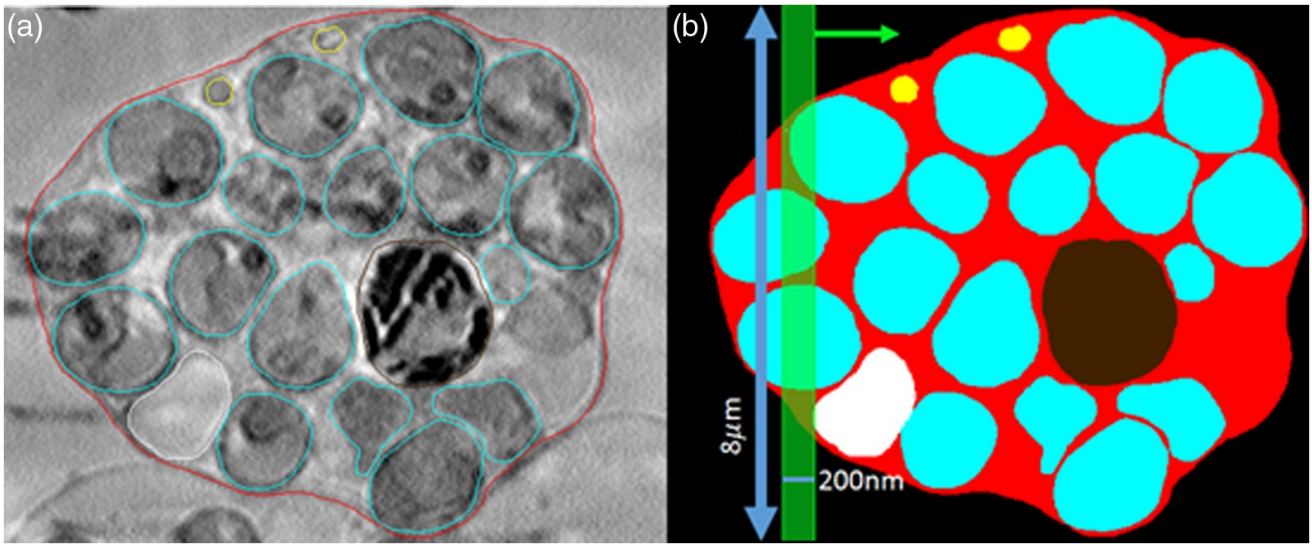

Figure 11: (a) Segmented slice from E64 treated RBC infected with malaria imaged with x-ray microscopy, (b) simulation geometry slice showing the laser spatial dimensions and scan direction; each color of the RBC is assigned a different absorption coefficient. Green bar represents the laser, and green arrow is the scanning direction. Cyan: merozoite membrane, yellow: PVM, brown: digestive vacuole, red: RBC membrane, and white: additional vacuole, as identified by Hale et al.[106,109]

Wave Propagation

Once the simulation geometry was created, the k-wave[110,111] toolbox in MATLAB was used to simulate the propagation of all waves throughout the simulation. This toolbox solves the photoacoustic wave equation in both time and space using a pseudospectral method and therefore allows for the modeling of acoustic wave propagation in a user-friendly and computationally efficient manner.

The k-wave simulation was run in 2-D for the E64 simulation model to conduct slice-by-slice imaging of the RBC. The detector was placed at the top of the excitation laser pulse. To simulate a focused probe beam of 200 nm, signals arriving at a detector array at the top of the laser beam in Figure 11b were averaged in time to yield a single waveform. The resulting pressure versus time A-line scans were set beside one another for the reconstruction of initial pressure in each slice for simple morphological imaging. Following this, the resulting images were manually segmented to obtain outlines of the differentiable merozoites and RBC membrane. For functional imaging, the detected pressures were corrected for r^2 amplitude decay using a correction algorithm.[112] This was not done for morphological images because the contrast was suitable for segmentation without this correction, and the raw pixel values do not reveal any morphological information. The pressures were assumed to be higher in the cytoplasm than in the parasites themselves as the cytoplasm contains the most Hb. For functional imaging, Hz amplitude was assumed to be 10 times that of the cytoplasm amplitude,[113] with little to no initial pressure in the parasites (corresponding to low absorber concentration).

Functional Imaging Parameters and Geometry

To simulate functional imaging, the simulation replicated conditions in which the Hz and Hb concentrations are not uniform throughout the cell, with Hz only present in the digestive vacuole of the parasites. nPAT RBC imaging at two different wavelengths was simulated, one at which Hb and Hz both absorb strongly and another at which only Hz absorbs strongly.

The reason for difference imaging is that Hb optical absorption is strong at 532 nm; however, Hz absorption can be more than an order of magnitude higher than Hb at this wavelength.[113–115]

Therefore, if Hz were evenly distributed throughout the RBC, it would be the only optical absorber that stands out as compared with the background and would render Hb concentration mapping impossible. Fortunately, Hz formation and storage occurs entirely inside the digestive vacuole of the cell.[116] Additionally, Hb absorption is around four orders of magnitude less than that of Hz at wavelengths of around 670 nm. Therefore, PA signals imaging at 670 nm would almost entirely originate from Hz. The drastic difference in Hb absorption at these two wavelengths (532 and 670 nm), and the strong absorption of Hz at both wavelengths, presents an opportunity for difference imaging. The simulations here have been performed accordingly, with one simulation featuring both Hz and Hb absorptions, and a second image featuring only Hz absorption. The difference between these two images reveals the Hb concentration distribution throughout the cell.

Results

Morphological Imaging

X-ray tomograms of E64 treated schizonts just prior to egress were used as the simulation geometry to determine the initial acoustic pressure, which was then allowed to propagate to a linear detector array with element size of 200 nm (corresponding to the diffraction limit of 532-nm light, representing the focused probe beam). For the sake of simplicity, detected A lines were converted to images by simply mapping the intensity of the detected waveforms back onto the image space. These images were in turn manually segmented to identify parasites within the cell. The maximum supported frequency of the grid was 46.7864 GHz, and the detectors were not given any restrictions on bandwidth to simulate the high bandwidth of the pump–probe detection. This contrasts with a PAM simulation, in which the detectors would have to be assigned some bandwidth of detection.

This high bandwidth is what allows nPAT to achieve higher resolutions suitable for cellular imaging. The output of the k-wave simulation (a series of pressure versus time plots) represents detected signals in nPAT at different positions of laser scanning.

A 2-D slice from a simulated nPAT image is shown in Figure 12b This figure shows that the merozoite images in nPAT have comparable resolution to those in x-ray microscopy. Merozoites (manually outlined in blue) are clearly visible within the RBC membrane (outlined in red). However, if this image was obtained by an nPAT imaging device, it would be an in-vivo image of the merozoites without necessitating fluorescent labeling. In addition, two of the vacuoles identified by Hale et al. are also visible.[106]

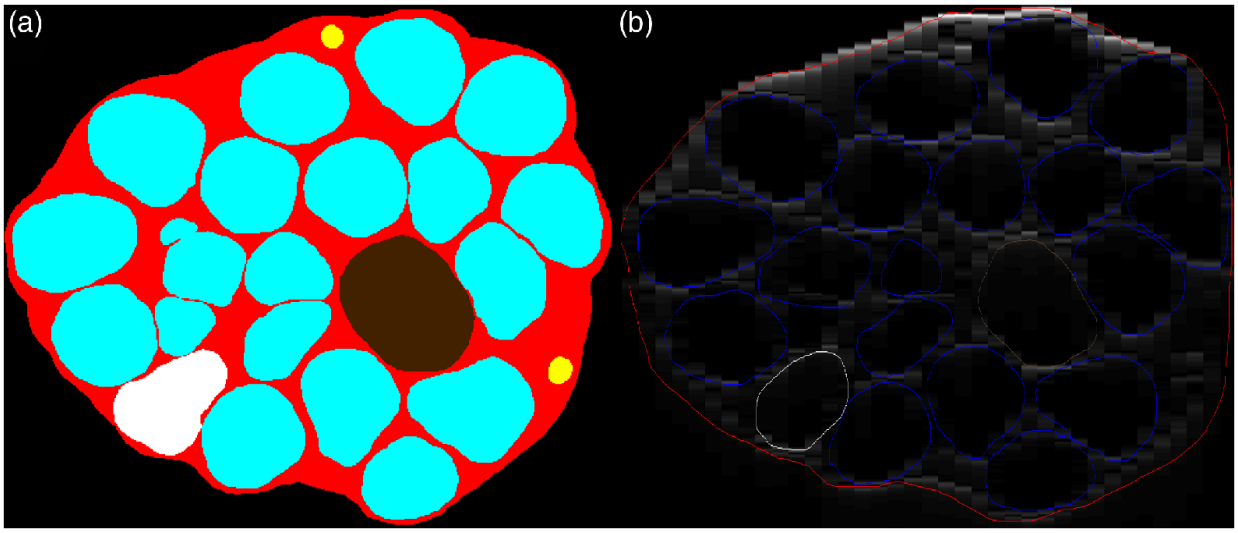

Figure 12: Simulation 2-D output (a) simulation geometry from segmented x-ray micrographs provided by Hale et al[106] and (b) nPAT simulated image of samples slice in (a); outlines of merozoites and RBC can be made, as well as the larger vacuoles. Manual segmentation was performed to the image in order to outline key features.[109]

This image was generated assuming Hb concentrations in the RBC according to the biological parameters. It has been shown that malaria cells digest up to 65% of the Hb in their host cell,[117] and so the absorption coefficient inside the merozoites was modeled as being ~30% smaller than that of the surrounding cytoplasm. Although the actual Hb may well be broken down and sent to the digestive vacuole for biocrystallization into Hz, the ultimate effect of this difference is that there is a much weaker photoacoustic signal from the malarial cells as opposed to the cytoplasm because that they have far less Hb.[118] This contrast is present regardless of where the Hb ends up as long as there is less Hb inside the merozoites than inside the cytoplasm. Hb that enters the merozoites is broken down via proteolysis, and the waste products are in turn transported to the digestive vacuole.[117,118] It is reasonable to expect that the Hb concentration inside merozoites will be substantially lower than that in the cytoplasm. nPAT can, therefore, differentiate between subcellular merozoites in malaria-infected RBCs and the cytoplasm of the RBC. As Hz is localized in the digestive vacuole (which can be removed via subtraction imaging at a different wavelength), the absorption of Hz was ignored for anatomical imaging simulations. However, it should be noted that in the experiment the suppression of this background will require multiwavelength laser imaging, taking advantage of the large difference in absorption of Hz and Hb at the wavelength of 700 nm and comparing with images from wavelengths at which Hb exhibits a peak. It can be seen that the stronger signals are near the "edge" of the merozoites. This is not to be confused with an edge effect; however, this is a consequence of the tight packaging of merozoites at this stage. The erythrocyte cytoplasm is visible entirely and all parts of it produce a signal. The appearance of signals originating from membranes alone is due to the high density of merozoites in the cell. As Hb concentration inside the merozoites is modeled to be smaller than that of the cytoplasm, the

absence of a signal is used to identify merozoites. Merozoites are tightly packed within the cell, these signals are only strong in the small areas between merozoites, leading to what appears to be an edge effect but is in fact simply Hb absorption.

Two-dimensional slice-by-slice imaging can enable 3-D imaging and rendering of biological phenomenon. In this way, nPAT can achieve 3-D imaging through repeated tomographic imaging of 2-D slices. These 2-D slices can be segmented and then a mesh can be formed from segmented features to render 3-D images. The E64 nPAT tomogram was put through this process to model a sample nPAT 3-D image. The resultant image (shown in Figure 13) was generated by meshing segmented merozoites, vacuoles, and the RBC membrane.

The shapes of the merozoites are apparent in high resolution. This image displays the 3-D imaging capabilities of nPAT to image malaria-infected RBCs. As nPAT is a noninvasive test, this imaging could theoretically be done during the live development of malaria without the need for E64 fixation to prevent egress, allowing for visualization of malarial development in living RBCs. The primary constraint of in vivo imaging will be in obtaining a high signal-to-noise ratio while simultaneously achieving fast raster scanning to allow for dynamic visualization. In this context, fast pump–probe scanning techniques such as asynchronous optical sampling can be combined with fast raster scanning techniques such as those used in photoacoustic remote sensing microscopy (PARS) to increase speeds and potentially enable dynamic imaging for small fields of views.

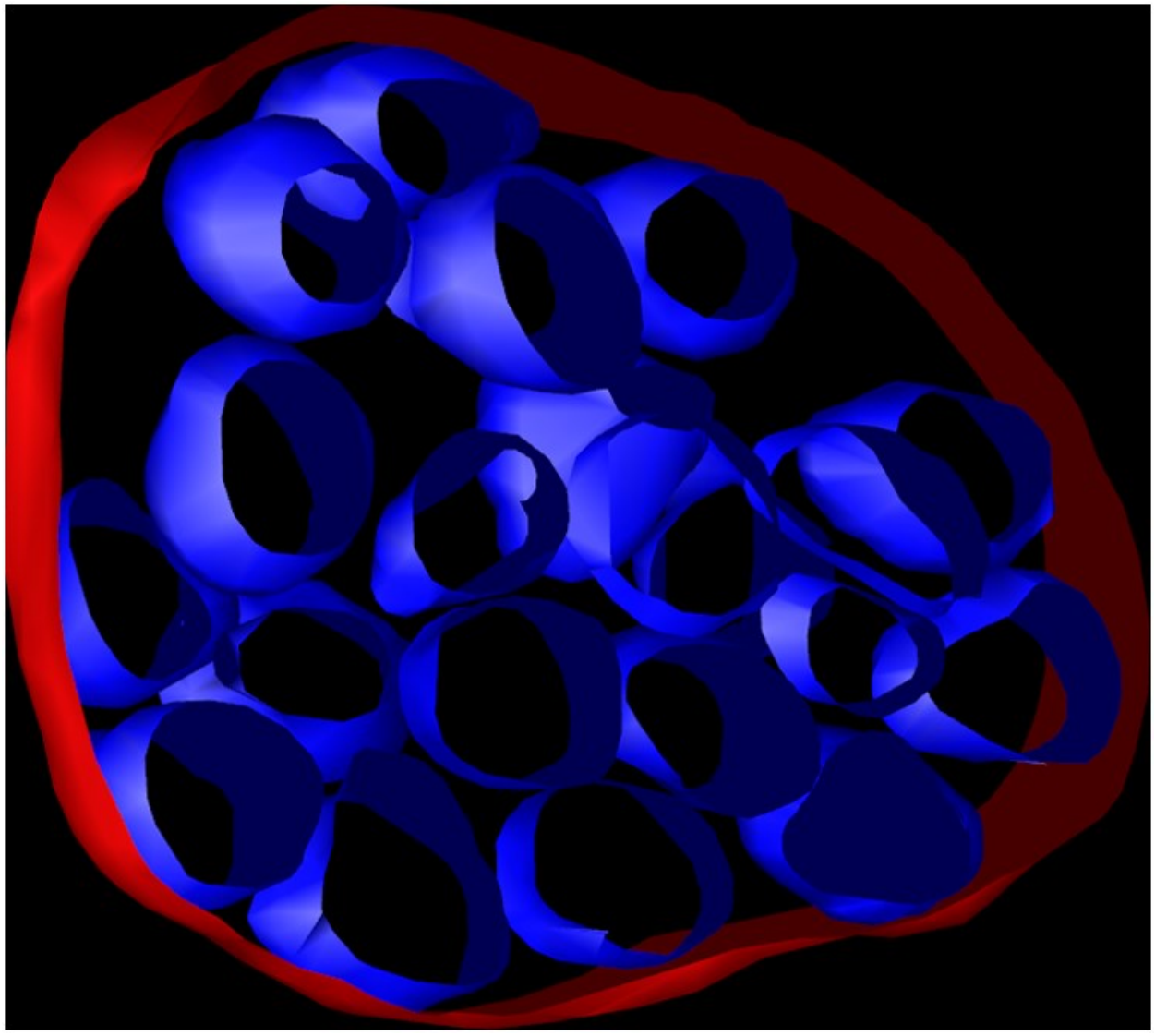

Figure 13: E64 simulated 3-D nPAT image after slice segmentation and meshing: merozoites (blue) can be easily distinguished. The RBC outline (red) is also visible. The 3-D tomogram shows structural features with nanometer resolution throughout the RBC.[109]

Different stages of malarial development can also be imaged with nPAT, allowing it to record, in vivo and without fluorescent labels, malarial development after cell infection. A C2 fixed cell was imaged with an x-ray microscope by Hale et al.[106] These tomograms, as in the E64 case, can serve

as inputs to a k-wave simulation of nPAT imaging. The 2-D sample geometry with segmentation is shown in Figure 14a, and the resulting simulated nPAT image of this sample is subsequently shown in Figure 14b. The rough morphology of the RBC and the PVM is both preserved and visible in nPAT.

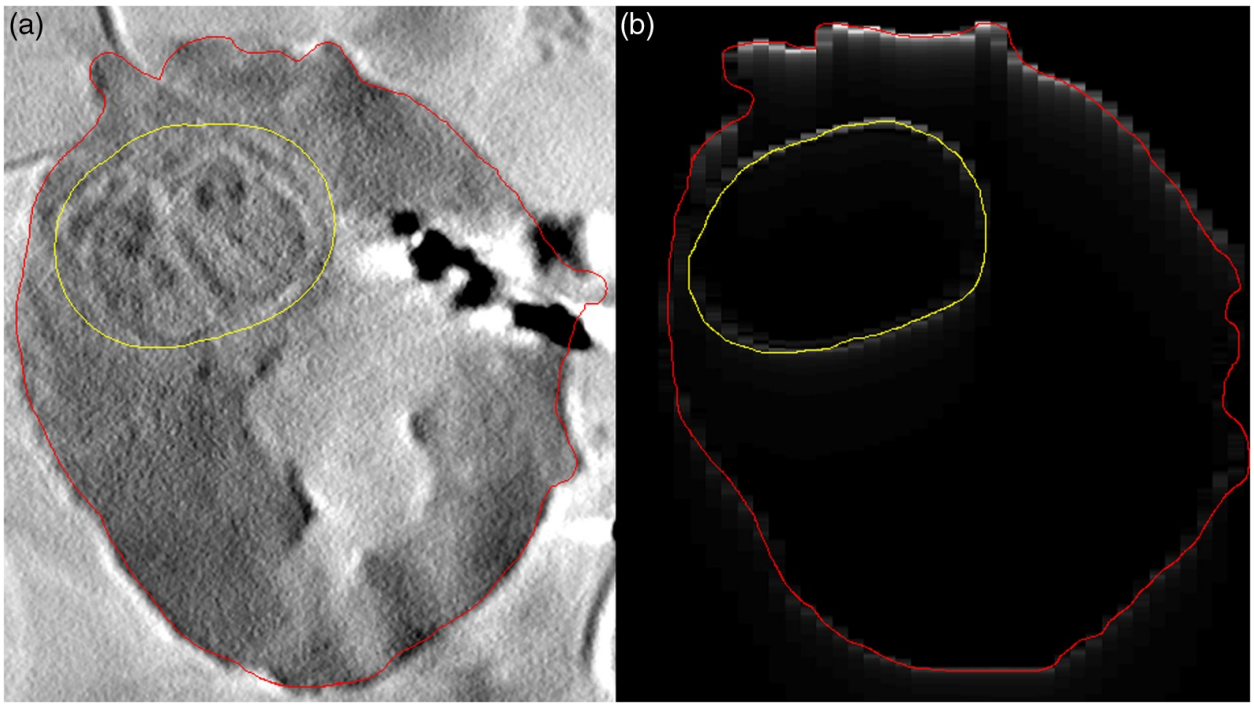

Figure 14: (a) Segmented slice from C2 treated RBC infected with malaria imaged with x-ray microscopy, (b) simulated and segmented nPAT image of (a); outlines of the PVM and RBC membrane are visible (yellow: PVM, red: RBC membrane).[109]

The resulting 3-D tomographic image is shown in Figure 15. The yellow parasitophorous vacuole is clearly visible. However, the packaged malarial parasites could not be consistently differentiated from the parasitophorous vacuole in all 2-D slices. Nevertheless, the shape of the vacuole can be assumed to roughly resemble the shape of the parasites themselves as demonstrated by Hale et

al.[106] This image demonstrates that nPAT is capable of imaging not just late stage but also early stage malarial development in vivo.

Figure 15: Three-dimensional image of C2 fixed schizont after slice segmentation and meshing, demonstrating nPAT's high-resolution imaging of early stage malarial development. Parasitophorous vacuole is shown in yellow with RBC membrane shown in red.[109]

Figure 16a shows the resulting image from functional imaging simulations at a wavelength where Hb and Hz absorb strongly. Due to the even stronger absorption of Hz, there is little contrast near the digestive vacuole from Hb, and the cell appears very dim compared with the strong signal coming from the digestive vacuole. Imaging at a wavelength where only Hz absorbs will essentially only produce an image of Hz concentration itself as shown in Figure 16b. To see the Hb image with the Hz interference removed, subtraction imaging can be done by taking the

difference between Figure 16 a and b, shown in Figure 16c. With the Hz signal subtracted, Figure 16c is a relative concentration map of Hb only, therefore demonstrating the functional information that can be obtained from nPAT.

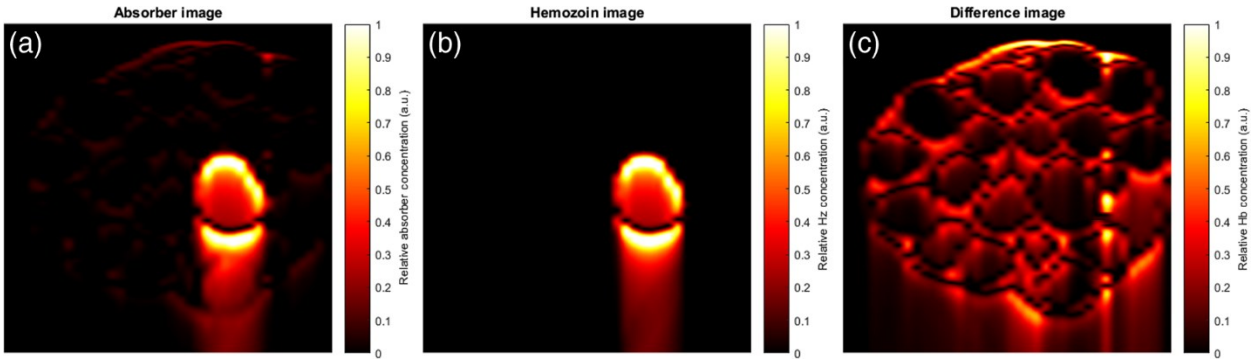

Figure 16: Simulated functional imaging via nPAT. (a) Full absorber image, including both Hb and Hz. (b) Hz image showing relative concentration map. (c) Difference image of subtracting (b) from (a), revealing relative Hb concentration in the cell.[109]

Discussion

The theoretical sensitivity and resolution of nPAT were derived. The sensitivity value of 292 NEN and 21 Pa NEP can be expected to be that of an ideal nPAT system. This would imply that a signal of typical amplitudes should be detectable. It has been shown in Chapter 2 that a 100 W, 7-ps pulse is capable of generating photoacoustic pressures on the order of 10^4Pa. This sensitivity value demonstrated that nPAT should be capable of detecting signals generated from RBCs for high-resolution imaging. The primary factor affecting the sensitivity is the distance from the probe focus. The sensitivity will decrease as distance from the sample increases. However, the distance between the probe and pump will typically be in the range of μm, which is substantially closer to

detection that is feasible with a transducer as in PAM. Therefore, nPAT is expected to still maintain low NEP at imaging depths of several microns.

The propagation of nPAT signals is dependent on two factors, one of which is the $\propto r^3$ amplitude decay of all 3-D acoustic waves. The amplitude of the wave must not fall below the system sensitivity at the time and location of detection. The second limitation is that of acoustic frequency attenuation. As an acoustic wave travels through a medium, higher frequencies are attenuated more as compared with lower frequencies in accordance with power–law attenuation. This places a limitation on the maximum detectable frequency of the pump–probe method since signals, as they propagate, will lose their high-frequency components that are crucial for higher resolution imaging. As a result, the actual resolution is itself a function of the imaging depth, with smaller imaging depths corresponding to higher resolutions (with an upper limit on resolution as derived earlier for entirely superficial imaging). nPAT is unique in this context from transducer-based photoacoustic imaging modalities since in nPAT, the detection beam is focused close to the point of optical generation. Therefore, imaging resolution does not depend on the acoustic time-of-flight distance from the source to the surface of the sample but rather the time-of-flight from the source to the probe beam focus. The imaging depth, therefore, depends on light penetration into the sample. So long as the probe beam light can reflect back from its focal point at a given depth, nPAT imaging is possible. The detection laser can be focused at a point 8 m away from the excitation point so that the acoustic signal needs only travel distance between the two laser foci.

The maximum achievable resolution was derived to be $\sim 10\text{nm}$ at a pulse duration of 7 ps. Narrower pulse widths will produce higher frequency signals, which, if detectable, can extend the

maximum achievable resolution of nPAT to smaller than this value (assuming an indefinitely small absorber). About 10 nm represents the superficial resolution of nPAT and is calculated assuming that the distance from generation to detection is very small so as to not heavily attenuate high frequencies within the signal. nPATs resolution also depends on the absorbers in question and their physical size, with a limit on resolution corresponding to the size of the absorber itself. The experimental resolution of nPAT will degrade at larger detection distances from the source due to frequency attenuation in the sample and thermal nonlinearities. Thermal nonlinearities can be negated so long as the rise in temperature is kept small, which was shown to be the case in Chapter 2. These simulations have accounted for frequency attenuation of the signals ($\alpha = 0.0022$, power–law attenuation with exponent of 2) and have shown that high-resolution imaging of RBCs is still possible for depths up to at least 8μm. Therefore, it is believed that the frequency attenuation of the acoustic signal will not result in a large enough degradation of the resolution to no longer be suitable for subcellular resolution imaging. However, precise estimates of the ranges of resolution and sensitivity will require more intensive simulation studies examining the precise full width at half maximum of a photoacoustic signal as it travels through a sample at various imaging depths and at various pulse widths. It also important to note that nPAT serves to improve the axial resolution, but the lateral resolution of nPAT remains diffraction limited. To achieve true 3-D super-resolution imaging, a future generation of nPAT could integrate concepts from structured illumination[15] to achieve lateral super-resolution, and integrate these principles with the axial super-resolution achieved by pump–probe imaging. Therefore, nPAT can serve as a key component in the realization of a truly 3-D super-resolution microscopy.

Previous studies have already demonstrated in experiment the feasibility of photoacoustic signal detection through the use of laser beams, leading to the development of methods such as PARS microscopy.[42,119] However, the detection bandwidth of PARS is ultimately dependent on the bandwidth of a detector photodiode, which is typically not in the range of several GHzs. This is a result of the fact that the probe beam in PARS is not pulsed but continuous. Using a pulsed probe and pump beam, as in picosecond ultrasonics[47] can increase the detection bandwidth in the range of hundreds of GHz, depending on the minimum possible delay increment between the pump and probe beams.

nPAT can theoretically image any molecules within biological samples that strongly absorb a particular wavelength of laser light at high contrast levels to the background. This is largely due to the high versatility of optical absorption spectra in biological samples. As the acoustic signal in nPAT is ultimately proportional to the absorption coefficient, nPAT allows for the visualization of a multitude of biological molecules on par with those previously imaged by photoacoustic imaging; this includes Hb,[120,121] lipids,[122], melanin.[8,123,124], and water.[125]

The contrast mechanism for an nPAT image is, as in photoacoustic imaging, optical absorption. In this way, nPAT can yield intrinsic optical absorption information in the case where a sample strongly absorbs the excitation laser wavelength. The excitation wavelength can in turn be adjusted to image using different intrinsic contrast agents and obtain a multitude of optical absorption maps for different wavelengths. In the context of imaging RBCs, an excitation wavelength of choice is 532 nm, as Hb has an absorption peak here. Different intrinsic contrast agents can be selected by

tuning the excitation laser to the absorption peak (as compared with other locally occurring absorbers) of the molecule of interest.

These simulations show the potential for nPAT to image cells at resolutions comparable with x-ray microscopes. However, unlike x-ray microscopy, an nPAT image would not expose the sample to damaging ionizing radiation. In addition, nPAT imaging of RBCs does not require any sample preparation. This is because the primary absorber in RBCs is Hb, which is already naturally occurring. As a result, Hb concentration mapping can be performed by nPAT without the need to prepare or otherwise alter the sample. These simulations also indicate that nPAT can image malarial cells at different stages of parasitic development. Simulations suggest that nPAT has the potential to achieve anatomical and functional in vivo imaging at resolutions comparable with x-ray microscopy without using exogenous contrast agents.

While currently under development, the results here demonstrate the potential of nPAT to impact biomedical imaging. It is possible that nPAT can eventually enable label-free 3-D imaging at high resolutions.

Nevertheless, further research is required to experimentally develop nPAT to achieve its first nanoscale images of real samples. Firstly, it needs to be established experimentally that laser-based detection of TA signals can indeed work for frequencies in the GHz regime. Additionally, it is important to establish that such waves can be generated by a picosecond laser at high enough amplitudes. In the following chapter, experimental verification of models predictions is presented, particularly regarding the high-frequency generation and detection capabilities of nPAT.

Chapter 4: GHz Photoacoustic Signal Detection by a Pump-Probe System

Overview

In previous chapters it was established that theory predicts a picosecond laser should be able to generate GHz photoacoustic signals in a sample. It was also established that such waves should be detectable using pump-probe laser based detection. In this chapter, a preliminary version of an nPAT imaging system is built and used to detect GHz signals produced by a picosecond laser. Photoacoustic imaging (PAI) has enabled the high-resolution imaging of biological samples without reliance on external contrast agents. However, conventional photoacoustic resolution in the axial direction is dependent on the maximum-detectable frequency of the ultrasound transducer, thereby limiting axial resolution to micrometers. In this chapter, GHz detection of a PA signal that can potentially enhance the achievable resolution in PAI is shown, previously limited by the detection bandwidth of ultrasound transducers. The experimental setup shows that GHz detection of the PA signals is achievable via pump-probe imaging setups, which can enhance the axial resolution of PAI by orders of magnitude. This validates one of the key theoretical predictions made in previous chapters regarding the potential of nPAT to image at nanoscale resolutions.

Introduction

Photoacoustic imaging (PAI) is a noninvasive hybrid imaging modality that can yield high-resolution images using endogenous contrast.[8] By coupling optical excitation and ultrasonic detection, PAI can image a wide variety of naturally occurring biomolecules, allowing for a set of

very versatile imaging applications, such as vasculature[61,121,126], DNA[16], lipids[122,127,128], and enzymes.[13,129] PAI therefore shows great promise in enabling multi-scale imaging from the same contrast mechanism, and could enable a wide variety of future biomedical discoveries.

As in clinical ultrasound, high frequency signals encode high resolution information, and the detection of high frequency signals is crucial in microscopic applications of PAI, such as photoacoustic microscopy (PAM).[8] The axial resolution of conventional PAM is limited by the maximum detectable frequency of the photoacoustic (PA) signal.[35,36,130] Higher-frequency photoacoustic signals encode high-resolution information about the sample. Whereas resolutions in the nanometer range require the detection of GHz ultrasound waves, typical ultrasonic transducers are restricted to bandwidths on the order of MHz.[39] Therefore, PAM has so far been unable to achieve nanometer axial resolutions as have become common in fluorescence super-resolution imaging modalities.

There have since been several ideas to improve the resolution of PAM. Zhang et al.[39] have used a high bandwidth transducer to obtain 7.6μm axial resolution, but this is not capable of achieving <200nm axial resolutions due to transducer bandwidth limitations. Danielli et al[13] have demonstrated a label free photoacoustic nanoscopy with 88nm lateral resolutions using nonlinear effects. However, the axial resolution again remains limited by ultrasound transducer bandwidth, therefore making axial super-resolution impossible. Shelton and Applegate[131] have developed an improvement over axial sectioning by combining pump probe spectroscopy with PAM, however the axial resolution of this technique remains limited by optical focusing, not achieving the detection of GHz signals nor nanoscale axial resolution.

Pump-probe detection methods are often used in picosecond ultrasonics in order to generate high frequency (GHz) waves that are produced by lasers.[46,47,101,132,133] However, picosecond ultrasonics uses the laser generated-acoustic waves themselves to interrogate the samples. Picosecond ultrasonics used in the context of imaging then ultimately reveals images of acoustic contrast mechanisms, unlike PAM which provides optical absorption contrast. The high bandwidth of pump probe detection methods can be combined with the optical signal origin in photoacoustic microscopy to extend the axial resolution in PAM into the nanometer regime while still providing absorption contrast.

This chapter demonstrates the detection of GHz photoacoustic signals via the use of a pump-probe laser system, which has the potential to improve the axial resolution of PAI to levels comparable to super-resolution microscopy. Pump-probe acoustic detection is used to overcome traditional bandwidth limitations of PAM. The constructed system also benefits from detecting signals very close to the generation source, thereby preventing excessive low-pass filtering of the acoustic signal by samples. The physical principle of the system for imaging is shown in Figure 17a, two absorbers (A1, A2) are excited by a focused and pulsed laser beam, each generating an acoustic wave (W1, W2). These high frequency waves then travel to the detector, D, at different times. In this way, if W1 and W2 are temporally separate, this method can theoretically achieve resolutions surpassing the optical diffraction limit in the axial direction.[109]

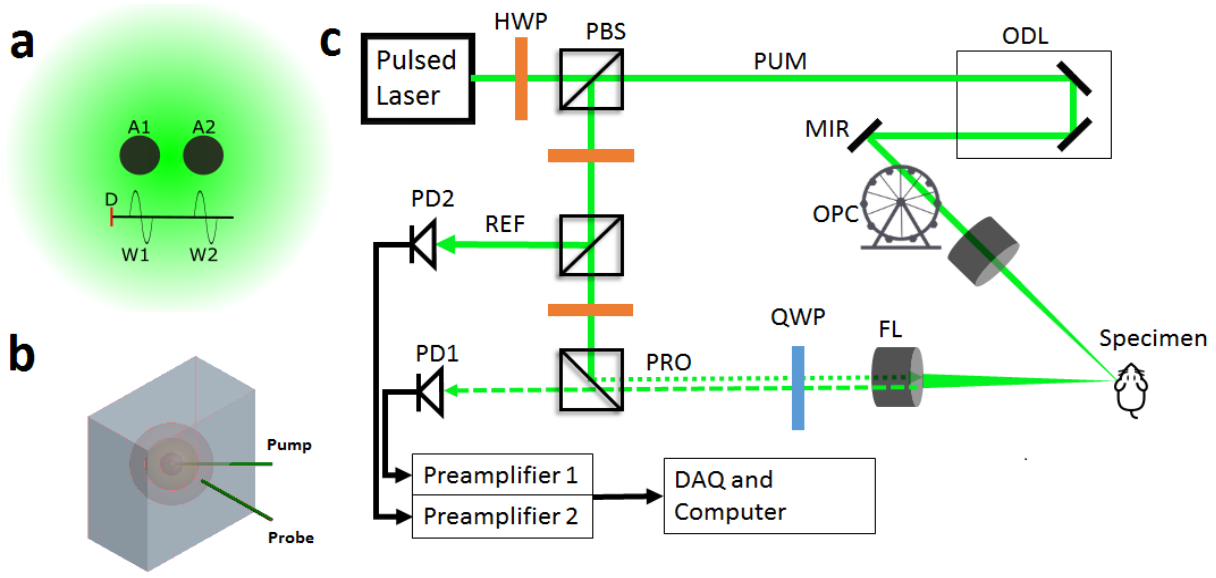

Figure 17: High Frequency PA signal detection imaging a) Physical principle of axial resolution improvement, two absorbers (A1, A2) are excited by a pulsed and focused laser, resulting in high frequency ultrasound emissions through the photoacoustic effect (W1,W2), emissions are detected at the detector (D). b)The pump arrives and generates a 3D, spherical acoustic wave c) Experimental set-up of the system, a laser beam is split into pump (PUM), probe (PRO), and reference (REF) beams through the use of half-wave plates (HWP) and polarization beam splitters (PBS), timing of pump and probe on the sample is controlled by an optical delay line (ODL). MIR: Mirror, OPC: Optical Chopper, FL: Focusing Lens, PD: Photodiode, QWP: Quarter-wave plate[11]

Methods

First, a pulsed laser beam (the pump) arrives at the sample (Figure 17b), generating an acoustic wave. The resulting acoustic pressure rise will affect the refractive index of the sample through

the optoacoustic effect. The refractive index change in the sample results in a corresponding change in the sample reflectance. This pressure-induced reflectance change on the sample can be quantified by a second laser beam (the probe), arriving at a precise delay time after the signal generation beam. Depending on the difference in arrival time between the pump and probe beam, heretofore referred to as the delay time, the plot of reflectance vs. delay time allows for the characterization of the high frequency acoustic signal.

Pump-probe detection for photoacoustic imaging uses laser induced ultrasound to ascertain information regarding optical information. This contrasts with picosecond ultrasonic applications of pump probe detection, in which picosecond laser induced acoustic waves themselves are used to interrogate samples.

Figure 17c shows a schematic set-up of the system, which uses pump-probe imaging to achieve high bandwidth detection of the acoustic signal. A pulsed laser of 532nm wavelength and 5ps pulse duration (Passat Ltd, COMPILER 532/266) is split, using half wave plates (Thorlabs WPH10ME-532-Ø1") and beam splitters (Thorlabs PBS121), into a pump, probe, and reference beam. Half-wave plates (Thorlabs WPH10ME-532-Ø1") and beam splitters (Thorlabs PBS121), into a pump, probe, and reference beam. Half-wave plates (Thorlabs WPH10ME-532-Ø1") are used prior to polarization beam splitters to allow for adjustment of the polarization of the laser beam. This therefore enables control of the energy ratio of the split beams. The pump is directed and focused by a focusing lens (Thorlabs AC254-150-A-ML) onto the sample through an optical delay line (Thorlabs ODL220) to generate the signal. The probe beam is directed onto the sample at a different angle through a quarter wave plate. The probe beam then reflects off the sample and back

through the quarter wave plate (Thorlabs WPQ10ME-532) towards a photodiode (Thorlabs PDA100a). The half-wave plate immediately following the laser source is used in conjunction with a polarization beam splitter such that 90% of the beam energy is directed towards the pump beam, with the remaining 10% being further attenuated prior to being evenly split between probe and reference beams. The quarter wave plate is set such that the pump polarization is perpendicular to the reflected probe polarization, and so only reflected probe light can go through the polarization beam splitter in front of the photodiode. The signal from the photodiode is amplified and filtered via a current preamplifier (Stanford Research Systems SR570). The signal then arrives for final processing and analysis to a data acquisition (DAQ) card (National Instruments PCI 6281) and computer. A reference laser beam is directed without any interaction with the sample towards a photodiode. The reference and probe beams are arranged to arrive at their respective photodiodes simultaneously.

A labelled photograph of this system is provided below in Figure 18, the beam arrives from the bottom left of the photo, first going through the attenuator (AT) before being split. By the first PBS, where it then proceeds as shown in Figure 17c

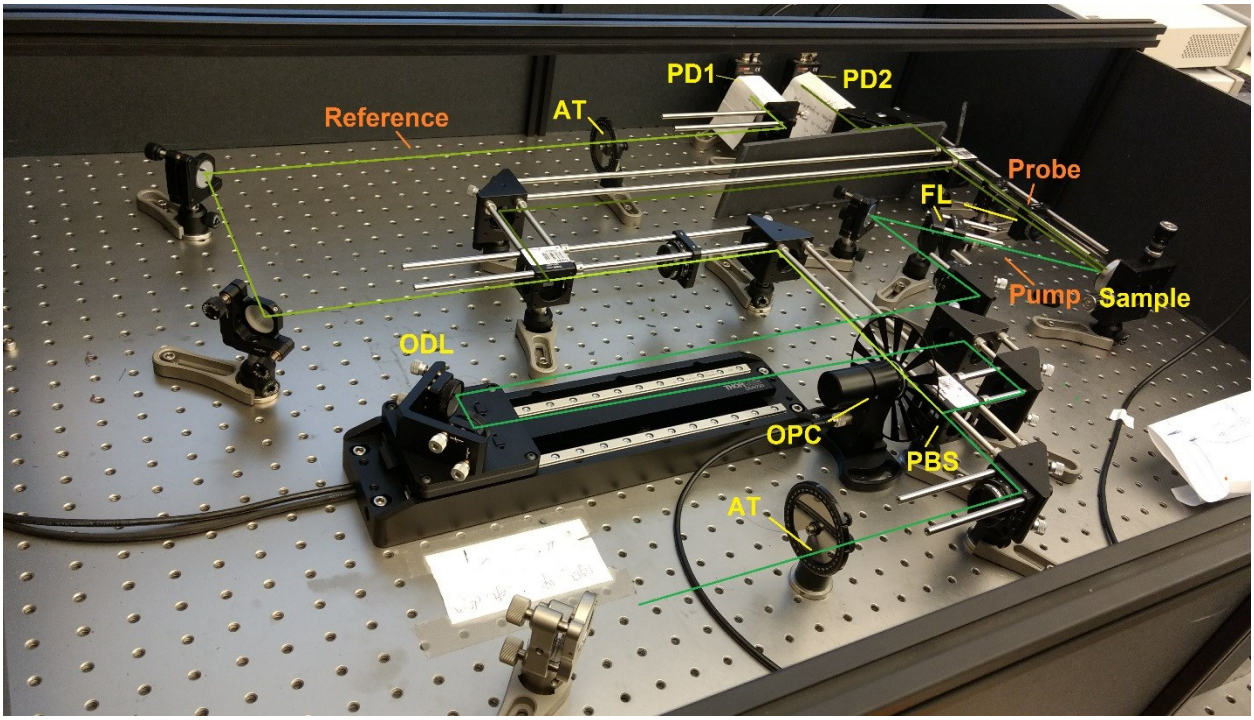

Figure 18: Photo of experimental set-up from Figure 17c. The beam path is shown by green colored lines, the shade of green changes every time the beam splits. AT: Attenuator, PBS: Polarization beam splitter, FL: Focusing Lenses, PD: Photodiode, OPC: Optical chopper

To correct for pulse-to-pulse laser intensity fluctuations, signal processing in this system plays an important role. As has been demonstrated by Werley et al.[134], the impact of pulse to pulse energy fluctuations can be largely corrected for to dramatically improve the signal to noise ratio (SNR) by analyzing the photodiode peak voltage with the pump beam present and pump absent to retrieve the signal modulation. To establish a system in which the pump beam was present on the sample at every other instance of the probe beam, an optical chopper (Figure 17c, Figure 19, and Figure 20) modulates the pump beam at half the repetition rate of the laser (200Hz). Therefore, a pump beam is present for only every other peak detected by each photodiode. The modulation of the

probe signal when the pump is on is compared to the probe signal when the pump is off. The quantity of interest is described by the expression

$$\frac{\Delta I}{I_0} = \frac{\left(\frac{PD1_a}{PD1_b}\right)}{\left(\frac{PD2_a}{PD2_b}\right)} \tag{25}$$

With PD1 and PD2 corresponding to the peak voltage from a pulse from PD1 and PD2 from Figure 17, respectively. The subscript *a* corresponds to the pump being present, and *b* corresponds to the pump being absent. The signals being described are illustrated in Figure 19, which shows the corresponding values in the form of voltage vs time plots on both probe and pump photodiodes. $\frac{\Delta I}{I_0}$ can only be computed, then, with at least a pair of pulses from the laser, one pulse with the pump present and the other with the pump absent. Several such pulse pairs can be computed and the corresponding $\frac{\Delta I}{I_0}$ can be averaged to further improve SNR. In our experiment, 50 pulse pairs were collected at each delay line location, and numerous scans of the delay line were also averaged to further maximize the SNR. The 50 pulse pairs collected corresponds to 100 data points per location collected by the DAQ card. The delay line scanned a total distance of 20mm, corresponding to a delay distance of 40mm. A total of 2103 delay locations were sampled per scan corresponding to a step size of ~0.0095mm. The primary rate-limiting step in the acquisition was the physical scanning of the delay-line itself, as the delay-line would need to move and stop in between every data set.[40]

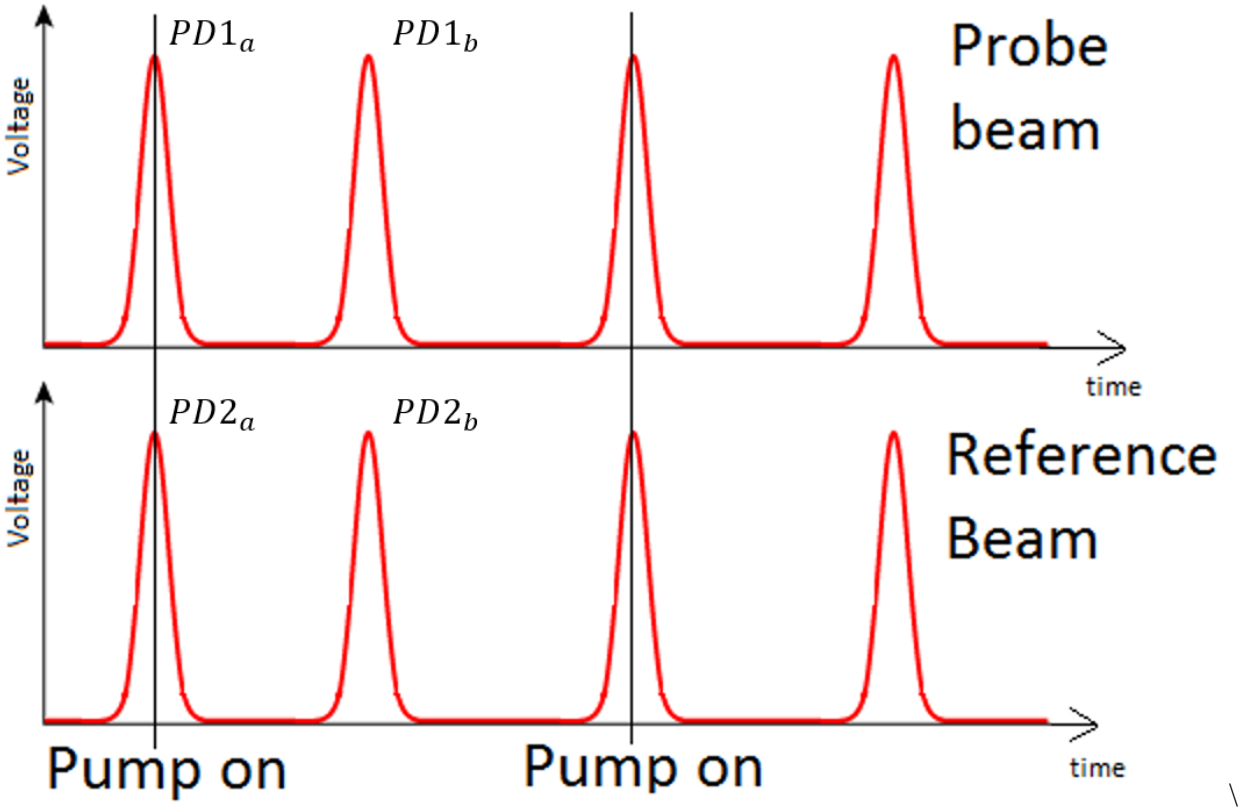

Figure 19: Principle of detection correcting for laser intensity fluctuations. Voltage vs time plots are collected for PD1 (top) and PD2 (bottom), the pump is present at every other pulse pair. Peak amplitudes from the two time traces can be used in conjunction with equation 25 to yield the value for $\Delta I/I_0$ as a function of the time delay.[11]

Due to the weak nature of the signal, careful communication between the various electronics is necessary to maximize the SNR. A schematic of all the electronic components used is shown in Figure 20. A total of four signals are collected by the DAQ card. A function generator triggers the laser controller via a TTL signal, triggering laser pulses at a repetition rate of 400Hz. The laser controller in turn sends a TTL signal corresponding to the pulse firing time to a delay generator. This additional routing of the function generator trigger through the laser controller was performed

to correct for laser jitter between pulses. The TTL signal from the laser controller has the same jitter as the firing of the laser pulses, and is used to trigger the chopper controller and to set the sample clock of the DAQ card to only collect pulses at voltage peaks.

To minimize the memory requirements of the DAQ card, the sample clock of the DAQ card is carefully timed with the use of a digital delay generator (Stanford Research Systems DG535) to correspond to the peak of the voltage signals from the two photodiodes. The delay generator was used to make it so that the sample clock TTL signal arrived at precisely the same time as the peak voltage of the photodiodes. As a result, the DAQ card only collects a single data point per voltage pulse, corresponding to the peak of voltage. In order to determine which peaks corresponded to pump present/absent situations, the chopper controller of the optical chopper acted to trigger the signal acquisition, such that every first pulse in a series collected to a pump present.

The maximum sampling rate of the DAQ card is limited to 625kHz. However, the pulse duration of a single pulse on the photodiode is on the order of nanoseconds. To lengthen the pulses to be large compared to the DAQ card sampling rate, we employed two current preamplifiers to enable amplification and low pass filtering of the photodiode signals. These current preamplifiers broadened the pulse duration so as to be on the order of ms, much larger than the sampling rate of the card.[134]

It should be noted that the sampling rate of the DAQ card is unrelated to the sampling rate of the detected acoustic waves, which are themselves dependent on the minimal possible movement of the optical delay line. The DAQ card sampling rate affects the system's ability to detect laser

pulses only, which fire at a rate of 400Hz. However the photoacoustic signal can be sampled at substantially higher frequencies due to the high detection bandwidth of the pump probe method.

For preliminary experiments, a 10μm thick strip of steel was used as a sample. This sample allowed for easy laser alignment and focusing while simultaneously producing a strong enough signal to configure the system. Thermal damage from the laser was also not a concern as the steel sample is quite difficult to burn as compared to actual biological samples. Nevertheless, the goal remains the use of the pump-probe laser system on biological samples.

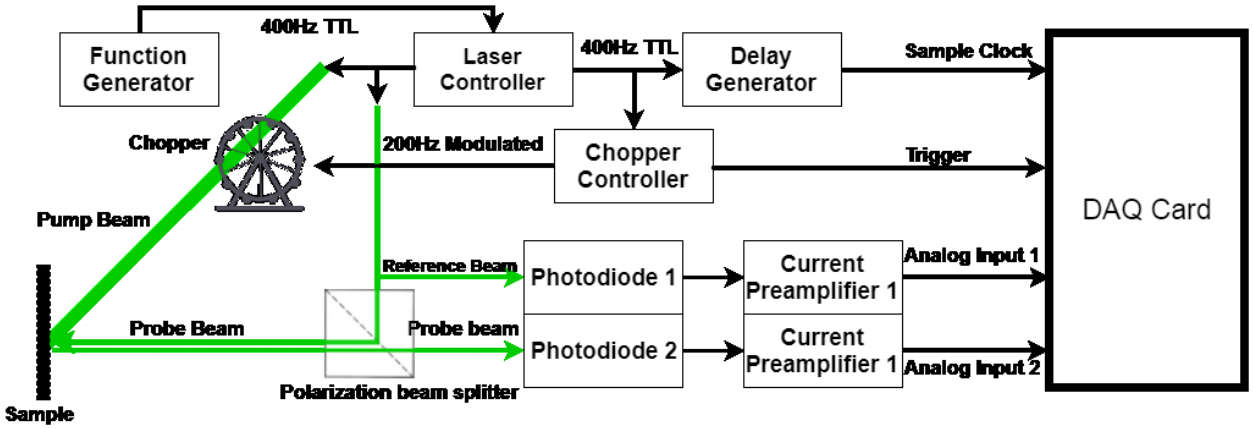

Figure 20: Signal Processing pathways, all signals make their way into different inputs of the DAQ card for processing.[11]

Results

The resulting modulations as a function of the delay time are shown in Figure 21. Figure 21a,b,c, show sample waveforms on three different days. The waveforms varied from day to day and scan to scan, due to imperfections in precise laser alignment, vibrational differences in the optical delay

line, temperature of the room, ambient light affected by weather, and pulse to pulse instability in the laser itself. The high pulse to pulse instability of the laser required averaging over multiple A-lines in order to obtain repeatable measurements. The noise level of the system could be accounted for by repeated averaging. The averaging of 12 collected waveforms shows a clearer signal with improved signal to noise ratio (Figure 21d). As the acoustic wave arrives at the sample surface, different delay times correspond to different distances travelled by the wave, and therefore yield depth information corresponding to $v_s t$ where t is the time of arrival and v_s is the speed of sound in the medium. Therefore, the modulation, $\Delta I/I_0$ yields depth information at different delay times. The optical delay line has precise time delay information and the path of both laser beams is measured, therefore controllable delay between the pump and probe is possible. Figure 4d shows the averaged signal of 12 scans taken over the course of three different days. The horizontal axis is converted into a depth inside the sample through the formula $\text{Distance} = v_s t$, where t is the delay time between the two beams, to show depth in place of time. A strong averaged signal can be seen after averaging of all signals.

To confirm that this signal was due to the influence of the laser, the same experiment was performed with the pump beam of the laser blocked. Two example waveforms from such experiments are shown in Figure 4e. It can be seen that the signal visualized in Figure 21a,b,c,d is entirely absent from waveforms collected without the laser present. This was the case for all tests conducted with the pump beam blocked. Additionally, it was ensured that the probe beam intensity was as low as possible incident onto the sample, measurements with PDA100a photodiodes on the sample were easily saturated by the pump beam but not close to saturated by the probe beam (signal

was on the order of ~mV). Figure 21d shows the averaged signal of 12 scans taken over the course of three different days. The horizontal axis is converted to a depth, d, inside the sample through the formula $d = v_s t$, where t is the delay time between the two beams, to show depth in place of time. A strong averaged signal can be seen. Figure 21f shows the Fast Fourier Transform (FFT) of the averaged signal from d, using time units as opposed to distance. The FFT shows significant contributions peaks at 0.7, 2.1, 3.67GHz, with a significant part of the signal spectrum in the range of 0-5GHz. This signal therefore can be used to high resolution imaging when the laser focus is raster-scanned throughout the sample. It is believed the reason for these peaks is because the fundamental frequency of the sample is ~0.7GHz, and we are seeing the 3rd and 5th harmonics of this. This signal is theoretically suitable of high-resolution depth imaging due to its high frequency nature and photoacoustic origin. The Fourier spectrum of the signal is influenced by several factors, primarily the pulse width of the excitation laser and the thickness of the sample. Sample thickness and pulse width are chosen such that the generation of a high frequency signal in the GHz range could be assured. The short pulse width of the laser is a crucial feature in the generation of GHz signals. The detection bandwidth of the pump-probe technique is much higher than the generation bandwidth of our system, therefore it is predicted that at shorter laser pulse widths, even higher frequency signals can be detected using an otherwise identical set-up.

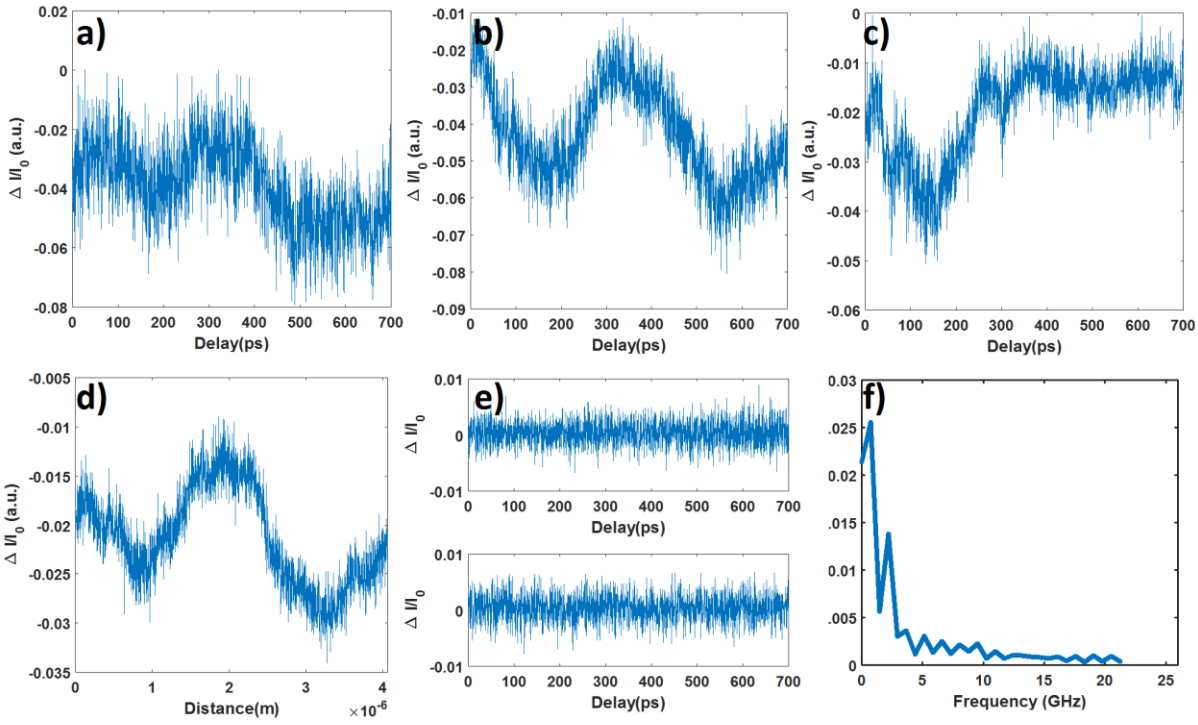

Figure 21: a,b,c, $\Delta I/I_0$ vs delay time sample waveforms collected from three different days, d) average $\Delta I/I_0$ of 12 such waveforms as a function of depth within the sample, corresponding to delay time. e) Noise waveforms, taken without the presence of a pump.[11]

The total scan time for each scan was on the order of ~1hour. However, employing faster axial scanning modalities could greatly reduce the required scan time. For example, Asynchronous Optical Sampling of ultrafast lasers can allow for scanning several orders of magnitude faster, at rates of several delay line scans per second. Asynchronous optical sampling can be combined with higher repetition rate of the laser can be employed to further increase scanning speed. As these techniques do not rely on a physical delay line for scanning, the scan speed can be improved to as high as tens of kHz 24. Extension of pump probe detection to biological samples requires a fast scanning speed in addition to the prevention of thermal damage from the laser. In previous

simulation experiments, we have demonstrated that a laser of ~200W fluence operating at our repetition rate would yield temperature rises on the order of mK while still generating strong and detectable photoacoustic signals from biological samples.25 So long as the duration between pulses is greater than the thermal relaxation time (shown to be ~10-8s by our previous studies), temperature damage to the sample should not be an issue.

Conclusion

The lateral resolution of such a system used for imaging is currently limited by optical focusing, and therefore is diffraction limited. However, techniques such as structured illumination[15,135–137] have been able to achieve super-resolution imaging by taking advantage of interference of diffraction orders and illumination at various controlled angles. Since PAM contrast agents are often endogenous, structural illumination could be combined with pump-probe axial scanning to enable endogenous 3D super-resolution imaging via a combination of structured illumination PAM and the detection of GHz waves.

Whereas previous studies have examined laser-based photoacoustic remote sensing[119], these techniques have so far had detection bandwidths limited to the response of a photodiode. Using a pulsed pump and probe instead, as is often done in picosecond ultrasonics[47], offers a much higher detection bandwidth and therefore enables an improvement in achievable axial resolution. The deployed method can therefore be employed to enhance the axial resolution of PAM substantially. Theoretical analysis of the resolution has shown in previous studies that the maximum achievable resolution can be as high as ~9nm, additionally the sensitivity of this method shows improvement

over that of conventional PAM according to calculations of the noise equivalent number of molecules [109].

One of the largest challenges in moving to biomedical imaging is the large image acquisition time (currently at ~1 hour per A-line scan). This is primarily because the delay line scan corresponds to a physical movement in the delay line, which needs to start and stop in between data collection. A large imaging time is suitable for proof-of-concept imaging of static samples, however not very practical for widespread use. Rapid scanning of the laser beam in x, y, and z directions much be achieved. Techniques to drastically reduce axial scan time, such as Asynchronous Optical Sampling, must be integrated into the laser system to enable fast imaging. However, these techniques must also be coupled with rapid lateral scanning of the sample, as has been done in photoacoustic remote sensing set-ups.[42,119] The imaging depth of this system is limited by optical penetration, of both the pump and probe beam. However, as the pump and probe beam can be focused very close to each other, there is very little attenuation of the acoustic signal between the point of detection and generation. The total imaging depth will likely be lower than that of conventional PA microscopy since the probe light must enter and exit the sample, however, due to the close proximity of the pump and probe beam, the sensitivity of this method will be higher than most implementations of conventional PAM [109]. As the penetration of green light into the epidermis can be as high as 2mm, GHz detection via pump-probe methods can be applied towards *in-vivo* imaging of superficial features

A detectable photoacoustic signal in the GHz range from photoacoustic modulation of a probe beam has been demonstrated. It is believed that pump-probe methods employed for detection of

photoacoustic signals can enhance the axial resolution considerably as compared to conventional PAM. The detection of GHz photoacoustic signals combined with structured illumination also has great potential in future studies to enable 3D imaging at resolutions of <200nm, thereby achieving 3D super-resolution.

Future Research in nPAT

There remain some theoretical open questions that future modeling can build on with regard to nPAT. Firstly, the imaging dept vs resolution tradeoff must be more accurately modelled in order to provide estimates for the utility of nPAT. While in Chapter 3 simulations have shown that at 8μm imaging depth, nanoscale resolution should still be achievable, it remains an open question what the exact relationship is between the resolution-imaging depth tradeoffs of nPAT. Future models to address this problem must incorporate signal amplitude decay with propagation distance as well as low-pass filtering that occurs in tissue. The final amplitude of signals arriving at the detector must then be compared to the typical noise levels that can be expected at the detectors in order to determine the maximum achievable resolution for a given distance between the pump ad probe beams.

Whereas the next step in the development of nPAT is the experimental realization of a true nPAT image, the main requirement for such an accomplishment is a laser much more stable than the one used in this study. Pulse to pulse intensity variation has been a major source of noise in the current experimentally developed nPAT prototype. This is primarily because of built-in parameters of the currently available laser. In the future, a more stable pulsed laser will be necessary with far smaller

pulse-to-pulse intensity variation, such a laser can drastically reduce the noise in the signal and therefore substantially reduce the number of averages required for sufficient SNR.

Lastly, there remains a crucial constraint on the time taken for a single axial scan using an optical delay line. Whereas the current scanning time per A-line acquisition outlined in this chapter can be several hours, this is an unacceptably slow rate of A-line acquisition for imaging in 3D or 2D, especially not for in vivo imaging where some elements within the sample can be dynamic. Solutions to this problem fortunately already exist, such as a laser system that is capable of asynchronous optical sampling (ASOPS)[102], which can easily perform thousands of A-line scans per second. Despite showing promise, there has not yet been a fully functional implementation of nPAT that could verify all the other predictions made from Chapters 1 and 2. This is one of the most pressing and important milestones in this research.

In this chapter, modelling predictions about bandwidth expectations were confirmed, thereby confirming that laser induced acoustic waves can generate GHz frequency signals. Now that this has been done, there remains an interesting question about the potential of other forms of radiation to generate detectable ultrasound. Especially as this would drastically expand the number of contexts in which the model could be deployed for imaging. Whereas nPAT is an imaging modality with applications in the nanoscale, the model is yet untested on length scales of entire millimeters, as is typical in conventional clinical medical imaging modalities. The next chapter deploys the developed model to millimeter length scales and explores its performance, and therefore its generalizability. In this way, a multi-scale thermoacoustic model can be confirmed.

Chapter 5: 3D Thermoacoustic Proton Beam Dose Mapping Through a Planar Ultrasound Array at a Millimeter length scale

Overview

In previous chapters, a model was developed for the generation of TA signals at nanoscale resolutions with picosecond laser pulses well approximated as delta function. The model was tested in the context of signal generation bandwidth and made several predictions with regard to imaging parameters. In this chapter, the model is extended to millimeter length scales. This chapter seeks to answer the question of whether TAI can be deployed in the context of proton therapy, and to see the quality of images that can be generated by a proton-induced acoustic signal. Proton beams can deliver a highly targeted radiation dose to a narrow volume defined by their Bragg peaks. However, the localization of the Bragg peak in the clinic has not yet been achieved due to large range uncertainties in delivery, even though this is crucial information to ensuring accurate dose delivery. Fortunately, a pulsed proton beam generates a thermoacoustic emission proportional to the absorbed proton energy, thereby encoding dosimetric information in a detectable ultrasound wave. In this chapter it is show through simulation that such protoacoustic emissions can be used to obtain high-resolution dose maps in 3 dimensions. Additionally, our simulation workflow models the acoustic dependence of emissions on pulse widths directly, and can be extended to analyze the potential of thermoacoustic imaging in a wide variety of contexts. This work demonstrates that the previously developed models used to predict nPAT imaging characteristics is generalizable to macroscopic thermoacoustic imaging as well.

Introduction

Proton radiotherapy is of increasing importance and prominence in radiation oncology. This is because proton beams can deliver a targeted dose in a narrow radiation volume defined by the Bragg peak of the proton beam. This narrow delivery of the dose allows for maximum dose delivery to the tumor region while minimizing dose delivery in surrounding healthy tissues. In contrast to x-ray based radiation therapy, the dose delivered to tissue from a proton beam is not highest at the surface, but instead inside the tissue at an adjustable, particle energy dependent depth.[138] Despite its promise, there remain some significant obstacles towards accurate proton radiation therapy

Bragg peak localization

In current proton therapy clinical procedure, Bragg peak localization is performed using Monte Carlo simulations using a scouting CT, and then attempting to position the patient in a similar position to that in the simulations. However, the steep dose gradient of the proton Bragg peak can rarely be used in practice to irradiate the tumor while sparing healthy tissues, because there is substantial uncertainty about the proton beam range, therefore introducing concern of severely overdosing healthy tissues. The range uncertainty of proton beams has several sources, such as the non-uniqueness and inaccurate nature of CT units to proton stopping powers, CT imaging artefacts, and changes in the patient during treatment caused by mispositioning, breathing, etc. Therefore, it remains an important clinical objective to achieve accurate proton range verification, ideally done through imaging and cross-correlation with known treatment plans.

Fortunately, pulsed proton beams generate detectable acoustic emissions of proportional amplitude to the deposited dose. This protoacoustic phenomenon presents a unique opportunity for range verification as well as dose imaging, as the Bragg peak itself is a high dose area and therefore a strong protoacoustic emitter. Therefore, with the simple addition of an ultrasound transducer array with appropriate frequency response, real-time proton dosimetry is possible in vivo.

This chapter presents simulations that demonstrate the potential of protoacoustic range verification and dose mapping in 3D during proton therapy. Our simulation workflow can also be easily optimized in order to conduct simulation studies of protoacoustics in the clinic, as all parameters are closely matched to clinical realities. It is shown show that protoacoustic dose mapping is possible using a planar ultrasound array with matching dimensions to a clinically realistic situation.

Theory of the Protoacoustic effect

The protoacoustic effect is ultimately a thermoacoustic phenomenon, wherein incident pulsed proton radiation rapidly deposited energy inside the target tissue. This rapid deposition of energy results in a localized temperature gradient and subsequent thermoelastic expansion within the sample. As the target tissue relaxes, an acoustic wave in the ultrasound regime is emitted, and propagates through the sample in three dimensions. A transducer array can then easily be placed near the source on the surface of the tissue in order to image the proton energy deposition in the sample. In this section some of the theory from Chapter 1 will be reviewed in the context of modelling pulsed protoacoustic signals towards the developing of a macroscale model of proaocoustic imaging.

The governing wave equation of the induced protoacoustic signal is as follows

$$\left(\nabla^2 - \frac{1}{v_s^2}\frac{\partial^2}{\partial t^2}\right)p(\boldsymbol{r},t) = -\frac{\beta}{\kappa v_s^2}\frac{\partial T(\boldsymbol{r},t)}{\partial t^2} \quad (26)$$

Where v_s is the speed of sound, p is the protoacoustic pressure, $\boldsymbol{r}$ is the position vector, t is time, β is the thermal coefficient of volume expansion, κ is the isothermal compressibility, and T is the temperature.[33] This equation is commonly solved for a delta function excitation with a Green's function approach.[33,34,139] Extention of the solution to a pulse of finite duration requires the convolution of the delta-function pulse solution with the pulse shape itself. Therefore, given the solution to an infinitely narrow pulse, p_δ the solution of the finitely large pulse is given as

$$p(\boldsymbol{r},t) = \int_{-\infty}^{+\infty} dt' p_\delta(\boldsymbol{r}, t-t')S(t') \quad (27)$$

where $S(t)$ is the temporal pulse profile.[34] Pulsed proton sources tend to have pulses on the order of μs in duration, which is typically on the order of how long utrasound signals take to travel from the source to the transducer. Therefore, delta function excitation assumptions are typically not valid for proton pulses in the range of 10s of μs.

Materials and Methods

Monte Carlo Simulations

A 5 step simulation workflow is designed and deployed in order to achieve realistic protoacoustic simulations in line with clinical parameters (Figure 22). The first step is to conduct a scouting CT of the sample in question. For convenience, we have done with a 30cmx30x30cm solid water

phantom. The CT is matched with standard human body digital phantom, featuring a prostate, rectum, and bladder relative positions.

Monte Carlo (MC) simulations were then run on the planning CT in order to estimate the proton dose deposition in the sample corresponding to the location of the prostate. In order for the MC simulations to run quickly, it was necessary to create a prostate phantom corresponding to a physical region that would fit within the 30cmx30x30cm solid water phantom with higher grid resolution than the scouting CT. In this way, the MC simulation could ensure maximal accuracy due to the higher grid resolution but still proceed smoothly due to the MC simulation size being smaller than the whole CT scouting phantom.

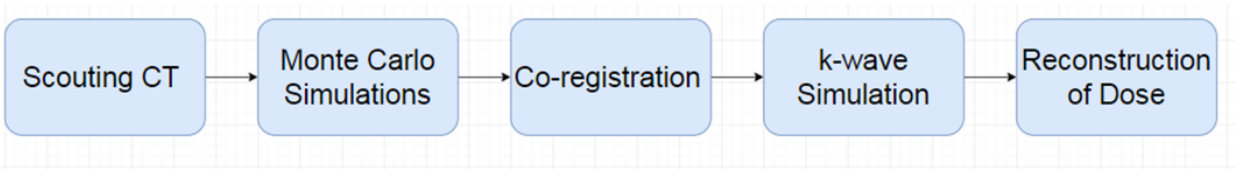

Figure 22: Simulation Workflow for Protoacoustic Imaging

Co-registration

The output of the MC simulation was overlaid with the solid water phantom CT via feature based co-registration in 3D slicer. The result of the co-registration is shown in Figure 23. A 3D digital phantom of organs was overlaid on both the prostate dose output of MC simulations and the 3D solid water phantom. The two images were then co-registered and made the same size via the use of this common prostate digital phantom. As the prostate is the same size, this can be used as a guide with which to re-size the MC simulation to the size of the 3D solid water phantom.

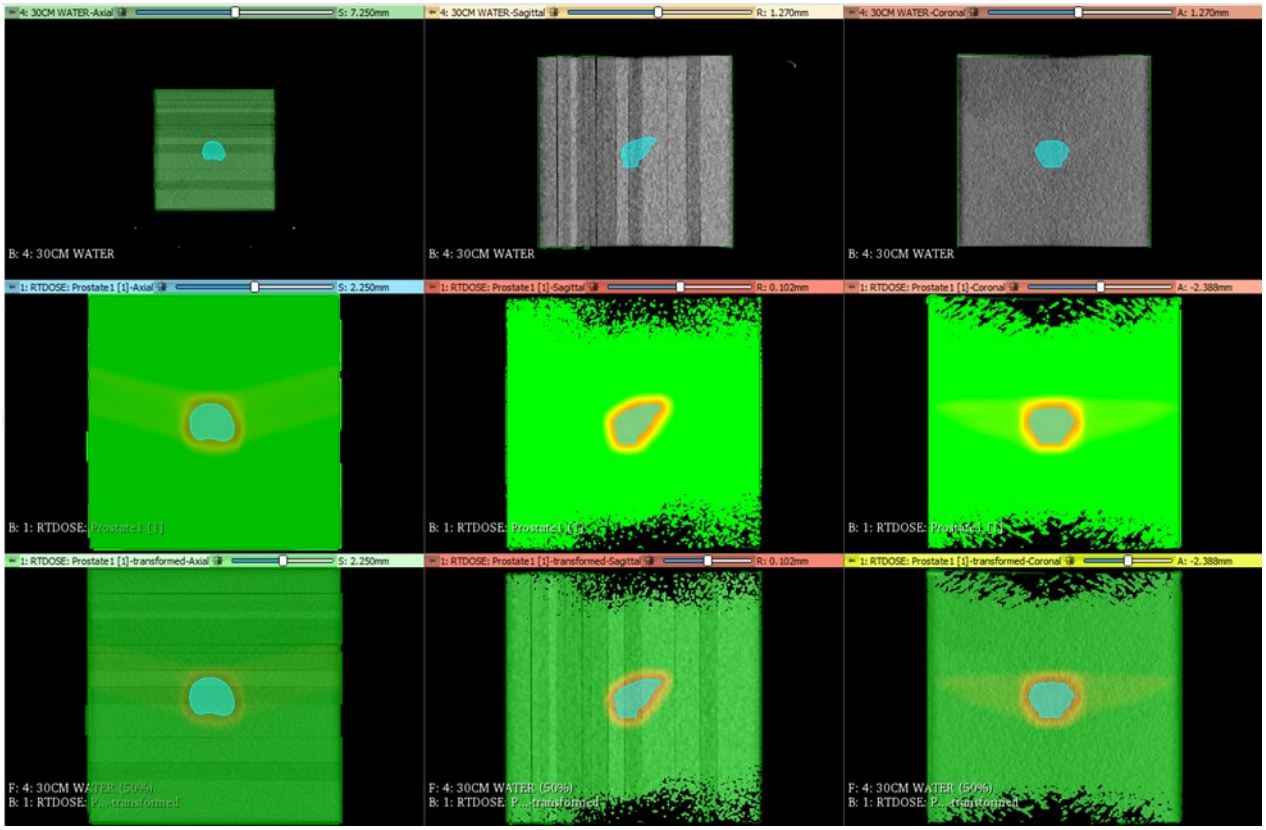

Figure 23: Co-Registration of CT image with MC dose plan. Top row: Phantom CT overlaid with digital prostate phantom (blue), Middle row: Proton Dose overlaid with digital prostate phantom (blue), Bottom row: Co-registered image with Phantom CT and prostate dose using feature mapping of the digital prostate phantom

K-wave Forward Simulation

Following the MC simulations of the proton dose, the dose is imported into MATLAB using the function dicomread. Here, the 3D dose can be used as a 3D initial condition to equation 26 using the k-wave MATLAB toolbox [110,140]. As the dose is linearly proportional to the protoacoustic initial pressure, this linearity be used to generate relative protoacoustic pressure maps in

MATLAB. This simulation is modelling a delta function pulse in order to obtain an estimate of p_δ. After initialization, the pressure is then allowed to propagate throughout the sample using a pseudospectral solution method. For speed, the code is run using the C++ version of k-wave as opposed to running the simulations in MATLAB.

A sensor array matching the dimensions of a parallel receiving transducer element is also added to the simulation in order to simulate signal reception by an ultrasound transducer array. The sensor array consists of a 5x5cm planar array with 16 elements evenly spaced in each direction. These dimensions were chosen to match a planar array that we possess and are actively using in experiments. For brevity, let $D_{\delta i}$ be the pressure vs. time signal of the ith element in the delta function simulation (with I ranging from 1 to 256) for the remainder of this thesis.

Convolution with Gaussian Pulse

As the pulse duration is an important factor to account for in image quality, it is not sufficient to only model p_δ, the pulse width must also be taken into account via suitable adjustments to all $D_{\delta i}$ signals. To this end, perform the numerical convolution of a Gaussian pulse of variable pulse width with detected acoustic pressure for all 256 sensor elements was performed. First, re-sampling/interpolating $D_{\delta i}$ is done to match the length of the discretized $S(t)$. The resulting waveform, $D_{\theta i}$, represents the pressure that the sensor would detect in the case that the initial pressure was deposited over a finite time interval corresponding to a Gaussian pulse with width θ. Then,

$$D_{\theta i}(k) = \sum_j D_{\delta i}(j) S(k - j + 1) \tag{28}$$

where all functions are discretized. This can be turned into a function of time, $D(t)$ by mapping the timestep vector to the elements within $D_{\theta i}(k)$.

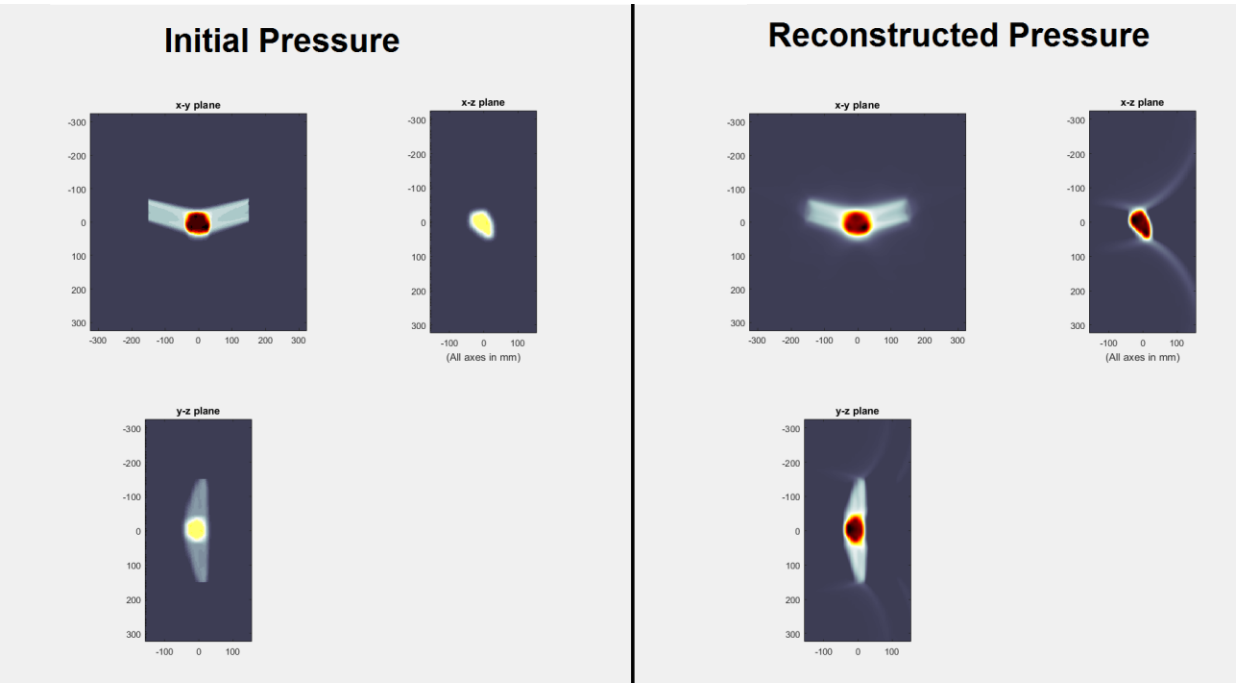

Figure 24: Initial (left) and Reconstructed (right) Pressures for a simulated proton source with θ=1μs in three imaging planes, xy, xz, yz shows the reconstruction of the initial pressure with relatively good fidelity in the range of stress confinement at CT resolutions.

Reconstruction of Relative Dose

The final step in the simulation workflow is the reconstruction of the dose via a time reversal algorithm, which is conveniently built into the k-wave toolbox. This is done through the reconstruction of the initial pressure in the k-wave simulation. After $D_{\theta i}(t)$ is obtained by

convolution of a Gaussian pulse, the sensor positions in the simulation now serve as boundary conditions on which the boundary condition

$$P_i = D_{\theta i}(t)$$

in time can be enforced, where P_i is the pressure at the location of sensor i. The simulation is now run in reverse in time and the pressure is allowed to propagate. After the reverse simulation is run, the final pressure corresponds well to the initial pressure.

One consideration that must be made is the avoidance of the inverse-crime in numerical reconstruction, in order to account for this fact the reverse simulation is performed in a slightly different number of grid points than the forward simulation.[110,111]

Results

Reconstructions were run for a variety of protoacoustic pulse widths, speciically at $\theta = 1\text{ns}, 1\mu s$, $10\mu s, 15\mu s$, and $30\mu s$. An example 3D output (with $\theta = 1\mu s$) is shown in Figure 24. It can be seen that at this pulse width, while there is some distortion and artifacts in the reconstructed initial pressure relative to the trie initial pressur, the pressure can be reconstructed with relatively good fidelity.

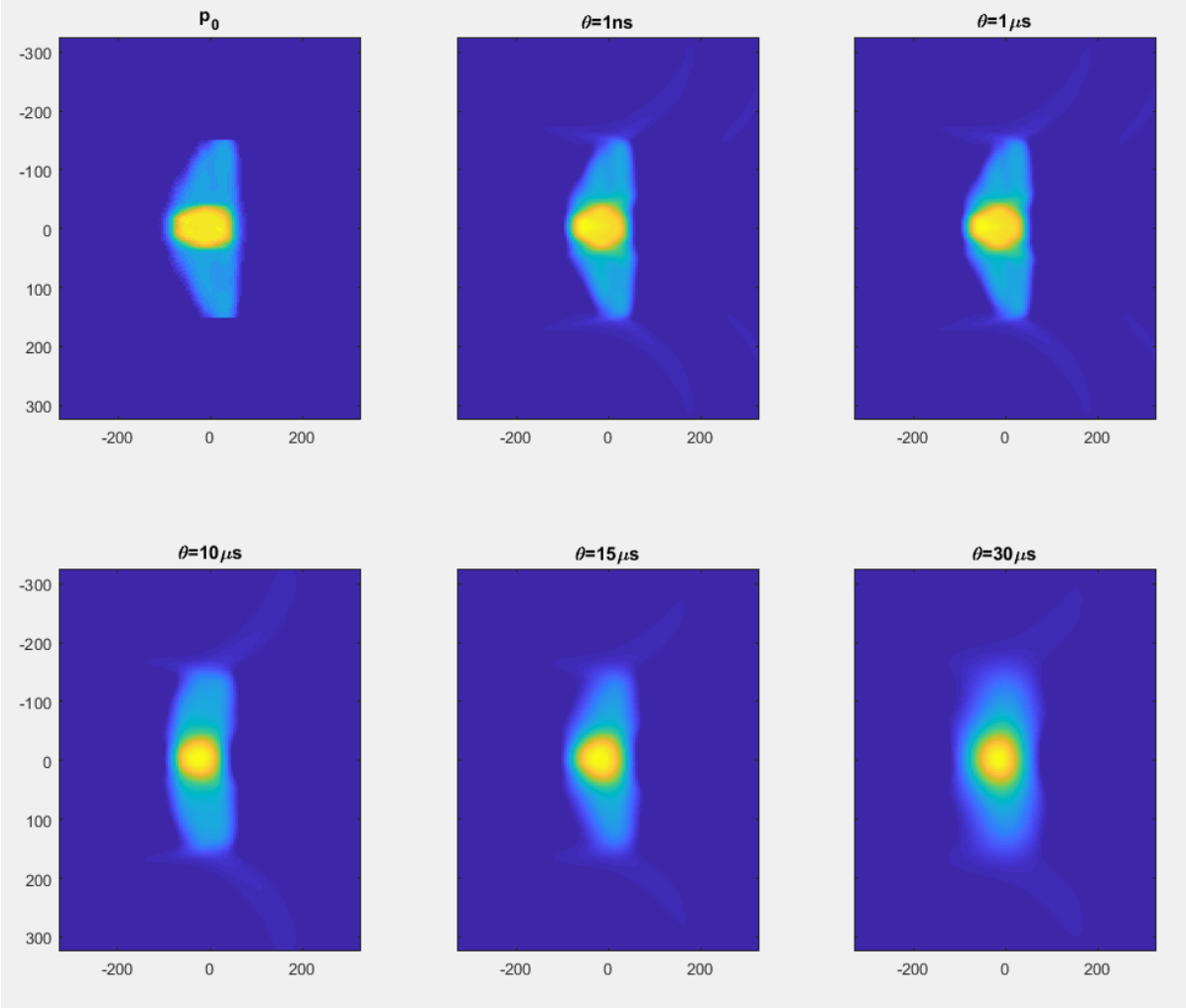

Figure 25: Pulse width dependence on Bragg peak Localization. All axes in mm. Image colormap is normalized for all images. Top left image is the true initial pressure for a delta function excitation, and all other images are reconstructed initial pressures at varying values of θ. Stress confinement occurs at $\theta < 8.66\mu s$

The performance of the reconstruction, as expected, decays with increasing pulse width. The pulse width dependence on the reconstruction is shown in Figure 21. It can be seen that at very low pulse widths ($\theta = 1\text{ns}$), the reconstruction performs best. This is because at pulse widths this low,

$\sum_j D_{\delta i}(j)S(k-j+1) \approx D_{\delta i}(k)$, and the convolution function does not change the characteristics of the signal all that much. This is consistent with what has been reported in literature [34,36,38]. The condition of stress confineement on pulse width is given as

$$\theta < d_c/v_s$$

As per equation 3. Where d_c is the desired resolution. As this simulation operates in a discretized space, the maximum achievable resolution in the simulation is limited by the grid spacing, which matches the dimensions of the planning CT scan (13mm in x and y directions, 25mm in the z direction). This corresponsed to a stress confinement time of 8.66μs in water. Therefore, stress confinement at this length scale is met for all simulations of $\theta < 8.66\mu s$.

The effect of stress confinement can be seen in Figure 25 for all the reconstructions without stress confinement, there is little to no difference seen. This is because all of these conditions are well appoximated as delta pulse excitations at the resolution limits set by the planning CTs. However, once stress confinement starts to be breached at the planning CT resolutions, resolution decay in the Bragg peak reconstruction is visible. These simulations demonstrate a useful guideline in clinical procedure of determining the optimal proton pulse peak for the desired accuracy of Bragg peak localization.

Discussion

The simulation results show that protoacoustic Bragg peak localization is possible in 3D, and therefore that full relative dose reconstruction is possible using protoacoustic Bragg peak range verification.

The simulation workflow demonstrated in this study provides a road-map through which clinicians can assess the feasibility of protoacoustic range verification for a wide variety of proton Bragg peaks. The simulation workflow is versatile with the planning CT used, the pulse width of the generated proton beam, the detector distribution, and the sample size and sound speed. This reconstruction is also robust to heterogeneities in sound speed in the sample, as the time reversed simulation is run with the same grid that ran the forward simulation, therefore if the planning CT can map tissue sound speeds and densities, this is a usable workflow for clinical practice.

There remain, however, important constraints to consider with the model. Firstly, the model's maximum resolution is ultimately limited by the input planning CT, therefore any pulse widths that may conceivably achieve (in practise) better resolutions than the panning CT will only achieve the resolution of the planning CT itself. Secondly, this model does not consider the potential of bandwidth limitations in the ultrasonic detection, however this can be refined in future studies via the application of band-pass filtering to input signals prior to the application of equation 28.

The work presented in this chapter has confirmed via simulations that protoacoustic signals are capable of enabling 3D dose mapping during radiation therapy. However, there remain potential areas of improvement in the models in order to achieve a realistic and clinically deployable simulation workflow for Protoacoustic range verification.

Reconstruction algorithms

One crucial area of improvement over the presented models is the potential for deploying more sophisticated image reconstruction algorithms than conventional time-reversal based reconstruction. While time-reversal is a very versatile algorithm that is robust to changes in transducer geometry and even (when sample acoustic characteristics are well known) attenuation

and sound speed inhomogeneities, the reconstruction time for time reversal is equal to that of the forward simulation. Therefore, the deployment of time reversal algorithms effectively doubles (at least) the time of the simulation as the reverse simulation takes as much time as the forward simulation. Faster reconstruction algorithms that are transducer specific can be of use here, especially in the context of accomplishing real-time imaging as would be necessary protoacoustic and x-ray acoustic monitoring in proton and radiation therapies of cancers.

Another potential area of improvement in reconstruction is the combination of the presented models with reconstruction algorithms that can solve the limited view problem.[141] Deep learning is specially promising in this regard, as there have already been promising studies that have shown that deep learning has great potential to enable to solution of the limited view problem in TA imaging. The deployment of deep learning in order to solve the limited view problem in TAI reconstruction can enable the use of more convenient and realistic array geometries such as linear arrays for imaging 3D volumes while still minimizing loss of information due to limited viewing of the sample.

Parallel processing

The speed of the simulation can be improved upon via the use of parallel processing techniques. Currently our forward and reverse simulations run on a conventional dual core desktop computer, which can limit the time of the simulations to several hours. However, through parallelization of the Fourier transform step used in k-wave's pseudospectral method, the speed of simulations can be drastically improved roughly linearly with the number of cores available.

The speed of these simulations, especially in 3D, remains a major constraint of all models presented in this thesis. While this can be mitigated by the use of the C++ version of k-wave in lieu of running in MATLAB, there remains a fundamental constraint on the current framework caused by the fact that the calculations are not parallelized. K-wave uses a pseudospectral method to solve equation 1, so while the spatial solution is acquired using spectral methods, the temporal solution is acquired using conventional finite element transition between timesteps. This means that the potential for parallelization is limited to only the spatial computations as opposed to temporal computations. Fortunately, the spatial calculations are where most of the computational power is dedicated typically.

Parallelization is only typically required in the context of the computationally heavy 3D simulations deployed, as only these memory heavy simulations typically take long enough times to justify the use of parallel computing. While there is a general parallelized version of the C++ code available on the k-wave website, the optimal parallelization must be performed for the specific machines in which k-wave is running. This can be done through OpenMPI[142] run on a local high-performing computer with multiple cores. A parallelized version of the simulation scripts should enable speed improvements roughly proportional to the number of cores available and could drastically reduce reconstruction time by more than an order of magnitude.

Quantitative Dose mapping

The final area of improvement of the presented models is the development of amplitude quantification within the simulations. The simulations presented in this thesis provide a useful framework through which the resolution and frequency characteristics of TAI can be predicted,

however the reconstructed pressures remain relative values as shown in Chapters 3 and 5. This is because the time reversal algorithm does not appropriately normalize the reconstructed initial pressures since usually there is information loss from the forward simulation due to insufficient coverage of the samples. Therefore, it would be useful towards the estimation of TAI sensitivity if the numerical simulations could also incorporate accurate amplitude estimates for the reconstructions via some correction of the limited view problem not just for resolution but also for quantitative amplitude estimation. However, missing this, the methods used for sensitivity estimation in Chapter 3 suffice and can be deployed for macroscopic contexts in future studies.

The main motivation behind the development of a quantitative Protoacoustic reconstruction is the dose relationship to the initial pressure. As the initial pressure induced by a given dose is known, a quantitatively accurate reconstruction of the initial pressure in protoacoustics would in turn translate to a quantitative dosimetry that could operate in 3D.

Conclusion

In conclusion, simulations have demonstrated here a function workflow for 3D protoacoustic imaging with real clinical treatment planning software input. The simulation workflow is robust to sample geometries and sensor geometries and can serve as a useful tool for investigations of the feasibility of proton therapy on a wide variety of proton machines for which the temporal radiation pulse profile is well known.

Chapter 6: Conclusion

Overview

This thesis has developed a modelling formalism that is usable at multiple scales of thermoacoustic imaging. A comprehensive set of equations was developed modelling the temperature rise and image characteristics of nPAT imaging. During this procedure, a more generalizable numerical modelling simulation workflow was generated with generalizable applications to thermoacoustics across a wide variety of ranges.

Experimental verification of model predictions about signal generation bandwidth for the case of nPAT was confirmed, and it was shown that as the model had predicted nPAT signal generation of GHz signal can be verified experimentally. More importantly, this thesis has presented a generalized simulation framework based on the k-wave toolbox that should be extendable to thermoacoustic investigations at all length scales and time scales up to at least the range of nanoseconds. The models developed when deployed for high-resolution imaging with nPAT predict thermal safety, GHz signal generation, comparable NEN to PAM, and maximum achievable resolutions of ~10nm. The models also confirm the feasibility of high-resolution RBC imaging via the use of nPAT and add further credence to the prospect of doing so in vivo. The numerical models developed for nPAT imaging were found to be generalizable to macroscale phenomena such as protoacoustic range verification. The numerical modelling workflow consists of importing an initial pressure from known sample geometries, using the pseudospectral method

within the k-wave toolbox to model attenuation, propagation, and reconstruction, and comparing the resulting images to the true initial pressure.

The theoretical framework presented here can enable the characterization of additional thermoacoustic imaging modalities such as Electro-Acoustic Tomography[143], ionoacoustic range verification[31,32,138,139], and future iterations of nPAT. The key to the translatability of the models is to ensure that the initial pressure constraints are well matched the excitation source alone, as the acoustic propagation is modelled using fixed equations. So long as the initial pressure in a k-wave simulation matches the induced initial pressure from incident radiation, the imaging should be simulated accurately using k-wave for modelling.

As the main variation between TAI modalities is the excitation source, and k-wave has no intrinsic support for excitation sources, it is double important to ensure the accuracy of the initial pressure, which fundamentally requires a user to understand the excitation source characteristics in great detail. Therefore, while the numerical models presented in this thesis are versatile to TAI at various length and temporal scales, they nevertheless demand that the excitation source characteristics, such as energy deposition and pulse profile, are well understood. In a situation where the excitation source's temporal and spatial energy deposition characteristics are not well understood, the numerical model using the pseudospectral method is not capable of generating an accurate simulation for TAI applications.

Summary

In summary, this thesis has demonstrated modelling of thermoacoustic phenomena at multiple length scales in order to inform experimental realization of TAI at both nano and macroscopic

imaging. Through the work presented here, the thermal safety, bandwidth characteristics, sensitivity, and resolution of nanoscale imaging have been predicted. The bandwidth characteristics have been experimentally verified, and the simulation models used for imaging at nanoscales have been shown to be promising also for the study of macroscopic TAI such as x-ray and proton induced ultrasound imaging.

References

1. Stein, E. W., Maslov, K. I. & Wang, L. V. Noninvasive, in vivo imaging of blood-oxygenation dynamics within the mouse brain using photoacoustic microscopy. *JBO* **14**, 020502 (2009).
2. Nasiriavanaki, M. *et al.* High-resolution photoacoustic tomography of resting-state functional connectivity in the mouse brain. *PNAS* **111**, 21–26 (2014).
3. Hariri, A., Omidi, P., Nasiriavanaki, M., Nasiriavanaki, M. & Nasiriavanaki, M. Resting-State Functional Connectivity Measurement in the Mouse Brain using a Low Cost Photoacoustic Computed Tomography. in JW4A.62 (Optical Society of America, 2016). doi:10.1364/FIO.2016.JW4A.62.
4. Hu, S., Maslov, K. I., Tsytsarev, V. & Wang, L. V. Functional transcranial brain imaging by optical-resolution photoacoustic microscopy. *JBO* **14**, 040503 (2009).
5. Maslov, K., Stoica, G. & Wang, L. V. In vivo dark-field reflection-mode photoacoustic microscopy. *Opt. Lett., OL* **30**, 625–627 (2005).
6. Li, M.-L. *et al.* In-vivo photoacoustic microscopy of nanoshell extravasation from solid tumor vasculature. *JBO* **14**, 010507 (2009).
7. Maslov, K., Zhang, H. F., Hu, S. & Wang, L. V. Optical-resolution photoacoustic microscopy for in vivo imaging of single capillaries. *Opt. Lett., OL* **33**, 929–931 (2008).
8. Zhang, H. F., Maslov, K., Stoica, G. & Wang, L. V. Functional photoacoustic microscopy for high-resolution and noninvasive in vivo imaging. *Nature Biotechnology* **24**, 848–851 (2006).

9. Samant, P., Chen, J. & Xiang, L. Characterization of the temperature rise in a single cell during photoacoustic tomography at the nanoscale. *J. Biomed. Opt* **21**, 075009–075009 (2016).

10. Samant, P., Chen, J. & Xiang, L. Photoacoustic tomography of unlabelled red blood cell at the nanoscale. in vol. 9925 992506-992506–7 (2016).

11. Samant, P. *et al.* GHz Photoacoustic Signal Detection by a Pump-Probe System. *IEEE Photonics Technology Letters* **31**, 825–828 (2019).

12. Conkey, D. B. *et al.* Super-resolution photoacoustic imaging through a scattering wall. *Nature Communications* **6**, 7902 (2015).

13. Danielli, A. *et al.* Label-free photoacoustic nanoscopy. *J. Biomed. Opt* **19**, 086006–086006 (2014).

14. Chaigne, T., Arnal, B., Vilov, S., Bossy, E. & Katz, O. Super-resolution photoacoustic imaging via flow-induced absorption fluctuations. *Optica, OPTICA* **4**, 1397–1404 (2017).

15. Murray, T. W., Haltmeier, M., Berer, T., Leiss-Holzinger, E. & Burgholzer, P. Super-resolution photoacoustic microscopy using blind structured illumination. *Optica, OPTICA* **4**, 17–22 (2017).

16. Yao, D.-K., Maslov, K., Shung, K. K., Zhou, Q. & Wang, L. V. In vivo label-free photoacoustic microscopy of cell nuclei by excitation of DNA and RNA. *Optics Letters* **35**, 4139 (2010).

17. Achwal, C. W., Ganguly, P. & Chandra, H. S. Estimation of the amount of 5-methylcytosine in Drosophila melanogaster DNA by amplified ELISA and photoacoustic spectroscopy. *The EMBO Journal* **3**, 263–266 (1984).

18. Kharine, A. *et al.* Poly(vinyl alcohol) gels for use as tissue phantoms in photoacoustic mammography. *Phys. Med. Biol.* **48**, 357–370 (2003).

19. Kolkman, R. G. M., Hondebrink, E., Steenbergen, W., Leeuwen, T. G. J. M. van & Mul, F. F. M. de. Photoacoustic mammography laboratory prototype: imaging of breast tissue phantoms. *JBO* **9**, 1172–1182 (2004).

20. Kitai, T. *et al.* Photoacoustic mammography: initial clinical results. *Breast Cancer* **21**, 146–153 (2014).

21. van der Burg, S. Imagining the Future of Photoacoustic Mammography. *Sci Eng Ethics* **15**, 97–110 (2009).

22. Kruger, R. A. *et al.* Dedicated 3D photoacoustic breast imaging. *Medical Physics* **40**, 113301 (2013).

23. Kruger, R. A., Lam, R. B., Reinecke, D. R., Rio, S. P. D. & Doyle, R. P. Photoacoustic angiography of the breast. *Medical Physics* **37**, 6096–6100 (2010).

24. Manohar, S. *et al.* Initial results of in vivo non-invasive cancer imaging in the human breast using near-infrared photoacoustics. *Opt. Express, OE* **15**, 12277–12285 (2007).

25. Manohar, S., Kharine, A., Hespen, J. C. G. van, Steenbergen, W. & Leeuwen, T. G. van. The Twente Photoacoustic Mammoscope: system overview and performance. *Phys. Med. Biol.* **50**, 2543–2557 (2005).

26. Heijblom, M. *et al.* Visualizing breast cancer using the Twente photoacoustic mammoscope: What do we learn from twelve new patient measurements? *Optics Express* **20**, 11582 (2012).

27. Pramanik, M., Ku, G., Li, C. & Wang, L. V. Design and evaluation of a novel breast cancer detection system combining both thermoacoustic (TA) and photoacoustic (PA) tomography. *Medical Physics* **35**, 2218–2223 (2008).

28. Hickling, S. Feasibility of x-ray acoustic computed tomography as a relative and in vivo dosimeter in radiotherapy applications. (McGill University, 2015).

29. Tang, S. *et al.* X-ray-induced acoustic computed tomography with an ultrasound transducer ring-array. *Appl. Phys. Lett.* **110**, 103504 (2017).

30. Xiang, L. *et al.* X-ray acoustic computed tomography with pulsed x-ray beam from a medical linear accelerator. *Med Phys* **40**, 010701 (2013).

31. Ahmad, M., Xiang, L., Yousefi, S. & Xing, L. Theoretical detection threshold of the proton-acoustic range verification technique. *Medical Physics* **42**, 5735–5744 (2015).

32. Patch Sarah K., Hoff Daniel E.M., Webb Tyler B., Sobotka Lee G. & Zhao Tianyu. Two-stage ionoacoustic range verification leveraging Monte Carlo and acoustic simulations to stably account for tissue inhomogeneity and accelerator–specific time structure – A simulation study. *Medical Physics* **45**, 783–793 (2018).

33. Wang, L. V. Tutorial on Photoacoustic Microscopy and Computed Tomography. *IEEE Journal of Selected Topics in Quantum Electronics* **14**, 171–179 (2008).

34. Zhou, Y., Yao, J. & Wang, L. V. Tutorial on photoacoustic tomography. *J. Biomed. Opt* **21**, 061007–061007 (2016).

35. Wang, L. V. & Hu, S. Photoacoustic Tomography: In Vivo Imaging from Organelles to Organs. *Science* **335**, 1458–1462 (2012).

36. Yao, J. & Wang, L. V. Sensitivity of photoacoustic microscopy. *Photoacoustics* **2**, 87–101 (2014).

37. Paltauf, G., Nuster, R., Haltmeier, M. & Burgholzer, P. Experimental evaluation of reconstruction algorithms for limited view photoacoustic tomography with line detectors. *Inverse Problems* **23**, S81–S94 (2007).

38. Yao, J. & Wang, L. V. Photoacoustic Microscopy. *Laser Photon Rev* **7**, (2013).

39. Zhang, C., Maslov, K., Yao, J. & Wang, L. V. In vivo photoacoustic microscopy with 7.6-μm axial resolution using a commercial 125-MHz ultrasonic transducer. *J Biomed Opt* **17**, (2012).

40. Calasso, I. G., Craig, W. & Diebold, G. J. Photoacoustic Point Source. *Phys. Rev. Lett.* **86**, 3550–3553 (2001).

41. Wang, X. *et al.* Noninvasive laser-induced photoacoustic tomography for structural and functional *in vivo* imaging of the brain. *Nature Biotechnology* **21**, 803–806 (2003).

42. Bell, K. L., Hajireza, P., Shi, W. & Zemp, R. J. Temporal evolution of low-coherence reflectrometry signals in photoacoustic remote sensing microscopy. *Appl. Opt., AO* **56**, 5172–5181 (2017).

43. Chen, S.-L., Guo, L. J. & Wang, X. All-optical photoacoustic microscopy. *Photoacoustics* **3**, 143–150 (2015).

44. Han, Y., Fu, Q., Hou, Q. & Wu, W. Ultrafast dynamics of MnSi1.7 film studied by pump–probe technique. *Mod. Phys. Lett. B* **30**, 1650282 (2016).

45. Capinski, W. S. *et al.* Thermal-conductivity measurements of GaAs/AlAs superlattices using a picosecond optical pump-and-probe technique. *Phys. Rev. B* **59**, 8105–8113 (1999).

46. Danworaphong, S. *et al.* Three-dimensional imaging of biological cells with picosecond ultrasonics. *Applied Physics Letters* **106**, 163701 (2015).

47. Matsuda, O., Larciprete, M. C., Li Voti, R. & Wright, O. B. Fundamentals of picosecond laser ultrasonics. *Ultrasonics* **56**, 3–20 (2015).

48. Thomsen, C. *et al.* Coherent Phonon Generation and Detection by Picosecond Light Pulses. *Phys. Rev. Lett.* **53**, 989–992 (1984).

49. Hoebe, R. A. *et al.* Controlled light-exposure microscopy reduces photobleaching and phototoxicity in fluorescence live-cell imaging. *Nat Biotech* **25**, 249–253 (2007).

50. Klibanov, A. L. Targeted delivery of gas-filled microspheres, contrast agents for ultrasound imaging. *Advanced Drug Delivery Reviews* **37**, 139–157 (1999).

51. Gould, T. J. *et al.* Nanoscale imaging of molecular positions and anisotropies. *Nat Meth* **5**, 1027–1030 (2008).

52. Johnston, L. J. Nanoscale Imaging of Domains in Supported Lipid Membranes. *Langmuir* **23**, 5886–5895 (2007).

53. Novak, P. *et al.* Nanoscale live-cell imaging using hopping probe ion conductance microscopy. *Nat Meth* **6**, 279–281 (2009).

54. Shroff, H., Galbraith, C. G., Galbraith, J. A. & Betzig, E. Live-cell photoactivated localization microscopy of nanoscale adhesion dynamics. *Nat Meth* **5**, 417–423 (2008).

55. Oladipupo, S. *et al.* VEGF is essential for hypoxia-inducible factor-mediated neovascularization but dispensable for endothelial sprouting. *PNAS* **108**, 13264–13269 (2011).

56. Oladipupo, S. S. *et al.* Conditional HIF-1 induction produces multistage neovascularization with stage-specific sensitivity to VEGFR inhibitors and myeloid cell independence. *Blood* **117**, 4142–4153 (2011).

57. Piao, Z. *et al.* High speed intravascular photoacoustic imaging with fast optical parametric oscillator laser at 1.7 μm. *Applied Physics Letters* **107**, 083701 (2015).

58. Xiang, L. *et al.* Noninvasive real time tomographic imaging of epileptic foci and networks. *NeuroImage* **66**, 240–248 (2013).

59. Hu, S., Yan, P., Maslov, K., Lee, J.-M. & Wang, L. V. Intravital imaging of amyloid plaques in a transgenic mouse model using optical-resolution photoacoustic microscopy. *Optics Letters* **34**, 3899 (2009).

60. Zhang, E. Z. *et al.* Multimodal photoacoustic and optical coherence tomography scanner using an all optical detection scheme for 3D morphological skin imaging. *Biomedical Optics Express* **2**, 2202 (2011).

61. Favazza, C. P., Jassim, O., Cornelius, L. A. & Wang, L. V. In vivo photoacoustic microscopy of human cutaneous microvasculature and a nevus. *J. Biomed. Opt* **16**, 016015-016015–6 (2011).

62. Hu, S., Rao, B., Maslov, K. & Wang, L. V. Label-free photoacoustic ophthalmic angiography. *Optics Letters* **35**, 1 (2010).

63. Jiao, S. *et al.* Photoacoustic ophthalmoscopy for in vivo retinal imaging. *Optics Express* **18**, 3967 (2010).

64. Doukas, A. G., McAuliffe, D. J. & Flotte, T. J. Biological effects of laser-induced shock waves: Structural and functional cell damage in vitro. *Ultrasound in Medicine & Biology* **19**, 137–146 (1993).

65. Huang, X., Jain, P. K., El-Sayed, I. H. & El-Sayed, M. A. Determination of the Minimum Temperature Required for Selective Photothermal Destruction of Cancer Cells with the Use of Immunotargeted Gold Nanoparticles. *Photochemistry and Photobiology* **82**, 412–417 (2006).

66. Tang, S., Chen, J., Samant, P., Kelly, S. & Xiang, L. Transurethral Photoacoustic Endoscopy for Prostate Cancer: A Simulation Study. *IEEE Trans Med Imaging* (2016) doi:10.1109/TMI.2016.2528123.

67. Jaunich, M., Raje, S., Kim, K., Mitra, K. & Guo, Z. Bio-heat transfer analysis during short pulse laser irradiation of tissues. *International Journal of Heat and Mass Transfer* **51**, 5511–5521 (2008).

68. Park, H. *et al.* Characterizations of individual mouse red blood cells parasitized by Babesia microti using 3-D holographic microscopy. *Scientific Reports* **5**, 10827 (2015).

69. Cox, B. T., Arridge, S. R., Köstli, K. P. & Beard, P. C. Two-dimensional quantitative photoacoustic image reconstruction of absorption distributions in scattering media by use of a simple iterative method. *Applied Optics* **45**, 1866 (2006).

70. Evans, E. & Fung, Y.-C. Improved measurements of the erythrocyte geometry. *Microvascular Research* **4**, 335–347 (1972).

71. Dao, M., Lim, C. T. & Suresh, S. Mechanics of the human red blood cell deformed by optical tweezers. *Journal of the Mechanics and Physics of Solids* **51**, 2259–2280 (2003).

72. Mills, J. P., Qie, L., Dao, M., Lim, C. T. & Suresh, S. Nonlinear elastic and viscoelastic deformation of the human red blood cell with optical tweezers. *Mech Chem Biosyst* **1**, 169–180 (2004).

73. Pozrikidis, C. Resting shape and spontaneous membrane curvature of red blood cells. *Math Med Biol* **22**, 34–52 (2005).

74. Fildes, J., Fisher, S., Sheaff, C. M. & Barrett, J. A. Effects of short heat exposure on human red and white blood cells. *J Trauma* **45**, 479–484 (1998).

75. Fanjul-Vélez, F., Ortega-Quijano, N., Solana-Quirós, J. R. & Arce-Diego, J. L. Thermal Damage Analysis in Biological Tissues Under Optical Irradiation: Application to the Skin. *Int J Thermophys* **30**, 1423–1437 (2009).

76. Lapotko, D. O. & Zharov, V. P. Spectral evaluation of laser-induced cell damage with photothermal microscopy. *Lasers Surg. Med.* **36**, 22–30 (2005).

77. Kasper, R. *et al.* Single-Molecule STED Microscopy with Photostable Organic Fluorophores. *Small* **6**, 1379–1384 (2010).

78. Cella Zanacchi, F. *et al.* Live-cell 3D super-resolution imaging in thick biological samples. *Nat Meth* **8**, 1047–1049 (2011).

79. Freudiger, C. W. *et al.* Label-Free Biomedical Imaging with High Sensitivity by Stimulated Raman Scattering Microscopy. *Science* **322**, 1857–1861 (2008).

80. Rust, M. J., Bates, M. & Zhuang, X. Sub-diffraction-limit imaging by stochastic optical reconstruction microscopy (STORM)., Stochastic optical reconstruction microscopy (STORM) provides sub-diffraction-limit image resolution. *Nat Methods* **3, 3**, 793, 793–795 (2006).

81. Huang, B., Wang, W., Bates, M. & Zhuang, X. Three-Dimensional Super-Resolution Imaging by Stochastic Optical Reconstruction Microscopy. *Science* **319**, 810–813 (2008).

82. Hell, S. W. *et al.* The 2015 super-resolution microscopy roadmap. *J. Phys. D: Appl. Phys.* **48**, 443001 (2015).

83. D'Este, E., Kamin, D., Göttfert, F., El-Hady, A. & Hell, S. W. STED Nanoscopy Reveals the Ubiquity of Subcortical Cytoskeleton Periodicity in Living Neurons. *Cell Reports* **10**, 1246–1251 (2015).

84. D'Este, E., Kamin, D., Balzarotti, F. & Hell, S. W. Ultrastructural anatomy of nodes of Ranvier in the peripheral nervous system as revealed by STED microscopy. *PNAS* **114**, E191–E199 (2017).

85. Dudok, B. *et al.* Cell-specific STORM super-resolution imaging reveals nanoscale organization of cannabinoid signaling. *Nat Neurosci* **18**, 75–86 (2015).

86. Huber, O. *et al.* Localization Microscopy (SPDM) Reveals Clustered Formations of P-Glycoprotein in a Human Blood-Brain Barrier Model. *PLOS ONE* **7**, e44776 (2012).

87. Hammond, A. M. & Galizi, R. Gene drives to fight malaria: current state and future directions. *Pathogens and Global Health* **0**, 1–12 (2018).

88. Esposito, A. *et al.* FRET Imaging of Hemoglobin Concentration in Plasmodium falciparum-Infected Red Cells. *PLOS ONE* **3**, e3780 (2008).

89. Fitch, C. D. & Kanjananggulpan, P. The state of ferriprotoporphyrin IX in malaria pigment. *J. Biol. Chem.* **262**, 15552–15555 (1987).

90. Pagola, S., Stephens, P. W., Bohle, D. S., Kosar, A. D. & Madsen, S. K. The structure of malaria pigment β-haematin. *Nature* **404**, 307–310 (2000).

91. Sullivan, D. J., Gluzman, I. Y., Russell, D. G. & Goldberg, D. E. On the molecular mechanism of chloroquine's antimalarial action. *PNAS* **93**, 11865–11870 (1996).

92. Fong, K. Y. & Wright, D. W. Hemozoin and antimalarial drug discovery. *Future Med Chem* **5**, 1437–1450 (2013).

93. Guerrant, R. L., Walker, D. H. & Weller, P. F. *Tropical Infectious Diseases: Principles, Pathogens and Practice E-Book*. (Elsevier Health Sciences, 2011).

94. Papadopoulos, S., Jürgens, K. D. & Gros, G. Protein diffusion in living skeletal muscle fibers: dependence on protein size, fiber type, and contraction. *Biophys J* **79**, 2084–2094 (2000).

95. Strohm, E. M., Moore, M. J. & Kolios, M. C. Single Cell Photoacoustic Microscopy: A Review. *IEEE Journal of Selected Topics in Quantum Electronics* **22**, 137–151 (2016).

96. Strohm, E. M. & Kolios, M. C. Classification of blood cells and tumor cells using label-free ultrasound and photoacoustics. *Cytometry Part A* **87**, 741–749 (2015).

97. Dong, B., Sun, C. & Zhang, H. F. Optical Detection of Ultrasound in Photoacoustic Imaging. *IEEE Trans Biomed Eng* **64**, 4–15 (2017).

98. Samant, P., Hernandez, A., Conklin, S. & Xiang, L. Nanoscale Photoacoustic Tomography (nPAT) for label-free super-resolution 3D imaging of red blood cells. in *Nanoimaging and Nanospectroscopy V* vol. 10350 103500P (International Society for Optics and Photonics, 2017).

99. Pontecorvo, E. *et al.* Visualizing coherent phonon propagation in the 100 GHz range: A broadband picosecond acoustics approach. *Appl. Phys. Lett.* **98**, 011901 (2011).

100. Pezeril, T., Klieber, C., Andrieu, S. & Nelson, K. A. Optical Generation of Gigahertz-Frequency Shear Acoustic Waves in Liquid Glycerol. *Phys. Rev. Lett.* **102**, 107402 (2009).

101. Smith, R. J. *et al.* Parallel detection of low modulation depth signals: application to picosecond ultrasonics. *Meas. Sci. Technol.* **19**, 055301 (2008).

102. Bartels, A. *et al.* Ultrafast time-domain spectroscopy based on high-speed asynchronous optical sampling. *Review of Scientific Instruments* **78**, 035107 (2007).

103. Jack, S. H., Hann, D. B. & Greated, C. A. Influence of the acousto-optic effect on laser Doppler anemometry signals. *Review of Scientific Instruments* **69**, 4074–4081 (1998).

104. Giulietti, A. & Ledingham, K. *Progress in Ultrafast Intense Laser Science*. (Springer Science & Business Media, 2010).

105. Xia, W. *et al.* An optimized ultrasound detector for photoacoustic breast tomography. *Medical Physics* **40**, 032901 (2013).

106. Hale, V. L. *et al.* Parasitophorous vacuole poration precedes its rupture and rapid host erythrocyte cytoskeleton collapse in Plasmodium falciparum egress. *PNAS* **114**, 3439–3444 (2017).

107. Glushakova, S., Mazar, J., Hohmann-Marriott, M. F., Hama, E. & Zimmerberg, J. Irreversible effect of cysteine protease inhibitors on the release of malaria parasites from infected erythrocytes. *Cellular Microbiology* **11**, 95–105 (2009).

108. Chandramohanadas, R. *et al.* Apicomplexan Parasites Co-Opt Host Calpains to Facilitate Their Escape from Infected Cells. *Science* **324**, 794–797 (2009).

109. Samant, P., Burt, T. A., Zhao, Z. J. & Xiang, L. Nanoscale photoacoustic tomography for label-free super-resolution imaging: simulation study. *JBO* **23**, 116501 (2018).

110. Treeby, B. E. & Cox, B. T. k-Wave: MATLAB toolbox for the simulation and reconstruction of photoacoustic wave fields. *J Biomed Opt* **15**, 021314 (2010).

111. Treeby, B. E., Jaros, J., Rohrbach, D. & Cox, B. T. Modelling elastic wave propagation using the k-Wave MATLAB Toolbox. in *2014 IEEE International Ultrasonics Symposium* 146–149 (2014). doi:10.1109/ULTSYM.2014.0037.

112. Pelivanov, I. *et al.* High resolution imaging of impacted CFRP composites with a fiber-optic laser-ultrasound scanner. *Photoacoustics* **4**, 55–64 (2016).

113. Menyaev, Y. A. *et al.* Preclinical photoacoustic models: application for ultrasensitive single cell malaria diagnosis in large vein and artery. *Biomed. Opt. Express, BOE* **7**, 3643–3658 (2016).

114. Burnett, J. L., Carns, J. L. & Richards-Kortum, R. In vivo microscopy of hemozoin: towards a needle free diagnostic for malaria. *Biomed Opt Express* **6**, 3462–3474 (2015).

115. Cai, C. *et al.* In vivo photoacoustic flow cytometry for early malaria diagnosis. *Cytometry* **89**, 531–542 (2016).

116. Kapishnikov, S. *et al.* Oriented nucleation of hemozoin at the digestive vacuole membrane in Plasmodium falciparum. *PNAS* **109**, 11188–11193 (2012).

117. Coronado, L. M., Nadovich, C. T. & Spadafora, C. Malarial Hemozoin: From target to tool. *Biochim Biophys Acta* **1840**, 2032–2041 (2014).

118. Goldberg, D. E., Slater, A. F., Cerami, A. & Henderson, G. B. Hemoglobin degradation in the malaria parasite Plasmodium falciparum: an ordered process in a unique organelle. *Proc Natl Acad Sci U S A* **87**, 2931–2935 (1990).

119. Hajireza, P., Shi, W., Bell, K., Paproski, R. J. & Zemp, R. J. Non-interferometric photoacoustic remote sensing microscopy. *Light: Science & Applications* **6**, e16278 (2017).

120. Bohndiek, S. E. *et al.* Photoacoustic Tomography Detects Early Vessel Regression and Normalization During Ovarian Tumor Response to the Antiangiogenic Therapy Trebananib. *J Nucl Med* **56**, 1942–1947 (2015).

121. Laufer, J. *et al.* In vivo preclinical photoacoustic imaging of tumor vasculature development and therapy. *J. Biomed. Opt* **17**, 0560161–0560168 (2012).

122. Guggenheim, J. A. *et al.* Photoacoustic imaging of human lymph nodes with endogenous lipid and hemoglobin contrast. *J. Biomed. Opt* **20**, 050504–050504 (2015).

123. Oh, J.-T. *et al.* Three-dimensional imaging of skin melanoma in vivo by dual-wavelength photoacoustic microscopy. *J. Biomed. Opt* **11**, 034032-034032–4 (2006).

124. Stoffels, I. *et al.* Metastatic status of sentinel lymph nodes in melanoma determined noninvasively with multispectral optoacoustic imaging. *Science Translational Medicine* **7**, 317ra199-317ra199 (2015).

125. Xu, Z., Zhu, Q. & Wang, L. V. In vivo photoacoustic tomography of mouse cerebral edema induced by cold injury. *J. Biomed. Opt* **16**, 066020-066020–4 (2011).

126. Laufer, J., Zhang, E., Raivich, G. & Beard, P. Three-dimensional noninvasive imaging of the vasculature in the mouse brain using a high resolution photoacoustic scanner. *Applied Optics* **48**, D299 (2009).

127. Dasa, M. K. *et al.* High-pulse energy supercontinuum laser for high-resolution spectroscopic photoacoustic imaging of lipids in the 1650-1850 nm region. *Biomed. Opt. Express, BOE* **9**, 1762–1770 (2018).

128. Sangha, G. S., Phillips, E. H. & Goergen, C. J. In vivo photoacoustic lipid imaging in mice using the second near-infrared window. *Biomed. Opt. Express, BOE* **8**, 736–742 (2017).

129. Zhang, C., Zhang, Y. S., Yao, D.-K., Xia, Y. & Wang, L. V. Label-free photoacoustic microscopy of cytochromes. *J. Biomed. Opt* **18**, 020504–020504 (2013).

130. Langer, G. *et al.* Frequency domain optical resolution photoacoustic and fluorescence microscopy using a modulated laser diode. in *Photons Plus Ultrasound: Imaging and Sensing 2017* vol. 10064 1006426 (International Society for Optics and Photonics, 2017).

131. Shelton, R. L. & Applegate, B. E. Ultrahigh resolution photoacoustic microscopy via transient absorption. *Biomed Opt Express* **1**, 676–686 (2010).

132. Dehoux, T. *et al.* Probing single-cell mechanics with picosecond ultrasonics. *Ultrasonics* **56**, 160–171 (2015).

133. Hao, H.-Y. & Maris, H. J. Study of Phonon Dispersion in Silicon and Germanium at Long Wavelengths Using Picosecond Ultrasonics. *Phys. Rev. Lett.* **84**, 5556–5559 (2000).

134. Werley, C. A., Teo, S. M. & Nelson, K. A. Pulsed laser noise analysis and pump-probe signal detection with a data acquisition card. *Review of Scientific Instruments* **82**, 123108 (2011).

135. Gustafsson, M. G. L. Nonlinear structured-illumination microscopy: Wide-field fluorescence imaging with theoretically unlimited resolution. *Proc Natl Acad Sci U S A* **102**, 13081–13086 (2005).

136. Schermelleh, L. Light-optical section through two mouse cell nuclei in prophase, recorded with 3D Structured Illumination Microscopy. https://commons.wikimedia.org/wiki/File:3D-SIM-3_Prophase_3_color.jpg (2009).

137. Schermelleh, L. *et al.* Subdiffraction Multicolor Imaging of the Nuclear Periphery with 3D Structured Illumination Microscopy. *Science* **320**, 1332–1336 (2008).

138. Knopf, A.-C. & Lomax, A. In vivo proton range verification: a review. *Phys. Med. Biol.* **58**, R131–R160 (2013).

139. Jones, K. C., Witztum, A., Sehgal, C. M. & Avery, S. Proton beam characterization by proton-induced acoustic emission: simulation studies. *Phys. Med. Biol.* **59**, 6549–6563 (2014).

140. Treeby, B. E., Jaros, J., Rendell, A. P. & Cox, B. T. Modeling nonlinear ultrasound propagation in heterogeneous media with power law absorption using a k-space pseudospectral method. *J. Acoust. Soc. Am.* **131**, 4324–4336 (2012).

141. Antholzer, S., Haltmeier, M. & Schwab, J. Deep learning for photoacoustic tomography from sparse data. *Inverse Problems in Science and Engineering* **27**, 987–1005 (2019).

142. Gabriel, E. *et al.* Open MPI: Goals, Concept, and Design of a Next Generation MPI Implementation. in *Recent Advances in Parallel Virtual Machine and Message Passing Interface* (eds. Kranzlmüller, D., Kacsuk, P. & Dongarra, J.) 97–104 (Springer Berlin Heidelberg, 2004).

143. Zarafshani, A. *et al.* Real-time in-situ monitoring of electrotherapy process using electric pulse-induced acoustic tomography (EpAT). in *Medical Imaging 2018: Physics of Medical Imaging* vol. 10573 105732J (International Society for Optics and Photonics, 2018).